

ABSTRACT

LIU, XIANG. Heteroepitaxy and Properties of III-V Materials Grown on Nanoscopically Roughened (001) Si. (Under the direction of David E. Aspnes).

The objectives of this work are (1) to study the growth mechanisms of GaP on Si by organometallic chemical vapor deposition (OMCVD) using trimethylgallium (TMG) and phosphine (PH_3) as precursors, and (2) to improve the GaP growth quality by using nanoscopically roughened Si substrates. We study the growth comparatively on (001) GaAs and thermally generated SiO_2 . Inadvertent indirect but important data are also obtained from the polycrystalline GaP deposited on the Mo susceptor surrounding the 2 in. wafers. We use spectroscopic polarimetry (SP) to follow growth in real time, and then analyze the films with atomic force microscopy (AFM) and spectroscopic ellipsometry (SE).

We investigated the gas-phase kinetics inside our vertical-flow, low-pressure OMCVD reactor chamber by calculating various kinetics parameters and characteristic dimensionless numbers based on simple hard-sphere approximations. The results allow a quantitative understanding of the OMCVD processes and the design of optimized growth conditions.

We found that the thicknesses of the deposited GaP films increases or decreases exponentially toward the edge of the wafers. This dependence is incompatible with the common explanation of gas-phase depletion of the precursors. Starting with the diffusion equation, we derive analytic expressions that describe the thickness variations in terms of the diffusion parameters, and evaluate the diffusion length quantitatively. We show that the cause is due to differences in chemical reactivities of the various surfaces, especially the different catalytic effects that they exert on PH_3 decomposition. The results also show that different parts of the surface, including the susceptor, are in constant contact with each other during growth through gas-phase diffusion, and that deposition occurs via a precursor that involves both Ga and P and is formed by heterogeneous catalysis.

We proposed a model for the growth of GaP based on the formation of this precursor and the effects of substrate. Our model, when used together with the thermodynamics and kinetic theories of nucleation and epitaxy, provides a consistent explanation of the various growth behaviors that we have observed.

Heteroepitaxy and Properties of III-V Materials Grown on
Nanoscopically Roughened (001) Si

by
Xiang Liu

A dissertation submitted to the Graduate Faculty of
North Carolina State University
In partial fulfillment of the
Requirements for the degree of
Doctor of Philosophy

Physics

Raleigh, North Carolina

August, 2008

APPROVED BY:

David E. Aspnes
Committee Chair

John E. Rowe

Jacqueline Krim

Robert M. Kolbas

Dedication

To my family

Biography

Xiang Liu was born on October 15, 1982 in Qianjiang, Hubei, China. He received his Bachelor of Science degree in Physics in June, 2003 from Wuhan University, Wuhan, Hubei, China, and in August of the same year he began his graduate study at the Department of Physics in North Carolina State University, Raleigh, NC, USA. Since May 2004, he has been a Research Assistant at the Real-time Diagnostic and Control Laboratory, working towards his Ph.D. degree under the direction of Prof. David E. Aspnes.

Acknowledgements

First and foremost, I would like to thank my advisor, Dr. Dave Aspnes, for providing guidance and inspirations on my research, and for influencing me on many aspects of life. I will always benefit from the numerous scientific and soft skills that I have learned. It is a pleasure and honor for me to work with such a great scientist and mentor.

I want to thank Dr. Inkyo Kim for collaborating with me on most of the GaP OMCVD growth experiments in this work. I would also like to thank Dr. Eric Adles for bringing his unique passion and expertise to the project of ZnO growth. And thanks to the other current and former members of our group, including Mr. Nick Stoute, Mr. Bill Robinson, Dr. Muharrum Asar, and Dr. Haijiang Peng, for making a great team and turning the office into a fun place to work.

I am indebted to the PhD advisory committee members, Drs. Jack Rowe, Robert Kolbas, and Jacqueline Krim, for giving valuable suggestions and comments on my work. I would like to acknowledge Mr. Dong Wu in the Surface Science Laboratory for providing training and consulting on the AFM experiments. I also thank Mr. Stephane Henrion, Ms. Trinity Biggerstaff, and Dr. Gerd Duscher in the Materials Science Department for helping me make the STEM measurements.

Last but certainly not least, I am so much grateful to Lily Liu and my parents Chunping Xiong and Shengping Liu for their constant love, encouragement and support that have accompanied me through this journey.

Table of Contents

List of Tables.....	vii
List of Figures.....	viii
Chapter 1 Introduction.....	1
1.1 Background and overview.....	1
1.2 Literature review.....	4
1.2.1 Heteroepitaxy of GaP on Si by OMCVD.....	4
1.2.2 Heteroepitaxy of GaP on Si by other techniques.....	11
1.2.3 Growth Chemistry.....	12
1.2.4 Heteroepitaxy on patterned Si.....	16
1.2.5 Lateral thickness variations.....	17
Chapter 2 Theory.....	19
2.1 OMCVD.....	19
2.1.1 Thermodynamics.....	19
2.1.2 Gas phase process.....	21
2.1.2.1 Kinetics theory.....	22
2.1.2.2 Dimensionless numbers.....	24
2.1.2.3 Simple growth analysis using the continuity equation.....	27
2.1.3 Surface processes.....	32
2.1.3.1 Adsorption and surface diffusion.....	32
2.1.3.2 Nucleation and the capillarity theory.....	37
2.1.3.3 Epitaxy.....	44
2.2 Polarimetry.....	48
2.2.1 The polarimeter.....	48
2.2.2 Two, three and four phase models.....	50
2.2.3 Dielectric function and the Bruggeman effective medium approximation.....	53
2.2.4 Spectral analysis near critical points.....	55
Chapter 3 Experiment.....	58
3.1 Instrument Overview.....	58
3.2 Materials.....	61
3.3 Polarimeter Calibration.....	63
3.4 Temperature Calibration.....	64
3.5 Thickness-profile measurements.....	68
3.6 Formation of nrSi.....	69
3.6.1 Si reaction with H ₂	69
3.6.2 Si reaction with O ₂	70

3.6.3 Isotropic etching of Si by HF + HNO ₃ + H ₂ O	72
3.6.4 Anisotropic etching of Si by NH ₄ F and NH ₄ OH	78
Chapter 4 Results and Discussion.....	81
4.1 GaP Heteroepitaxy on (001) GaAs	81
4.1.1 Growth and characterization	81
4.1.2 Lateral thickness profile of GaP / (001) GaAs.....	93
4.2 GaP heteroepitaxy on (001) Si.....	96
4.2.1 Growth and characterization of GaP on non roughened Si substrates	96
4.2.2 Analysis of earlier data of GaP / Si	100
4.3 GaP heteroepitaxy on nanoscopically roughened (001) Si	109
4.3.1 Growth and characterization of GaP / nrSi (1:1:1) and (1:3:5).....	109
4.3.2 Lateral thickness variation of GaP / nrSi (1:1:1)	115
4.3.3 Growth and characterization of GaP / nrSi (1% NH ₄ F).....	116
4.4 GaP heteroepitaxy on thermally oxidized Si.....	120
4.4.1 Growth and characterization of GaP / SiO ₂	120
4.4.2 Lateral thickness profile of GaP / SiO ₂	129
4.5 Discussion	132
4.5.1 Arrival-rate calculations: analysis of growth kinetics.....	132
4.5.2 Lateral thickness variations: implications for growth chemistry	138
4.5.3 Growth mechanisms.....	146
Chapter 5 Summary and Conclusions.....	156
References.....	165

List of Tables

Table 1.1 Prior work concerning growth of GaP on Si by OMCVD	9
Table 2.1 Typical flow characteristics with different Reynolds numbers [73].	25
Table 2.2 Number of saturated and unsaturated bonds for atoms in Fig 2.1.9, after Refs. [78, 80].	46
Table 2.3 Information content in the harmonic of a rotating-compensator polarimeter	50
Table 3.1 Various 2” epi-ready wafers.....	62
Table 4.1.1 Growth conditions for representative GaP/GaAs depositions.	83
Table 4.1.2 Characterization parameters for the GaP/GaAs depositions in Table 4.1.1.	84
Table 4.1.3 Initial stage growth parameters for several GaP/GaAs depositions in Table 4.1.1.	84
Table 4.2.1 Growth conditions for representative GaP / Si runs on as-polished wafers.	97
Table 4.2.2 Initial stage growth parameters for GaP / Si run # 10 (1 step = 1.65 s).	109
Table 4.3.1 Growth conditions for representative GaP / nrSi (1:1:1) and (1:3:5) runs.	110
Table 4.3.2 Growth conditions for representative GaP / nrSi (1% NH ₄ F) runs.	117
Table 4.4.1 Growth conditions for representative GaP/SiO ₂ depositions.	124
Table 4.4.2 Characterization parameters for the final films and the initial stages determined by least-squares fitting for representative GaP/GaAs depositions.....	124
Table 4.5.1 Calculated gas-phase kinetic properties using N ₂ as the carrier gas. The left 3 columns in the lower half assume that diffusion is not a factor and that growth is kinetically limited.	134
Table 4.5.2 As Table 4.5.1 but with H ₂ as the carrier gas	135
Table 4.5.3 Dimensionless numbers of our OMCVD system under N ₂ and H ₂ flows.....	135
Table 4.5.4 Growth rate of various Ga species calculated from surface reaction rates.	136
Table 4.5.5 Summary of the effective lateral thickness profiles for representative runs.	139
Table 4.5.6 The effect of different substrates and growth condition on GaP heteroepitaxy.	146

List of Figures

Fig 1.1 GaP island density on (001) Si as a function of (a) V/III ratio (after Ref. [15]), (b) growth rate and (c) misorientation angle from (001) to [110] (after Ref. [16]).....	8
Fig 1.2 Growth mode for the initial stage of GaP on Si under different V/III ratios and pressures, after Ref. [19].....	8
Fig 1.3 PH ₃ decomposition catalyzed by (a) 60 cm ² SiO ₂ , (b) 300 cm ² SiO ₂ , and (c) 60 cm ² InP, after Ref. [35].....	13
Fig 1.4 PH ₃ decomposition (a) without TMI and with (b) PH ₃ /TMI = 4.2, (c) PH ₃ /TMI = 4.2 with InP surface area of 1200 cm ² , and (d) with PH ₃ /TMI = 2.1, after Ref. [37].....	14
Fig 1.5 TMG decomposition with (a) N ₂ [41], and AsH ₃ /TMG/D ₂ = (b) 0/0.6/99.4, (c) 0.3/0.3/99.3, and (d) 3.3/0.3/96.3, after Ref. [38].....	15
Fig 2.1.1 Schematic view of diffusion and mass transfer currents, after Ref. [71].	27
Fig 2.1.2 Precursor adsorption model, after Ref. [69].	33
Fig 2.1.3 Dependence of the adatom diffusion length under typical growth conditions at 600°C on (a) the difference between the desorption energy E _d and the activation energy E _s for surface diffusion, and (b) E _s only.....	36
Fig 2.1.4 2D heterogeneous nucleation process, after Ref. [69].....	38
Fig 2.1.5 3D heterogeneous nucleation process, after Ref. [68].....	39
Fig 2.1.6 Monte Carlo simulation of surface morphology at 20% surface coverage under different supersaturations, after Ref. [77].....	42
Fig 2.1.7 Effect of surfactants on the critical nucleus size and nucleation barrier energy, after Ref. [81].	43
Fig 2.1.8 Schematic representation of flat (F), stepped (S), and kinked (K) surfaces of a simple cubic lattice, after Refs. [78, 80].	45
Fig 2.1.9 Different positions that an atom can occupy, after Refs. [78, 80].	45
Fig 2.2.1 (a) Two phase model, (b) Three phase model, and (c) Four phase model.....	53
Fig 2.2.2 Electronic band structure of Si, after Ref. [83].....	56
Fig 2.2.3 (a) Imaginary part of the dielectric function $\langle \epsilon_i \rangle$ of the room temperature Si; (b) Second energy derivative of $\langle \epsilon_i \rangle$ along with the least-squares fit of Eq. (2.2.2.2).	56
Fig 3.1.1 Integrated OMCVD/polarimeter system.	60
Fig 3.1.2 Spindle assembly with real-time wobble adjustment [85].....	60
Fig 3.2.1 Schematic drawing of an organometallic bubbler [86].....	62
Fig 3.3.1 Relative intensity spectrum of a Hg/Ar lamp [89].	64
Fig 3.4.1 Thermocouple readings vs. measured Si E ₁ transition energies for the original susceptor (red), along with the T dependence of the Si E ₁ transition energy from Ref.	

[83].	66
Fig 3.4.2 Temperature calibration curve for the original susceptor.	66
Fig 3.4.3 As Fig 3.4.1, but with the new susceptor.	67
Fig 3.4.4 As Fig 3.4.2, but for the new susceptor.	67
Fig 3.5.1 (a) Ellipsometer beam measurement positions across an arbitrary 1" wafer radius; (b) Ellipsometer beam path in the entrance arm. The scale is for illustration purpose only.	68
Fig 3.6.1 Critical concentration of O ₂ for the transition between active and passive oxidation, after Ref. [95].	71
Fig 3.6.2 Variation of $\langle\epsilon_i\rangle$ at 3.15 and 4.06 eV observed during thermal oxidation of (001) Si at 800 °C.	71
Fig 3.6.3 Si etching rates in mils/min for different solution compositions at 25 °C, after Ref. [98].	73
Fig 3.6.4 AFM micrographs of (001) Si etched in HF:HNO ₃ :H ₂ O = 1:1:1 solutions for (a) 10 s and (b) 30 s.	75
Fig 3.6.5 SE spectra for the samples of Fig. 3.6.4.	75
Fig 3.6.6 AFM micrographs of (001) Si etched in HF:HNO ₃ :H ₂ O = 1:3:5 solutions for (a) 1 min, (b) 3 min, (c) 4 min, (d) 5 min, (e) 6 min and (f) 7 min.	76
Fig 3.6.7 SE spectra for the samples in Fig 3.6.6, with (a) $\langle\epsilon_r\rangle$ and (b) $\langle\epsilon_i\rangle$ for (001) Si etched for 1 – 4 min, and (c) $\langle\epsilon_r\rangle$ and (d) $\langle\epsilon_i\rangle$ for (001) Si etched for 5 – 7 min.	77
Fig 3.6.8 Evolution of pSi spectra at 600°C under 4 Torr (a) H ₂ for 250s, and (b) N ₂ for 430 s.	77
Fig 3.6.9 Systematic representation of various surface features on a vicinal (111) Si surface, after Ref. [102].	78
Fig 3.6.10 AFM micrographs of (001) Si etched at 80°C in (a) 1% NH ₄ F for 7 min, and (b) 1% NH ₄ OH for 5 min.	79
Fig 3.6.11 SE spectra for the samples in Figure 3.6.10.	80
Fig 4.1.1 $\langle\epsilon\rangle$ from 1.5 to 6 eV for GaP/GaAs depositions A - F measured with the bench SE, together with least-squares fitting with the four-phase model.	85
Fig 4.1.2 AFM micrographs for GaP/GaAs depositions A - F.	86
Fig 4.1.3 (a) RI and (b) $\langle\epsilon\rangle$ data at 2.64 eV for the initial stage of GaP/GaAs run A.	89
Fig 4.1.4 As Fig 4.1.3, but for run B.	89
Fig 4.1.5 Complete (a) RI and (b) $\langle\epsilon\rangle$ data at 2.64 eV for GaP/GaAs growth run E.	90
Fig 4.1.6 (a) RI and (b) $\langle\epsilon\rangle$ data at 2.64 eV for the initial stage of GaP/GaAs run E.	90
Fig 4.1.7 As Fig 4.1.5, but for run F.	91
Fig 4.1.8 As Fig 4.1.6, but for run F.	91
Fig 4.1.9 $\langle\epsilon\rangle$ during the initial phase of run C under PH ₃ only, illustrating P - As exchange.	92
Fig 4.1.10 Lateral thickness profile of GaP / GaAs run A. Thicknesses are in nm, and	

dimensions in the exponent are mm.....	94
Fig 4.1.11 (a) Calculated concentration dependence of the gas-phase reactants along a radius for GaP / GaAs run A, assuming that the thickness is proportional to concentration. The curve is normalized to the concentration at the center. (b) Calculated diffusion current resulting from (a) normalized to the flow at the edge.....	94
Fig 4.1.12 As Fig 4.1.10, but for run C.....	95
Fig 4.1.13 As Fig 4.1.11, but for run C.....	95
Fig 4.1.14 Photograph of a portion of GaP / GaAs run E.....	96
Fig 4.2.1 AFM micrographs of GaP / Si run (a) A and (b) B.....	98
Fig 4.2.2 RI at 2.64 eV for GaP / Si run A.....	98
Fig 4.2.3 AFM micrographs for (a) center and (b) edge of GaP / Si run C.	99
Fig 4.2.4 A piece from GaP / Si run C.	99
Fig 4.2.5 $\langle \epsilon \rangle$ from 1.5 to 6 eV for GaP / Si run # 10.	103
Fig 4.2.6 AFM micrographs at (a) 8 μm and (b) 2 μm for GaP / Si run # 10.	104
Fig 4.2.7 STEM micrographs for GaP / Si run # 10 in the Z-contrast mode. The magnifications are $\times 120\text{K}$ for (a) and (b), $\times 5\text{M}$ for (c), and $\times 8\text{M}$ for (d).	105
Fig 4.2.8 Variation of the E_1 (3.14 eV) and E_2 (4.03 eV) peaks of $\langle \epsilon_i \rangle$ for Si during the PH_3 pretreatment and growth of GaP in run # 10. Here (a) shows the data for steps 900 to 2000, and (b) and (c) enlarged views for 900 to 1130 and 1250 to 1480, respectively.	106
Fig 4.2.9 (a) $\langle \epsilon_r \rangle$ and (b) $\langle \epsilon_i \rangle$ from 1.7 to 5.2 eV during the growth steps 1481 to 1661 for GaP / Si run # 10. The spectra are shown for 20-step intervals (33 s) and are shifted by $5n$ ($n = 0, 1 \dots 9$).....	107
Fig 4.2.10 (a) RI and (b) $\langle \epsilon \rangle$ data at 2.91 eV during growth of GaP / Si run # 10.	108
Fig 4.2.11 (a) RI and (b) $\langle \epsilon \rangle$ data at 2.91 eV along with model fittings for the initial stage of GaP / Si run # 10.....	109
Fig 4.3.1 $\langle \epsilon \rangle$ spectrum from 1.5 to 6 eV for (a) center and (b) edge of GaP/nrSi measured after deposition.....	112
Fig 4.3.2 AFM micrographs of (a) center and (b) edge of GaP/nrSi (1:1:1) run A.	113
Fig 4.3.3 AFM micrographs of GaP / nrSi (1:3:5) run (a) B and (b) C.	113
Fig 4.3.4 (a) $\langle \epsilon_r \rangle$ and (b) $\langle \epsilon_i \rangle$ from 1.7 to 5.2 eV during growth of GaP/nrSi (1:1:1) run A. The spectra are shown for 30 s intervals and for clarity are shifted by $3n$ ($n = 0, 1 \dots 9$).	114
Fig 4.3.5 The change of the GaP E_2 peak of $\langle \epsilon_i \rangle$ at 4.84 eV during growth of GaP/nrSi (1:1:1) run A.....	114
Fig 4.3.6 Thickness profile of GaP / nrSi (1:1:1) run A.....	115
Fig 4.3.7 (a) Calculated concentration change of gas phase reactants along a radius for GaP / nrSi (1:1:1) run A that is required to obtain the observed thickness change, assuming a constant stagnant layer thickness. The scale is normalized to the center concentration. (b) Calculated diffusion current resulted from (a), normalized to the edge flow.....	116

Fig 4.3.8 $\langle \epsilon \rangle$ spectrum from 1.5 to 6 eV for the (a) center and (b) edge regions of GaP / nrSi (1% NH ₄ F) run D, measured after deposition.....	117
Fig 4.3.9 AFM micrographs of the (a) center and (b) edge regions of GaP / nrSi (1% NH ₄ F) run D.	118
Fig 4.3.10 $\langle \epsilon \rangle$ spectrum from 1.5 to 6 eV for the (a) center and (b) edge regions of GaP / nrSi (1% NH ₄ F) run E, measured after deposition.	118
Fig 4.3.11 AFM micrographs of the (a) center, (b) edge, and (c) center between-islands regions of GaP/nrSi (1% NH ₄ F) run E.....	119
Fig 4.3.12 Photograph of a portion of GaP / nrSi (1% NH ₄ F) run D.	119
Fig 4.4.1 $\langle \epsilon \rangle$ spectra from 1.5 to 6 eV for GaP/SiO ₂ runs A - F.	125
Fig 4.4.2 AFM micrographs of GaP/SiO ₂ runs A - F.	126
Fig 4.4.3 (a) RI and (b) $\langle \epsilon \rangle$ data at 2.64 eV for the initial stage of GaP/SiO ₂ run A.	127
Fig 4.4.4 (a) RI and (b) $\langle \epsilon \rangle$ data at 2.64 eV for the initial stage of GaP/SiO ₂ run B.	127
Fig 4.4.5 (a) RI and (b) $\langle \epsilon \rangle$ data at 2.64 eV for the initial stage of GaP/SiO ₂ run C.	128
Fig 4.4.6 (a) RI and (b) $\langle \epsilon \rangle$ data at 2.64 eV for the initial stage of GaP/SiO ₂ run E.	128
Fig 4.4.7 Thickness profile of GaP / SiO ₂ run C.....	129
Fig 4.4.8 (a) Calculated concentration change of gas phase reactants along a radius for GaP / SiO ₂ run C normalized to the center concentration. (b) Diffusion current resulting from (a) normalized to the edge flow.....	130
Fig 4.4.9 A segment of sample of GaP / SiO ₂ run C.	130
Fig 4.4.10 Thickness profile of GaP / SiO ₂ run F.	131
Fig 4.4.11 A piece from the sample of GaP / SiO ₂ run F.....	131
Fig 4.4.12 AFM micrograph for the (a) center and (b) edge of GaP / SiO ₂ run F.....	131
Fig 4.5.1 Plots of Eqs. (4.5.11) and (4.5.12) for $a = 0$ and $L = 5$	142

Chapter 1 Introduction

1.1 Background and overview

Polar-on-nonpolar heteroepitaxy, mainly III-V materials on Si, has been studied extensively since the 1980s due to the potential technological importance of merging optoelectronic and Si technologies [1-66]. However, the associated chemical and structural incompatibilities cause formidable difficulties, especially charge discontinuity at the heteroepitaxial interface, low densities of nucleation sites, and three-dimensional (3D) growth, to mention several. Many attempts have been made to overcome these problems. Some examples include: (1) use of unconventional orientations to realize interface charge neutrality [25, 26]; (2) use of buffer layers to form a structural and chemical transition between substrate and epilayer [33, 50]; (3) two-step processes where growth is started at a lower temperature to increase the critical nucleation density during the initial stage [6, 7]; (4) preflow by more reactive species to reduce the interfacial energy, thus increasing nucleation and promoting 2D growth [10]; and (5) ion-assisted deposition by suppressing 3D nucleation through ion-induced removal of atoms [51].

In addition to the chemical- and structural-mismatch factors mentioned above, investigation of heteroepitaxy is complicated further by a third reason: up to now essentially all investigators have been taking an indirect approach toward solving the problem rather than the direct approach of examining surface properties in real time, especially during the critical first stages of heteroepitaxy. Because diagnostic equipment that can provide chemical and structural information about surfaces during growth is not generally available, heteroepitaxy is typically studied by post-deposition analysis of deposited material through

micrographs obtained with transmission electron microscopy (TEM), determinations of surface topography by atomic force microscopy (AFM), electrical measurements, etc. While reflection high-energy electron diffraction (RHEED) is a standard surface-analysis tool in molecular beam epitaxy (MBE), RHEED is a structural probe that cannot access surface chemistry, and is not applicable under the relatively high pressure environment of organometallic chemical vapor deposition (OMCVD). Detailed information about the growth process as it is occurring is needed, in addition to post-deposition characterization.

OMCVD is a powerful technique that is used to grow many device-quality compound semiconductors. Its advantages include the additional flexibility provided by chemistry, and the possibility of scale-up to industrial levels of production. However, the OMCVD is a complex combination of thermodynamics, mass transport, homogeneous gas phase kinetics, and heterogeneous surface kinetics. As it also involves various precursor species, possible differences in reactivity between initial and subsequent homoepitaxial growth surfaces may present further challenges.

The objective of this work is to study OMCVD growth mechanisms, and to explore the possibility of improving film quality in the chemically mismatched but nearly lattice-matched combination of GaP on Si. We work within contemporary OMCVD technology, and examine particularly the possibility of improving the quality of the deposited material by using Si substrates that are deliberately roughened on the scale of nm prior to growth. We use Spectroscopic Polarimetry (SP) to follow growth chemistry in real time, and then analyze the deposited material with various techniques including atomic force microscopy (AFM), and spectroscopic ellipsometry (SE).

From a thermodynamic point of view, substrates that are rough on a nm scale have larger surface areas and higher densities of irregularly oriented dangling bonds with respect to conventional singular or vicinal substrates. Thus the surface energies are larger and the nucleation energy barriers are smaller. From a kinetics point of view, such nanoscopically

roughened (nr) substrates contain a high density of kink sites, which can also facilitate nucleation. Thus these substrates are expected to improve film continuity. They can also be expected to reduce lattice strain and charge-discontinuity effects at the heteroepitaxial interface, while preserving the integrity of the underlying lattice. The latter is particularly important for heteroepitaxy.

Since both chemical and structural incompatibilities exist during the initial stage of polar-on-nonpolar heteroepitaxy, it is desirable to study the two effects separately by performing parallel experiments on material combinations where one is more important than the other. As a result we also investigate GaP on GaAs and GaP on SiO₂. GaP on Si exhibits the complications of chemical mismatch, but the lattice mismatch of only 0.37% minimizes those from strain. GaP on GaAs is a chemically compatible system since both materials have the same polar nature, so the 3.6% lattice mismatch at room temperature becomes the dominant factor affecting growth. GaP on thermally grown SiO₂ on Si is an interesting case of a polar-on-polar system, but the amorphous nature of the substrate does not provide a template for epitaxial growth. Studying these systems comparatively helps identifying the origins of the different growth behaviors. Also, information gained about chemical driving forces and precursor reactivities on different substrates is useful in understanding the general process of OMCVD as well.

Our study of heteroepitaxy is greatly facilitated by real-time SP. Our OMCVD system features an integrated spectroscopic polarimeter that covers a spectral range of 230 to 840 nm and acquires both relative-intensity (RI) and pseudodielectric function $\langle \epsilon \rangle$ data at a 4 Hz rate. Hence it can follow surface chemistry in the sub-nm range on time scales well under 1 s. As described in Ch. 2, RI and $\langle \epsilon \rangle$ data are analyzed using least-squares programs with the three-phase model and reference spectra at specific temperatures, and parameters such as film composition and growth rate can be readily extracted.

We also find that the lateral thickness variation of the deposited film near the edge of the

substrate provides very useful information. Since the physical process of epitaxial growth can be viewed as the accumulation of various atoms, the thickness profile is a direct measure of the local gas-phase distribution of the species that determines the growth rate. In principle, this can be Ga, P, or a compound containing both. By comparing lateral thickness variations that occur for different substrates, we perform an analysis of their chemistries relative to that of a fifth substrate, the polycrystalline GaP material deposited on the molybdenum susceptor that surrounds the actual substrate. This initially unplanned experiment actually provides a wealth of information not only about diffusion lengths in the gas phase but also about the growth process itself. As discussed more completely in Ch. 4, these data provide unambiguous evidence that deposition occurs via a precursor that involves both Ga and P species, is formed by heterogeneous catalysis and largely desorbed.

1.2 Literature review

1.2.1 Heteroepitaxy of GaP on Si by OMCVD

Although the growth of GaP on Si by OMCVD is very challenging, a number of groups have reported varying degrees of success. A selection of relevant results is given in Table 1.1. The substrates are mainly (001) Si with various degrees of miscut. The precursors are mainly trimethylgallium (TMG) and phosphine (PH₃). Other orientations and precursors such as triethylgallium (TEG) have been used, as listed in the last column of Table 1.1.

A universal pretreatment procedure appears to be the following. The Si substrates are heated to 850 to 1180 °C under H₂ for intervals of the order of minutes, with the objective of removing residual oxides. However, this pretreatment is also known to roughen Si. This inadvertent nanoroughening step appears to be a requirement for the production of continuous films, further justifying a systematic investigation.

Andre et al. [1] found that (001) Si substrates with a 3° or 4° miscut towards [110] and annealed in a PH₃ preflow reduced the film cracking density and promoted the growth of single crystals. They studied GaP nucleation during the initial 15 s by scanning electron microscopy (SEM). The nuclei are seen to be elongated along <110> directions and are randomly distributed.

Beneking et al. [3] found that enhancing PH₃ decomposition before growth by passing it through a hot zone reduced the V/III ratio needed by 2 orders of magnitude relative to normal growth conditions.

Olson et al. [6] found that with their approach GaP heteroepitaxy on Si follows a 3D growth mode. The misoriented nuclei coalesce to give a smooth polycrystalline film at 500°C and a rougher film at 600°C. However, they do not coalesce at 800°C. Thus Olson et al. recommended a 2-step growth method, where a lower temperature of 500°C is used to nucleate the initial 30 – 50 nm polycrystalline layer, and a higher temperature of 750°C to grow the bulk single-crystal layer. They also found that the initial nuclei have a high density of defects, and that a ~ 2.5 nm SiO₂ layer may exist between the nuclei and the Si substrate. The defect density was 10¹¹ cm⁻² at the heterointerface and 10⁸ cm⁻² on the surface of a 2 μm thick film.

Sugo et al. [7] also used the same 2-step growth method, with temperatures of 450°C and 730°C for the growth of a < 20 nm initial layer and the bulk layer respectively. They also found that GaP grows as randomly spaced 3D islands of about 5 μm in size at 700°C with a small TEG flow. However, increasing the TEG flow promoted the formation of a continuous film.

A group of researchers at the Nagoya Inst. of Tech. in Japan and their coworkers performed extensive investigations on this topic [10-19]. Many mechanisms have been proposed to explain their results, which are mainly based on surface-diffusion considerations. A brief summary of their results is given below.

Kohama et al. [10, 11] used an AsH₃ preflow at 900 to 1100 °C before growth, finding that this promoted the growth of continuous GaP epilayers in the early stages. In addition, crystal quality was improved and defect density reduced. Also, the heterointerface was sharper and Si outdiffusion was suppressed. They explained this through the formation of an As-stabilized surface because AsH₃ adsorbs more readily than PH₃. This reduces the interfacial energy, so the wetting angle of a nucleus becomes smaller. In a following paper, Soga et al. [12] found that preheating the Si substrate to 900 °C under PH₃ and H₂ was a key to obtaining smooth GaP epilayers. In their model preheating the Si substrate in PH₃ covers the Si substrate with a layer of P atoms, which enhances the wetting of GaP by effectively reducing the surface migration of the reactive Ga species once growth starts. This technique has also been used by Su [4].

These authors also studied the effect of the V/III ratio on the heteroepitaxy of GaP on Si [13-19]. They found that growth under large V/III ratios yielded smoother morphologies and better crystal quality with fewer defects. Imaizumi et al. [13] concluded that high V/III ratios suppress the surface migration of the adsorbed reactive species, which they assumed to be GaP dimers. Soga et al. [14] proposed that high V/III ratios enhance the adsorption of P species, so the observed shorter surface-diffusion lengths of the mobile species are due to the increased probability of being captured by adsorbed P species. They also suggested that many of the mobile species under high V/III ratios may exhibit larger molecular masses than those under low V/III ratios, which would also reduce surface mobility. They concluded in a following paper that the mobile species are clusters having the form of Ga_xP_y [15].

Soga et al. plotted GaP island density on (001) Si as a function of V/III ratio, growth rate, and misorientation angle respectively, as shown in Figure 1.1 (a), (b) and (c) after Ref. [15, 16]. They also include a GaAs case for comparison. They explained the results as follows [16]. The density of GaP islands increases exponentially with V/III ratio due to the increased reaction probability of generating Ga_xP_y clusters, since more reactive P species are

available at higher V/III ratios. Also, since the decomposition rate of AsH_3 is high, nucleation reactions are already easy, so the GaAs island density is already large and does not increase with V/III ratio. GaP island density increases linearly with growth rate due to the reduced time for reaching critical nucleus size, which in turn reduces the diffusion length. However this explanation cannot explain why the nucleation density increases. The more important reason, as we will present later, is that the increased TMG supersaturation that is responsible for the larger growth rates also reduces the nucleation barrier energy. Soga et al. [16] also found that the GaP island density is not affected by misorientation angle, so increasing the step density and thus atomic height roughness does not promote nucleation. This is also consistent with our observations.

Suzuki et al. [17] proposed that the reactants can be divided into two categories, one of which results in direct quasi-2D growth (species A) and the other that does not (species B). At low V/III ratios species A is not stable and its density is small, so nucleation is discrete and the nuclei grow through the adsorption, migration, and incorporation of species B. At higher V/III ratios the density of species A is sufficiently large to promote high nucleation densities, and a continuous GaP film can be formed at an early stage through the coalescence of the nuclei. This is again consistent with our data and our proposed model for the GaP growth mechanism, as we will present later.

These authors observed that the GaP growth mode can be different on different regions of the Si wafer along the flow path of their horizontal reactor, being 3D upstream and 2D downstream [12, 17]. They explained that it is due to the increased downstream availability of P, and thus a higher P/Ga ratio. This is consistent with the fact that PH_3 is difficult to decompose, and that it probably happens mainly above the substrate.

Finally, these authors found that the critical V/III ratio for quasi-2D growth is larger at lower chamber pressures [17-19], as seen in Fig. 1.2 [19]. They argued that the resident time of PH_3 in the hot zone is reduced at low pressures due to the increased gas flow rate, so

decomposition is less efficient. However, as we will see from our data analysis, this explanation is not accurate.

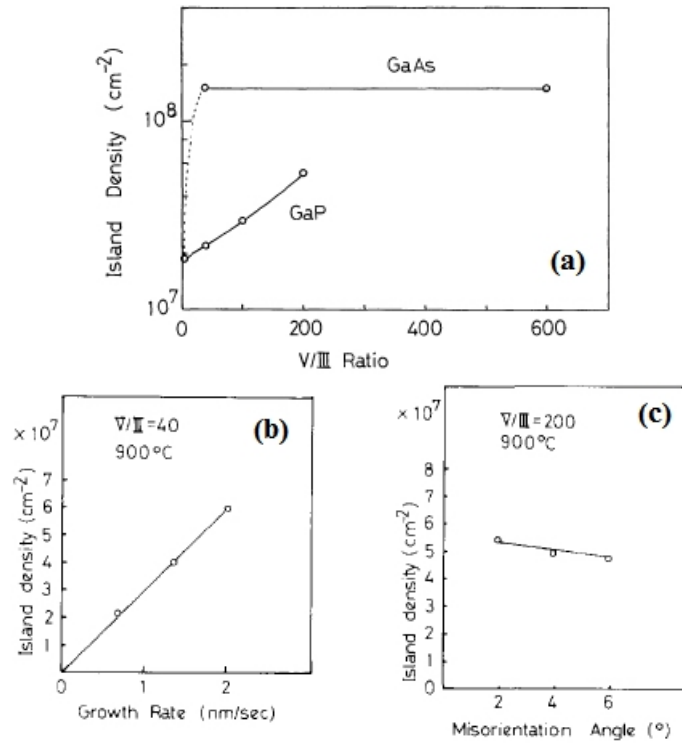


Fig 1.1 GaP island density on (001) Si as a function of (a) V/III ratio (after Ref. [15]), (b) growth rate and (c) misorientation angle from (001) to [110] (after Ref. [16]).

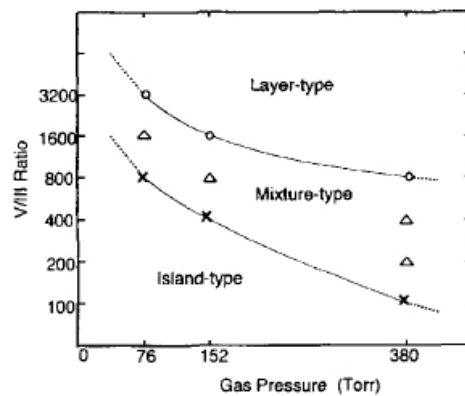


Fig 1.2 Growth mode for the initial stage of GaP on Si under different V/III ratios and pressures, after Ref. [19].

Table 1.1 Prior work concerning growth of GaP on Si by OMCVD

Reference	T (°C)	P (Torr)	Flow rate (l/min)	Precursors			Growth Rate (nm/s)	Pretreatment in H ₂	Structure Characterization	Notes
				P _{III} (Torr)	P _V (Torr)	V/III				
Andre et al. [1]	800	-	1.1	0.9	17.5	20	5.6	1180 °C, with HCl	SEM, X-ray Topography	3°-4°; PH ₃ preflow
Pogge et al. [2]	750 - 1000	-	6	-	-	-	5.0	1100 °C, 2 min	SEM, Optical	3° miscut
Beneking et al. [3]	700 - 900	-	6	-	-	4	1.1 - 2.5	1100 °C, 2 min	Optical	PH ₃ precracking
Su [4]	660	-	1	-	-	13	5	1200 °C		(111); TEG
Samuelson et al. [5]	800	760	4	0.076	0.76	10	1.7	1150 °C, 30 min	SEM	PH ₃ preflow
Olson et al. [6]	500 750	760	3	-	-	-	0.17 - 1.7	1000 - 1100°C	TEM, SEM	2°; 2 steps growth
Sugo et al. [7]	450 730	70	5	-	-	60	0.11 - 0.19 0.56	900 - 1000°C, 10 min	SEM, Optical	TEG ; 4°; 2 steps growth
Bell et al. [8]	610	60	10.15	0.00036	3.6	10000	0.09	-	SE	PH ₃ preflow
Dixit et al. [9]	845	23		-	-	100	0.17	850 °C, 30 min	SEM, Optical, XRD, Raman	Post-growth annealing

Table 1.1 (Continued)

Reference	T (°C)	P (Torr)	Flow rate (l/min)	Precursors			Growth Rate (nm/s)	Pretreatment in H ₂	Structure Characterization	Notes
				P _{III} (Torr)	P _V (Torr)	V/III				
Kohama et al. [10]	900	760	6	-	-	100	0.83	1100 °C	SEM, XRD, SIMS	2°; AsH ₃ preflow
Kohama et al. [11]	500	76	180 - 540	0.13 - 0.38	38	100 - 300	5.7	1000°C, 10 min	TEM, SEM	AsH ₃ preflow
Imaizumi et al. [12]	900	760	-	-	-	800	0.92	1000°C, 15 min	SEM, Optical	2°; 2D and 3D growth mode vs. V/III
Soga et al. [14]	900	76	-	-	-	3200	0.25	1000°C, 10 min	TEM	2°; P adsorption and clusters size vs. V/III
Soga et al. [15]	900	760	-	-	-	3200	0.67	1000°C, 10 min	TEM, Optical	2°; Ga _x P _y cluster vs. V/III
Suzuki et al. [17]	900	76 - 380	2 - 2.5	-	-	3200	0.16 - 0.31	-	Optical	4°; stable reactant density vs. V/III
Soga et al. [18]	900	76 - 380	-	-	-	3200	0.1 - 0.6	-	Optical	4°; growth mode vs. V/III and P

1.2.2 Heteroepitaxy of GaP on Si by other techniques

Heteroepitaxy of GaP on Si has been realized using techniques other than OMCVD. For example, Gong et al. [20] used atomic layer epitaxy (ALE) at atmospheric pressure and 600°C with TMG and PH₃ precursors, demonstrating single-crystal (001) GaP films about 30 nm thick with smooth morphology grown on (001) Si with 3° miscut. These samples were characterized by TEM and SEM. Also, Choi et al. [21, 22] used plasma-enhanced chemical vapor deposition (PECVD) at 1 Torr and 390 to 620 °C with precursors of TMG and plasma-generated phosphorous subhydrides. GaP epilayers with good qualities were obtained, and were characterized by AES, SEM, XRD, and SIMS.

Various high-vacuum techniques have also been explored, such as molecular beam epitaxy (MBE) [23-26, 30, 31], gas-source molecular beam epitaxy (GSMBE) [27], migration-enhanced epitaxy (MEE) [28, 29] and chemical beam epitaxy (CBE) [32-34]. Although the optimum growth temperatures of these methods are usually several hundreds of degrees lower than those used in OMCVD, a two-step growth process starting with a low-temperature buffer layer is recommended, as it results in better-quality GaP than that obtained by direct growth [27, 28].

Wright et al. [25, 26] have proposed using Si substrates with (211) orientations as a way of maintaining interface charge neutrality and providing site selections for the adjacent incorporation of Ga and P atoms, thus suppressing the formation of anti-phase domains (APDs). They showed that GaP films grown on (211) Si by MBE are free of APDs as revealed by anisotropic etching, and that the range of suitable growth temperatures is extended relative to that seen with other orientations.

Bachmann and coworkers [33, 34] studied extensively the CBE of GaP on (001) Si using triethylgallium (TEG) and tertiary-butyl phosphine (TBP) precursors. The growth process was monitored in real time using single-wavelength p-polarized reflectance (PR) and

laser light scattering (LLS). Together with the *ex situ* AFM measurements, they found that the film morphology is directly related to the initial Ga supersaturation level, which is determined by the TEG input flux [34]. At small initial Ga supersaturations, GaP grows as widely spaced 3D islands. Although these coalesce at large aspect ratios (height to radius), the result is a film with large roughness. Increasing the initial Ga supersaturation increases the nucleation density and reduces the time to coalescence. Thus a continuous layer can be formed at an early stage, and the final film exhibits a smooth morphology. However, increasing the Ga supersaturation further results in the formation of Ga droplets, and the film becomes rough, as seen from the rapid increase of LLS intensities. Although the growth conditions in CBE are very different from those in OMCVD, the dependences of nucleation and growth on the initial Ga supersaturation are very similar.

1.2.3 Growth Chemistry

Stringfellow and coworkers studied the decomposition of the precursors PH_3 and trimethylindium (TMI), and the growth chemistry of InP, GaAs, and GaP [35-39]. They also reviewed the earlier works by others on the decomposition of various precursors. Specifically, Larsen et al. [35] used mass spectroscopy to study heterogeneously catalyzed PH_3 decomposition by passing it through a 41.5 cm long silica tube with a 4 mm inner diameter. In some cases these were packed with additional SiO_2 or InP chips to increase surface area. Their results are presented in Fig 1.3, which is after Ref. [35]. The decomposition temperature is significantly reduced when the SiO_2 surface area is increased from 60 cm^2 to 300 cm^2 , or when the 60 cm^2 SiO_2 surface is coated with InP. They also found that no HD exists in the final products when D_2 is used as a carrier gas. Therefore, PH_3 decomposition occurs heterogeneously over SiO_2 or InP. This reaction is found to be first order in PH_3 , with an activation energy of 1.56 eV (36 kcal/mol) [35] on InP. Other

activation energies were determined to be 1.99 eV (46 kcal/mol) [35] or 1.92 eV (44.2 kcal/mol) [40] on SiO₂, and 2.40 eV (55.3 kcal/mol) [40] on Si. The above numbers are all less than the PH₂-H bond strength of 3.92 eV (90.3 kcal/mol), which indicates the effects of bond weakening exerted by the various heterogeneous surfaces [35].

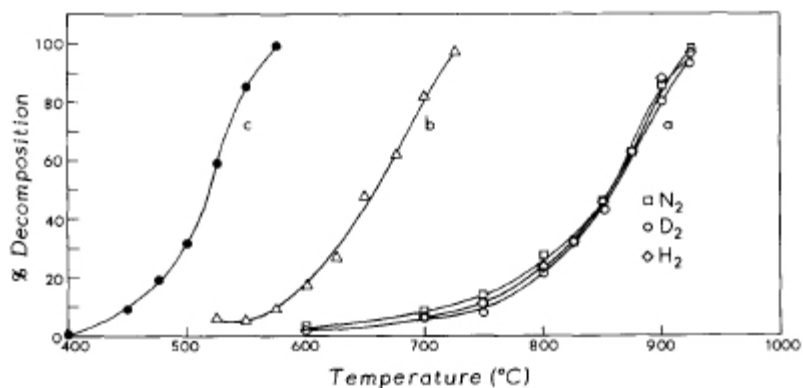


Fig 1.3 PH₃ decomposition catalyzed by (a) 60 cm² SiO₂, (b) 300 cm² SiO₂, and (c) 60 cm² InP, after Ref. [35].

Buchan et al. [36, 37] found that the PH₃ decomposition temperature is further reduced in the presence of TMI and also with increasing surface area of InP, as shown in Fig. 1.4 [37]. An interesting point is that for PH₃/TMI = 4.2, approximately the same amount of TMI (100%) and PH₃ (25%) are decomposed at 325 °C, after which the shape of (b) resembles that of (a), for which no TMI is present. Also, they found that by using D₂ as a carrier gas only CH₄ is detected, although the decomposition of TMI alone generates CH₃D. They proposed the growth mechanism of InP from TMI and PH₃ as follows [37]. For temperatures below 400 °C, adducts of (CH₃)₃In : PH₃ are formed on InP surface through either homogeneous reactions in the gas phase followed by adsorption, or heterogeneous reactions of individually adsorbed species. This is known as the Langmuir – Hinshelwood (LH) mechanism. The adducts are then reduced heterogeneously through CH₄ eliminations. For temperatures

above 400 °C, adduct formation is primarily homogeneous followed by the elimination of the first CH₄ molecule. Further CH₄ eliminations in (CH₃)₂In – PH₂ can occur either homogeneously or heterogeneously.

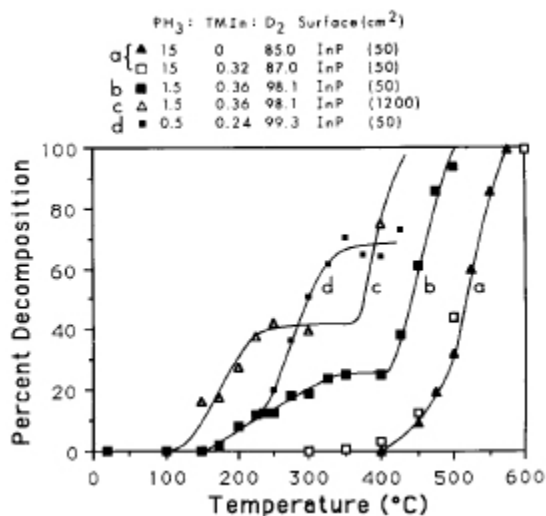


Fig 1.4 PH₃ decomposition (a) without TMI and with (b) PH₃/TMI = 4.2, (c) PH₃/TMI = 4.2 with InP surface area of 1200 cm², and (d) with PH₃/TMI = 2.1, after Ref. [37].

The same group of authors studied the system AsH₃ and TMG, and found similar behavior as the above [38, 39]. The decomposition of AsH₃ alone happens heterogeneously over SiO₂ or GaAs, and no HD appears in the decomposition products when D₂ is used as a carrier gas. The decomposition of TMG alone is homogeneous and generates CH₃D. When both AsH₃ and TMG are decomposed together, only CH₄ is detected without any CH₃D or C₂H₆. H₂ is also present when AsH₃/TMG > 1. The decomposition temperature is lowered when the GaAs surface area is increased, which indicates a heterogeneous process. TMG decomposition data are given in Fig. 1.5 (after Ref. [38]).

The authors did not detect any adduct formation using mass spectrometry. They explained this as being due to the weak bonding of (CH₃)₃Ga : AsH₃, consistent with the fact

that the bond strength for the similar system of $R_3M : LR_3'$ varies as $N > P \gg As > Sb > Bi$, with $M = Ga$ or In and $R, R' = CH_3$ [39]. Therefore, the authors proposed that the growth of GaAs follows the LH mechanism, where individual adsorbed TMG and AsH_3 react to form an adduct followed by the CH_4 removal [39].

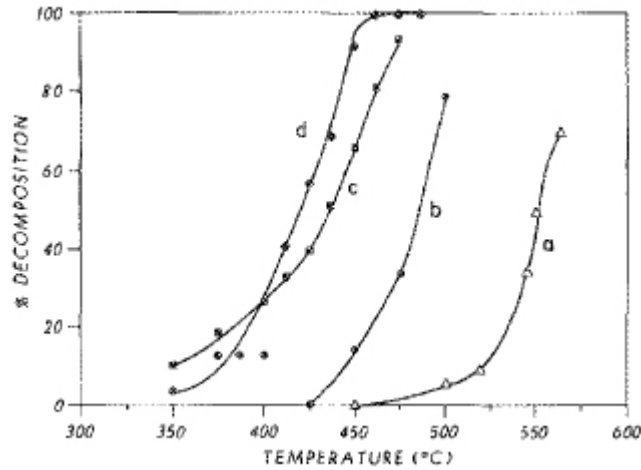


Fig 1.5 TMG decomposition with (a) N_2 [41], and $AsH_3/TMG/D_2 =$ (b) 0/0.6/99.4, (c) 0.3/0.3/99.3, and (d) 3.3/0.3/96.3, after Ref. [38]

Jacko and Price [42] studied the homogeneous decomposition of TMG. They found that the first and second methyl detach at $500^\circ C$ and $550^\circ C$, with activation energies 2.58 eV (59.5 kcal/mol) and 1.54 eV (35.41 kcal/mol), respectively. They calculated the Ga-C bond strength in the monomethyl gallium (MMG) to be 3.36 eV (77.5 kcal/mol). However, for TMG adsorbed on GaAs, the bond strength is only 1.13 eV (26 kcal/mol) [43] or 1.08 eV (25 kcal/mol) [44]. A more comprehensive review including the data above is provided by Larsen et al. [39].

The mechanisms for the homogeneous and heterogeneous growth of GaAs using AsH_3 and TMG have also been studied by other groups [45-49]. The formation of an intermediated adduct was detected by infrared adsorption spectroscopy [47].

1.2.4 Heteroepitaxy on patterned Si

The work reviewed above all uses commercial Si wafers, which are usually given several standard chemical treatments before epitaxy and are nominally flat without surface patterns. However, heteroepitaxy on patterned Si has also been studied.

Gorbach et al. [52, 53] generated patterned (001) Si substrates by chemical etching in 10% KOH solutions at 80 °C for 10 – 30 min or HF:HNO₃ = 10:1 solutions at room temperature for 5 to 30 s. The final morphologies are convex tetragonal pyramids and concave rough hemispherical plates respectively. They grew GaAs and GaP on these patterned Si substrates at room temperature using pulsed vacuum thermal deposition [52] and HgCdTe at 220 and 270 °C using pulsed laser deposition [53]. However, film quality was evaluated only by SEM.

Bakin et al. [54] studied the low-pressure (LP) OMCVD growth (15 – 75 Torr) of InP on patterned Si substrates generated by: (1) etching in 4.5% NaOH solutions with 5% (vol) 2-propanol at 90°C for 45 min; (2) first covering the surface with InP islands then etching in the above solution or 30% KOH solutions at 60°C; (3) etching in boiling deionized H₂O for 10 – 40 min; and (4) growing oxides of 0.5 – 1 μm thicknesses followed by removal then pre-epitaxy cleaning with 5 min in H₂SO₄:H₂O₂:H₂O = 5:1:1 and 30 s in HF. The morphology and characteristic scale for the various patterns are: (1) pyramids exposing four {111} facets with base dimension ~ μm; (2) pyramids exposing four {111} facets with base dimension ~ 100 nm for NaOH etching, and conical exposing multiple facets with base dimension ~ 100 nm for KOH etching; and (3, 4) nanopatterns with RMS roughness 0.34 – 0.7 nm, which however are highly sample dependent and hence are due to intrinsic defects in the substrate materials. The growth of InP on patterned Si generated by method (1) was found to contain a high density of defects including twins, threading dislocations, and APDs. The first two primarily originated from the {111} facets of Si pyramids, as revealed by TEM.

Patterned Si substrates generated by method (2) resulted in the growth of very inhomogeneous layers. The best results came from growth on nanopatterned Si generated by methods (3) and (4). APD free InP epilayers were obtained by optimizing the pattern roughness, as revealed by optical microscopy.

Hashimoto et al. [55] studied the two-step LPOMCVD growth of GaAs on (001) Si patterned with μm -scale V-grooves exhibiting $\{111\}$ facets, which were generated by etching with KOH solution at 70°C using 200 nm Si_3N_4 masks. They found that GaAs layers grow only on (001) planes and that no growth occurs inside the grooves. However, Sprung et al. [56] were able to grow a smooth GaAs layer on (001) Si sawtooth-patterned with $\{111\}$ facets by MBE using the two-step method. Korst et al. [57] also studied two-step LPOMCVD growth of InP and GaAs on grooved (001) Si. Material quality was found to be better than that for films grown on planar (001) Si.

The selective-area growth of GaAs on (001) Si patterned with an oxide overlayer has been studied extensively [58-60]. The density of defects such as threading dislocations and stacking faults can be controlled using this method [59].

Another special point of interest is the CVD growth of diamond on Si. Scratching the Si surface with various abrasives (powder of diamond, BN, SiC, or Al_2O_3 , etc.) is found to increase the nucleation density by several orders of magnitude [61]. Thus the rough morphologies and defects associated with a work damaged silicon surface appear to be the favored nucleation sites for diamond [62].

1.2.5 Lateral thickness variations

Different growth behaviors and rates over different regions for samples grown in horizontal OMCVD reactor are frequently been observed, e.g., in the work of GaP heteroepitaxy on Si by Suzuki et al. [17] and Soga et al. [12], as reviewed in Sec. 1.2.1.

Saxena et al. [63] plotted the growth rates of GaAs homoepitaxy along the gas flow direction, which is seen to be largest near the upstream, constant for a wide range in the middle with a stable boundary layer, and lowest near the downstream. Interestingly, Sato et al. [64] found that the growth rates are inversely proportional to the thickness of the boundary layer, which has a square root dependence on the distance from the susceptor edge. This is exactly what is been expected for growth under a diffusion-limited mode in a horizontal reactor, as we will show in Eq. (2.1.2.18).

Moreover, Costrini et al. [65] studied the lateral thickness variations resulted from GaAs epitaxy using TMG and AsH₃ as precursors in a vertical-flow OMCVD reactor. The 2” wafer covers the susceptor entirely and is rotated at a speed of 25 rpm. The growth conditions they varied include H₂ carrier gas flow rate, growth temperature, and TMG input rate. In either case an edge with thickness thinner than the center was observed. They ascribed the reason to be due to the reactants depletion, which for temperatures below 700 °C is resulted from the insufficient TMG source input supply in the mass transport-limited growth regime without a fully developed diffusion boundary layer [66], and for temperatures above 700 °C is resulted from the parasitic depositions on the wall.

As seen from the above, although lateral thickness variations in OMCVD are commonly reported, these are always attributed to depletion of reactants in the gas phase, and not connected to catalytic decomposition on different types of surfaces. As we shall show in Ch. 4, the distinguishing feature is an exponential dependence of the thickness variation on radius in the case of circular wafers. A similar dependence should be observable in horizontal-flow reactors, although to our knowledge this has not been reported so far.

Chapter 2 Theory

This chapter provides a brief overview of the theoretical background for our experiment, especially on OMCVD and polarimetry. Section 2.1 introduces the fundamental aspects of OMCVD, including thermodynamics, homogeneous gas-phase processes of mass transport and kinetics, and heterogeneous surface processes of nucleation, surface diffusion, and epitaxy. Section 2.2 discusses the principles of spectroscopic polarimetry measurements, including the Jones-matrix formalism of the polarimeter system, two-, three- and four-phase models, and dielectric functions. Other topics such as the Bruggeman effective medium approximation and spectrum analysis near critical point energies are also covered.

2.1 OMCVD

2.1.1 Thermodynamics

Thermodynamics provides the underlying force driving growth, which governs the phase transition from the gas phase of various precursor species to the solid phase of the desired epitaxial material. The discussion of OMCVD thermodynamics can be found in Ref. [67-69]. Some important points are summarized here.

Under typical OMCVD growth conditions of constant temperature and pressure, the two-phase equilibrium condition is expressed as the minimization of the Gibbs free energy G , which is given by:

$$G = H - TS = E + PV - TS \quad (2.1.1.1)$$

where H is the enthalpy, S the entropy, E the internal energy, and P , V , T the pressure, volume and temperature, respectively. Using Maxwell's relation $dE = TdS - PdV$, the above can be

written in the differential form as:

$$dG = dE + VdP + PdV - SdT - TdS = VdP - SdT . \quad (2.1.1.2)$$

Since T is a constant and from the ideal gas law $PV = nRT$,

$$dG = nRTd(\ln P) . \quad (2.1.1.3)$$

Thus the chemical potential with reference to the standard state is:

$$\mu = \frac{\partial G}{\partial n} = \mu_0 + RT \ln a . \quad (2.1.1.4)$$

Here the activity a is defined as:

$$a = \frac{xP}{P_0} = \frac{P_x}{P_0} \quad (2.1.1.5)$$

for the gas phase where x is the mole fraction and P_x the partial pressure, and

$$a = \frac{x}{x_0} = x \quad (2.1.1.6)$$

for solid and liquid phases, where $x_0 = 1$ for the pure form in the standard state.

For a transition process of A to B, the thermodynamic driving force is the difference in the chemical potential:

$$\Delta\mu = \mu_B - \mu_A = \mu_{B0} - \mu_{A0} + RT \ln \frac{a_B}{a_A} . \quad (2.1.1.7)$$

In equilibrium $\Delta\mu = 0$, so

$$\mu_{B0} - \mu_{A0} = -RT \ln \frac{a_B^{eq}}{a_A^{eq}} . \quad (2.1.1.8)$$

Thus the equilibrium concentration of A and B can be related to the difference in the chemical potential between the standard states as

$$\frac{n_B^{eq}}{n_A^{eq}} = \frac{a_B^{eq}}{a_A^{eq}} = \exp\left(-\frac{\Delta\mu_0}{RT}\right) . \quad (2.1.1.9)$$

Also Eq. (2.1.1.7) becomes:

$$\Delta\mu = RT \ln \frac{a_B / a_B^{eq}}{a_A / a_A^{eq}}. \quad (2.1.1.10)$$

Here we only follow one species. Generalization to real growth involving multiple species and is given by summation.

For the special case of a transition from vapor to solid, the above can be written as

$$\Delta\mu = RT \ln \frac{P_S / P_S^{eq}}{P_V / P_V^{eq}} = RT \ln \frac{P_S}{P_V} = -RT \ln(1 + S_{sat}), \quad (2.1.1.11)$$

where the degree of supersaturation S_{sat} is defined by

$$S_{sat} = \frac{P_V - P_S}{P_S}. \quad (2.1.1.12)$$

Here P_S is the saturated pressure above the solid and P_V the supersaturated pressure in the ambient vapor phase. In OMCVD S_{sat} is always positive, so $\Delta\mu$ is always less than zero and a chemical driving force always exists. Another practical form of Eq. (2.1.1.11), which depends on the number of atoms N instead of the molar concentration is the free energy change per unit volume ΔG_V :

$$\Delta G_V = \frac{kT}{\Omega} \ln \frac{P_S}{P_V} = -\frac{kT}{\Omega} \ln(1 + S_{sat}), \quad (2.1.1.13)$$

where Ω is the atomic volume, and $\Delta\mu = n_A \Omega \Delta G_V$.

2.1.2 Gas phase process

Although thermodynamics determines the extent of the overall reaction that can happen during an OMCVD process, the actual growth is often influenced by other factors especially mass transport and kinetics. A maximum growth rate can be estimated from various calculations such as the arrival rates of various reactive species and their gas phase collisions,

which as will be seen later to provide useful insight into the analysis of OMCVD growth.

2.1.2.1 Kinetics theory

Analytic expressions involving various gas-phase kinetic parameters can be derived from basic properties using a simple elastic hard-ball collision model. A detailed discussion on this topic can be found in Ref. [70]. Some important results are presented here.

Gas-phase molecules have classical 1D and 3D Maxwell velocity distributions of:

$$f(v_i) = \sqrt{\frac{m}{2\pi kT}} \exp\left(-\frac{mv_i^2}{2kT}\right), \quad i = x, y \text{ or } z \quad (2.1.2.1)$$

and

$$f(v) = 4\pi \left(\frac{m}{2\pi kT}\right)^{3/2} v^2 \exp\left(-\frac{mv^2}{2kT}\right) \quad (2.1.2.2)$$

respectively, where m is the molecular mass. The average velocity can be calculated as:

$$\langle |v_i| \rangle = \frac{1}{2} \sqrt{\frac{8kT}{\pi m}}, \quad i = x, y \text{ or } z \quad (2.1.2.3)$$

and

$$\langle |v| \rangle = 2\langle |v_i| \rangle = \sqrt{\frac{8kT}{\pi m}}. \quad (2.1.2.4)$$

The arrival rate of molecules with a volume density of N/V on a surface area A in the $+v_x$ direction can be obtained with the help of time interval Δt :

$$J = \frac{\int_0^{+\infty} \frac{N}{V} A v_x \Delta t f(v_x) dv_x}{A \Delta t} = \frac{N}{V} \frac{\int_0^{+\infty} |v_x| f(v_x) dv_x}{2} = \frac{1}{2} \frac{N}{V} \langle |v_x| \rangle = \frac{1}{4} \frac{N}{V} \langle |v| \rangle. \quad (2.1.2.5)$$

Using Eq. (2.1.2.9) and the ideal gas equation $PV = NkT$, the above can be written as:

$$J = \frac{P}{\sqrt{2\pi k m T}}, \quad (2.1.2.6)$$

which is the homogeneous impinging current. Equation (2.1.2.8) can also be viewed as the surface mass transfer flux

$$J = K_s n, \quad (2.1.2.7)$$

where the surface reaction rate K_s which has the form

$$K_s = \gamma \sqrt{\frac{kT}{2\pi m}} \quad (2.1.2.8)$$

where γ is the reaction probability.

The mean free path λ , which is the average distance that a molecule travels between collisions, can be calculated as:

$$\lambda = \frac{\langle |v| \rangle}{\frac{N}{V} \sqrt{2} \langle |v| \rangle \pi d^2} = \frac{1}{\frac{N}{V} \sqrt{2} \pi d^2}. \quad (2.1.2.9)$$

Here $\sqrt{2} \langle |v| \rangle$ is the average relative velocity obtained by using the reduced mass $m/2$, and πd^2 is the collision cross section.

For collisions between different kinds of molecules A and B with an average relative velocity $\langle |v_r| \rangle$, the collision cross section becomes $\pi \left(\frac{d_A + d_B}{2} \right)^2$, and the total number of collisions per unit volume per unit time is:

$$Z_{AB} = \langle |v_r| \rangle \pi \left(\frac{d_A + d_B}{2} \right)^2 \frac{N_A}{V} \frac{N_B}{V}. \quad (2.1.2.10)$$

A simple estimate of the diffusion coefficient can be obtained by calculating the flux between two planes each located one mean free path away ($x = \pm \lambda$) from the reference plane ($x = 0$):

$$J_x = \frac{1}{4} \langle |v| \rangle \left(\frac{N}{V} \right)_{- \lambda} - \frac{1}{4} \langle |v| \rangle \left(\frac{N}{V} \right)_{+ \lambda} = -\frac{1}{2} \langle |v| \rangle \lambda \frac{d \left(\frac{N}{V} \right)}{dx}, \quad (2.1.2.11)$$

then integrating over all fluences from $x = 0$ to $x = \pm \infty$. We obtain:

$$J_x = -\frac{3\pi}{16\sqrt{2}} \langle |v| \rangle \lambda \frac{d\left(\frac{N}{V}\right)}{dx} \quad (2.1.2.12)$$

which compared to $J_x = -D \frac{d\left(\frac{N}{V}\right)}{dx}$ gives

$$D = \frac{3\pi}{16\sqrt{2}} \langle |v| \rangle \lambda. \quad (2.1.2.13)$$

Using an estimation method similar to that above, the viscosity coefficient (or dynamic viscosity) can be calculated:

$$\mu = \frac{1}{2} m \langle |v| \rangle \lambda \frac{N}{V} = \frac{1}{\pi d^2} \sqrt{\frac{mkT}{\pi}}, \quad (2.1.2.14)$$

and also the kinematic viscosity:

$$\nu = \frac{\mu}{\rho}. \quad (2.1.2.15)$$

Here ν has the dimension of a diffusion coefficient (m^2/s).

2.1.2.2 Dimensionless numbers

Many dimensionless numbers have been defined to facilitate the description of OMCVD [68]. Here we present only the most important four, which are relevant to our interests: the Knudsen, Reynolds, Péclet, and Damköhler numbers. These are summarized from Refs. [68, 72].

The Knudsen number (Kn) is defined as the ratio of mean-free path in the gas to a characteristic length L_c of the system:

$$Kn = \frac{\lambda}{L_c}. \quad (2.1.2.16)$$

The assumption of a fluid flow is only valid if $Kn \ll 1$.

The Reynolds number (Re) is defined by comparing the system diameter L_d and the length $\sqrt{\nu t}$ characteristic of the kinematic viscosity:

$$Re = \left(\frac{L_d}{\sqrt{\nu t}} \right)^2 = \frac{L_d^2}{\frac{\mu}{\rho} \frac{L_d}{\rho u}} = \frac{\rho u L_d}{\mu} \quad (2.1.2.17)$$

where ρ is the mass density (kg/m^3), u the average gas velocity resulting from advection (m/s), and μ and ν are the dynamic ($\text{kg}\cdot\text{m}^{-1}\cdot\text{s}^{-1}$) and kinematic (m^2/s) viscosities, respectively. The value of Re reflects the flow characteristics, as summarized in Table 2.1 [73]. Using Re, the thickness of the boundary layer in a horizontal-flow reactor can be readily obtained:

$$\delta(x) = \sqrt{\nu t} = \sqrt{\frac{\mu}{\rho} \frac{x}{u}} = \sqrt{\frac{\mu}{\rho u L_d} x L_d} = \sqrt{\frac{x L_d}{Re}}. \quad (2.1.2.18)$$

Table 2.1 Typical flow characteristics with different Reynolds numbers [73].

Reynolds number (Re)	Flow characteristics
$Re < 4$ to 25	Laminar flow with straight streamlines
$4 < 25 < Re < 1000$ to 2100	Laminar flow with rippling
$1000 < 2100 < Re < 4000$	Transient flow
$Re > 4000$	Turbulent flow

The Péclet number (Pe) is defined by the ratio of the system length in the direction of interest L , to the characteristic diffusion length \sqrt{Dt} :

$$Pe = \left(\frac{L}{\sqrt{Dt}} \right)^2 = \frac{L^2}{D \frac{L}{u}} = \frac{uL}{D}, \quad (2.1.2.19)$$

where D the diffusion coefficients (m^2/s). Pe is a measure of the relative importance of mass transport by advection and diffusion. If Pe is much larger (smaller) than 1, advection (diffusion) dominates and diffusion (advection) will have negligible effect. But when Pe is at intermediate values, mass transport by advection and diffusion are both important. In this case downstream reactants could diffuse back in the growth of upstream and affect the reaction there. We will show examples of this in the growth of GaP on nrSi. It can be seen that Pe is directly proportional to the system length scale L . Therefore larger L will give a larger Pe , which means that advection will eventually dominate over diffusion if the gas travels far enough. This follows because the displacements due to advection and diffusion have time dependences of t and $t^{1/2}$, respectively [74].

The Damköhler number (Da) is defined by the ratio of the surface reaction rate to the diffusion rate:

$$Da = \frac{K_s}{D/H} = \frac{K_s H}{D}, \quad (2.1.2.20)$$

where K_s is the surface reaction rate (m/s) given by Eq. (2.1.2.8), which has the dimension of a velocity, and H is the characteristic height (m) over which diffusion occurs. Above the growing surface we have the vertical diffusion current ($\text{m}^{-2}\text{s}^{-1}$)

$$J_D = \frac{D}{H}(n_0 - n_s), \quad (2.1.2.21)$$

and the mass transfer flux ($\text{m}^{-2}\text{s}^{-1}$)

$$J_{MT} = K_s(n_s - n_{eq}). \quad (2.1.2.22)$$

A schematic view of these two quantities with slightly different notations is given in Figure 2.1.1 after Ref. [71]. In steady state $J_D = J_{MT}$, so we have

$$n_s = \frac{n_0}{1 + \frac{K_s H}{D}} + \frac{n_{eq}}{1 + \frac{D}{K_s H}} = \frac{n_0 + n_{eq} Da}{1 + Da}, \quad (2.1.2.23)$$

where n_0 and n_s are the bulk- and surface-nutrient densities (m^{-3}), respectively. Thus the value of Da reveals the growth-rate-limiting mechanism. If $Da \gg 1$, n_s will be close to zero, so the surface reaction is rapid comparing to diffusion. Then growth will be mass-transport limited. If $Da \ll 1$, n_s will be close to n_0 , so diffusion is rapid comparing to the surface reaction rate. Then growth will be kinetically limited.

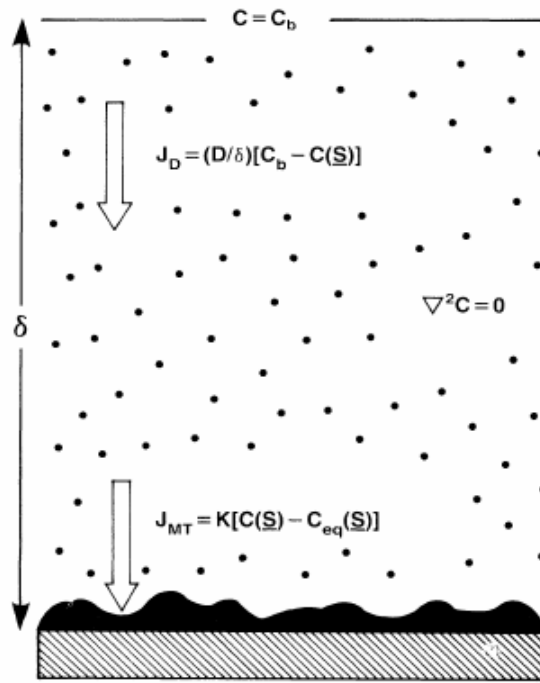


Fig 2.1.1 Schematic view of diffusion and mass transfer currents, after Ref. [71].

2.1.2.3 Simple growth analysis using the continuity equation

Simple growth analysis based on mass conservation using the continuity equation can

provide insight into the OMCVD process. For example, the lateral thickness profile under some conditions can be adequately explained using the results developed in this section. The approach here is similar to that of Ref. [72].

We will concentrate on the reactive nutrient species that is responsible for the growth. Assume that the reactant source supply arrives only from the lateral direction, and that its vertical-transport component occurs by diffusion only. Then it is possible to choose a small volume above the growing surface where no flux either enters or leaves the top surface. Since the bottom surface is bounded by the sample, no flux is exchanged there either. Also, the vertical diffusion current \vec{J}_D is purely an internal effect. Thus the 3D continuity equation can be reduced to 1D along the lateral direction. This has a differential form

$$\nabla \cdot \vec{I} + \frac{\partial n}{\partial t} = G, \quad (2.1.2.24)$$

where \vec{I} is the current, n the concentration, and G the generation rate, which is negative in the case of recombination. Here we use \vec{I} to represent the lateral current in order to distinguish it from the vertical current \vec{J} and the vertical diffusion current \vec{J}_D .

In the case of $Pe \ll 1$, lateral transport is dominated by the diffusion current, which comes from the lateral density variations:

$$\vec{I}_D = -D\nabla n_D = -D \frac{\partial n_D}{\partial x} \hat{x}. \quad (2.1.2.25)$$

The diffusion coefficient D is assumed to be the same for both vertical and horizontal directions. The generation rate G actually represents the removal rate of the nutrient species inside the volume, and it has the form of an exponential decay in time with constant τ :

$$G = -\frac{n_D}{\tau}. \quad (2.1.2.26)$$

Assuming that the nutrient removal is through deposition only, and also assuming mass-transport-limited growth with surface reactions being more rapid than vertical diffusion ($Da \gg 1$), the above becomes

$$G = -\frac{J_D}{H} = -\frac{Dn_D}{H^2} = -\frac{n_D}{\tau}, \quad (2.1.2.27)$$

where H is the height of the region we choose, and the time constant τ is given as

$$\tau = \frac{H^2}{D}. \quad (2.1.2.28)$$

Other nutrient removal mechanisms may also exist, e.g., thermal decomposition. For the coexistence of two time constants, an effective τ is defined by

$$\frac{1}{\tau} = \frac{1}{\tau_1} + \frac{1}{\tau_2}, \quad (2.1.2.29)$$

and the value of which is mainly determined by the smaller one of τ_1 and τ_2 .

Under steady-state conditions

$$\frac{\partial n_D}{\partial t} = 0. \quad (2.1.2.30)$$

Using the above formulae the continuity equation (2.1.2.24) becomes

$$-D \frac{\partial^2 n_D}{\partial x^2} = -\frac{n_D}{\tau}, \quad (2.1.2.31)$$

with solutions

$$n_D(x) = C_D \exp\left(\pm \frac{x}{\sqrt{D\tau}}\right) = C_D \exp\left(\pm \frac{x}{L_D}\right). \quad (2.1.2.32)$$

where the characteristic length L_D is

$$L_D = \sqrt{D\tau} = H. \quad (2.1.2.33)$$

Thus L_D is equal to the distance over which diffusion occurs. Here n_D has two solutions, with the exponent taking either \pm sign. This means that diffusion flow can travel both ways, either along with or against the advection flow. The process discussed here is actually the mechanism that forms lateral thickness profile of GaP on nrSi(1:1:1).

Similar results can be obtained for the case of $Pe \gg 1$, where advection flow dominates diffusion for the lateral mass transport. If we also assume that vertical diffusion is rapid

compared to the surface reaction, then

$$\bar{I}_A = n_A U \hat{x}, \quad (2.1.2.34)$$

$$U \frac{\partial n_A}{\partial x} = -\frac{n_A}{\tau}, \quad (2.1.2.35)$$

$$n_A(x) = C_A \exp\left(-\frac{x}{U\tau}\right) = C_A \exp\left(-\frac{x}{L_A}\right), \quad (2.1.2.36)$$

$$L_A = U\tau = \frac{UH^2}{D}, \quad (2.1.2.37)$$

where τ has the same form as in Eq. (2.1.2.28). Here n_A has only one solution, the one that has the negative sign in the exponential term, where the $+x$ direction is defined as that of the advection flow. Here, the nutrient concentration that has been carried by lateral advection decreases exponentially if not replenished in the vertical directions.

For the case of intermediate Pe , where both advection and diffusion exist, the solution will be a combination of the above, with n depending on both the relative values of the pre-exponential factors and the characteristic lengths.

For the case of kinetically limited growth, where diffusion is more rapid than surface reactions ($Da \ll 1$), the density gradient is very small and the reactant concentration is approximately homogeneous. The nutrient removal rate in Eq. (2.1.2.27) will be described in a different way:

$$G = -\frac{K_s n}{H} = -\frac{n}{\tau'}, \quad (2.1.2.38)$$

where τ' is the time constant

$$\tau' = \frac{H}{K_s}. \quad (2.1.2.39)$$

The characteristic lengths in (2.1.2.33) and (2.1.2.37) for $Pe \ll 1$ and $Pe \gg 1$ become

$$L'_D = \sqrt{D\tau'} = \sqrt{\frac{DH}{K_s}} \quad (2.1.2.40)$$

$$L'_A = U\tau' = \frac{UH}{K_s}. \quad (2.1.2.41)$$

In reality, the nutrient could also arrive from the top of the stagnant layer. Thus to get a complete nutrient-density distribution we would have to solve the time-dependent 2D continuity equation by considering the vertical direction as well. Discussions of more complicated situations can be found in Refs. [72, 73].

Taking the above 1D case with $Pe \gg 1$ and $Da \gg 1$ as an example, we further discuss the situation where the generation of nutrients along the flow path is considered. The generation rate from a point source located at $x = x_0$ can be described by the δ function as

$$G_s = N_0\delta(x - x_0). \quad (2.1.2.42)$$

Here N_0 (s^{-1}) is the number of nutrient molecules generated per unit time. When Eq. (2.1.2.42) inserted into the continuity equation and again assuming steady-state conditions, Eq. (2.1.2.31) becomes

$$-D \frac{\partial^2 n_D}{\partial x^2} = -\frac{n_D}{\tau} + N_0\delta(x - x_0). \quad (2.1.2.43)$$

The above has the solution

$$n_D(x) = C \exp\left(-\frac{|x - x_0|}{L}\right). \quad (2.1.2.44)$$

where $L = \sqrt{D\tau}$, and $C = \frac{N_0 L}{2D}$. The connection between C and the system parameters is obtained by substituting Eq. (2.1.2.44) back into Eq. (2.1.2.43) and integrating over an infinitesimal region around x_0 .

Integrating Eq. (2.1.2.44) with respect to x_0 from $-\infty$ to $+\infty$ gives

$$N_D(x) = \frac{N_0 L^2}{D}, \quad (2.1.2.45)$$

which is a constant over x . Physically this means that if the source is generated at an equal

rate over the entire 1D space, the nutrient concentration will be a constant. However, suppose that the source generation only comes from half of the 1D space from $-\infty$ to a , integrating Eq. (2.1.2.44) over this region gives

$$N_D(x) = \frac{N_0 L^2}{2D} \exp\left(-\frac{x-a}{L}\right) \quad (2.1.2.46)$$

Thus an exponentially distributed nutrient concentration can be obtained. Generalization to more regions with different source generation rates is straightforward.

2.1.3 Surface processes

2.1.3.1 Adsorption and surface diffusion

Discussions of adsorption and surface diffusion can be found in Refs. [67-69, 76]. Some useful results are summarized here.

The atoms or molecules impinging on a surface can be either physisorbed, chemisorbed, or return to the gas phase, as shown in Fig. 2.1.2 after Ref. [69]. The reference state $E_p = 0$ is the diatomic form of Y_2 , and $\Delta_f H$ is the heat of formation of two Y atoms. The physisorption of Y_2 molecules follows either line a or b, and the dissociative chemisorption of Y_2 in the form of Y atoms follows line c, with desorption energies shown as E_{da} , E_{db} and E_c respectively. As determined by the relative position of intersection, the energy barrier to change from physisorption to chemisorption is E_{ra} for a to c and E_{rb} for b to c. For the former case there is an activation energy E_a for dissociation as well.

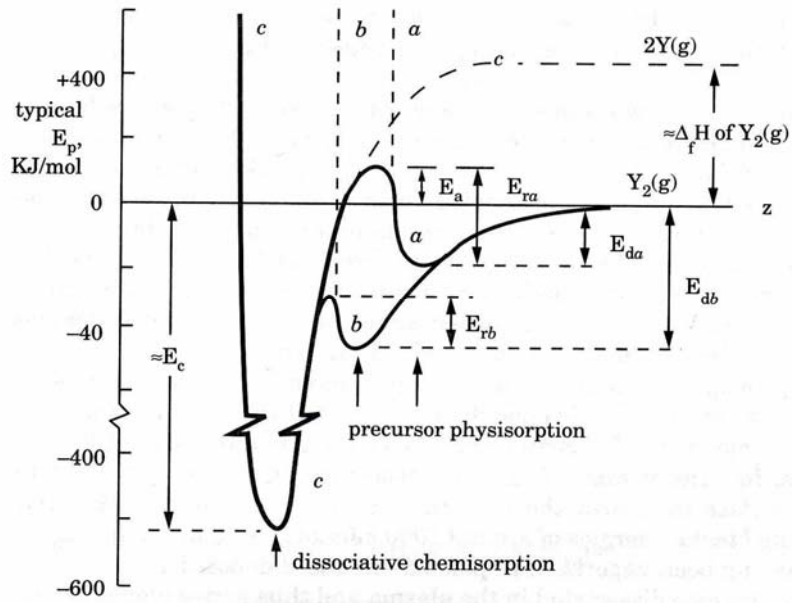


Fig 2.1.2 Precursor adsorption model, after Ref. [69].

For the chemisorbed case, when adsorption and desorption with rate constants k_a and k_d are balanced, then

$$k_a p_i (1 - \theta_i) = k_d \theta_i, \quad (2.1.3.1)$$

where θ_i is the surface coverage and p_i is the partial pressure of species i . The Langmuir isotherm, which describes coverage as a function of partial pressure, is then

$$\theta_i = \frac{K p_i}{1 + K p_i}, \quad (2.1.3.2)$$

where $K = k_a / k_d$ is the surface equilibrium constant. Here θ_i increases with increasing p_i but decreases with increasing T since adsorption is an exothermic process. When $K p_i \ll 1$, $\theta_i \approx K p_i$ and the reaction is first order in p_i . When $K p_i \gg 1$, $\theta_i \approx 1$ and the reaction is zeroth order in p_i .

If two species A and B adsorb at the same time and are in equilibrium, then each can be described by Eq. (2.1.3.1) as

$$k_{aA}p_A(1-\theta_A-\theta_B)=k_{dA}\theta_A, \quad (2.1.3.3)$$

$$k_{aB}p_B(1-\theta_A-\theta_B)=k_{dB}\theta_B. \quad (2.1.3.4)$$

When solved these give the Langmuir-Hinshelwood isotherm:

$$\theta_A = \frac{K_A p_A}{1 + K_A p_A + K_B p_B}, \quad (2.1.3.5)$$

$$\theta_B = \frac{K_B p_B}{1 + K_A p_A + K_B p_B}. \quad (2.1.3.6)$$

If the species react to give a third species, then the rate for the surface reaction is:

$$r = k_{AB}\theta_A\theta_B = \frac{k_{AB}K_A p_A K_B p_B}{(1 + K_A p_A + K_B p_B)^2} \quad (2.1.3.7)$$

Suppose next that the average time that an unreacted adatom remains on the surface before desorption is given by

$$\tau_d = \frac{1}{\nu} \exp\left(\frac{E_d}{kT}\right), \quad (2.1.3.8)$$

where E_d is the desorption energy and $\nu = kT/h$ is the vibrational attempt frequency, which is of the order of 10^{13} s^{-1} . Suppose also that an adatom can be incorporated into the solid phase by collisions with nuclei or other adatoms before desorbing. Then during stable growth the average time before incorporation is

$$\tau_i = \frac{n_T}{J_{MT}}, \quad (2.1.3.9)$$

where J_{MT} is the mass transfer flux ($\text{m}^{-2}\text{s}^{-1}$) and n_T is the total adsorption site density (m^{-2}).

We now consider diffusion. Suppose that the adatoms have a concentration C and the minimum traveling step length is a_0 . For growth on a (001) diamond or zinc blende surface, a_0 is usually the lattice constant times $1/\sqrt{2}$. If there is an adatom flux difference between the locations $x = 0$ and $x = a_0$, then we can define the diffusion current J as:

$$J = \frac{1}{4} \nu a_0 C \Big|_{x=0} - \frac{1}{4} \nu a_0 C \Big|_{x=a_0} = \frac{1}{4} \nu a_0 \left\{ C_0 - \left(C_0 + \frac{dC}{dx} a_0 \right) \right\} = -\frac{1}{4} \nu a_0^2 \frac{dC}{dx} \quad (2.1.3.10)$$

We used the factor of 1/4 because diffusion can occur along any of the four directions. Considering the definition of a diffusion coefficient D_0 , we write $J = -D_0 dC/dx$. Then $D_0 = -1/4 \nu a_0^2$, and the surface diffusion coefficient D_s becomes:

$$D_s = D_0 \exp\left(-\frac{E_s}{kT}\right) = \frac{1}{4} a_0^2 \nu \exp\left(-\frac{E_s}{kT}\right), \quad (2.1.3.11)$$

where E_s is the activation barrier for surface diffusion, which is determined essentially by the bonds that need to be broken for the adatoms to move.

The diffusion process has a characteristic length of the form $X_s = \sqrt{4D_s t}$, which is the root-mean-square distance that an adatom travels on the substrate before it is either desorbed or incorporated. If an adatom can only leave by desorption, $t = \tau_d$ and the diffusion length is

$$X_s = \sqrt{4D_s \tau_d} = a_0 \exp\left(\frac{E_d - E_s}{2kT}\right). \quad (2.1.3.12)$$

Usually $E_d - E_s > 0$, since for desorption the bonds between the adatoms and the substrate are fully broken, while for diffusion the adatoms are still partially bonded to the substrate. If an adatom can only be incorporated into the solid phase, then $t = \tau_i$ and the diffusion length is

$$X_s = \sqrt{4D_s \tau_i} = a_0 \sqrt{\nu \frac{n_T}{J_{MT}}} \exp\left(-\frac{E_s}{2kT}\right). \quad (2.1.3.13)$$

This is usually larger than the distance between two stable nuclei.

Alternatively, adatom diffusion can be viewed as a random walk of N_0 steps with step length a_0 :

$$X_s = a_0 \sqrt{N_0} = a_0 \sqrt{k_s t} = a_0 \sqrt{\nu \exp\left(-\frac{E_s}{kT}\right) t}, \quad (2.1.3.14)$$

which gives the same result as above. Here $k_s = \nu \exp\left(-\frac{E_s}{kT}\right)$ is the rate constant of migration, which has the same form as a chemical reaction.

The desorption energy for Ga on (111) Si has been measured to be 2.88 ± 0.2 eV [79]. A (001)Si surface is usually anisotropic due to the (2 x 1) reconstruction, which generates dimer rows. Diffusion is faster along a dimer row than perpendicular to it. The activation energies are of the order of 0.2 to 0.7 eV and 1.7 to 2.8 eV, respectively, for the two situations [80].

Figure 2.1.3 presents dependence of the adatom diffusion length under typical growth conditions at 600°C on (a) the difference between the desorption energy E_d and the activation energy E_s for surface diffusion as given by Eq. (2.1.3.12), and (b) E_s only as given by Eq. (2.1.3.13). These figures describe the situations where diffusion lengths are limited by (a) adsorption and (b) incorporation into the existing nuclei, respectively.

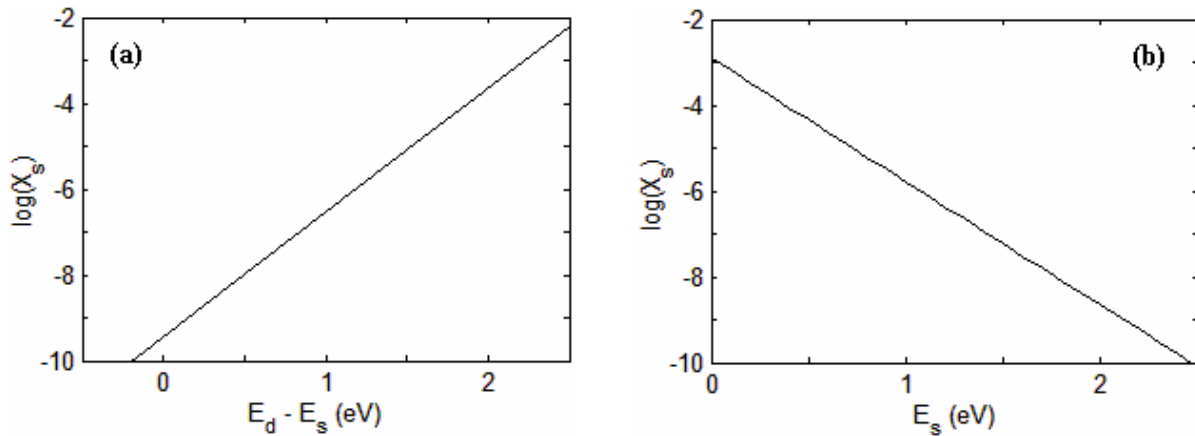


Fig 2.1.3 Dependence of the adatom diffusion length under typical growth conditions at 600°C on (a) the difference between the desorption energy E_d and the activation energy E_s for surface diffusion, and (b) E_s only.

2.1.3.2 Nucleation and the capillarity theory

For a wide range of OMCVD applications, 2D or 3D heterogeneous nucleation processes usually represent the onset of growth. Nucleation can also occur in the gas phase, where it is termed homogeneous. The well-established capillarity theory provides a thermodynamic treatment of nucleation. Here, some important results are summarized and deduced from Refs. [68, 69, 78].

For homogeneous nucleation, the change of total free energy is given by:

$$\Delta G = \frac{4}{3}\pi r^3 \Delta G_v + 4\pi r^2 \gamma \quad (2.1.3.15)$$

where $\Delta G_v = \frac{kT}{\Omega} \ln \frac{P_s}{P_v} = -\frac{kT}{\Omega} \ln(1 + S_{sat})$ is the free energy change per unit volume given by

Eq. (2.1.1.13), and γ is the interfacial energy per unit area. When the system is under equilibrium $d(\Delta G) / dr = 0$, and the critical radius for nucleation r^c and the corresponding ΔG^c are given by:

$$r^c = -\frac{2\gamma}{\Delta G_v}, \quad (2.1.3.16)$$

$$\Delta G^c = \frac{1}{3} A \gamma = \frac{16\pi\gamma^3}{3(\Delta G_v)^2}, \quad (2.1.3.17)$$

with $A = 4\pi(r^c)^2$ the surface area of the critical nucleus. Here ΔG^c can be viewed as the energy barrier for nucleation, and is equal to 1/3 of the surface energy.

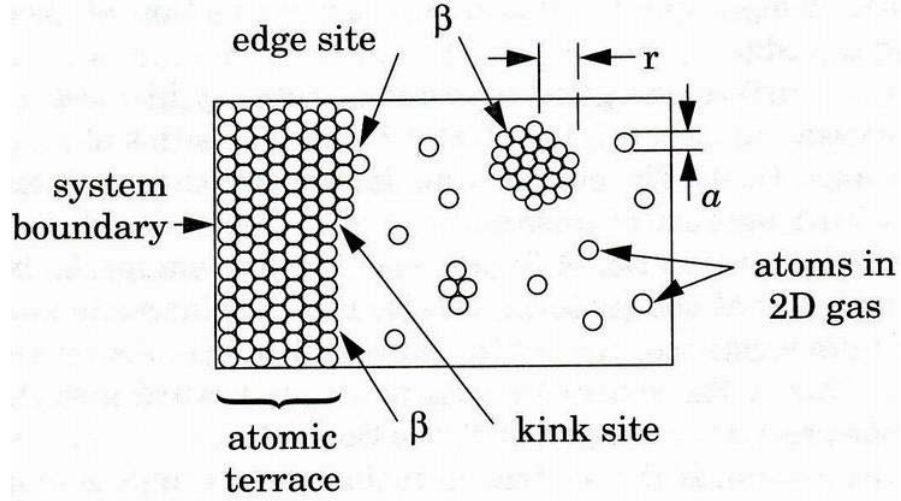


Fig 2.1.4 2D heterogeneous nucleation process, after Ref. [69].

2D heterogeneous nucleation, as in Figure 2.1.4, can be treated similarly as the homogeneous case if we assume that enough adatoms have been adsorbed on the surface, and that they behave like 2D ideal gas. Considering the simplest case where the nucleation material is the same as the substrate, the various surface and interface energies can be viewed to have no change, but we must now consider a new edge energy γ_e (J/m), which is developed around the exposed perimeter of 2D nuclei. Thus the total free energy change is now

$$\Delta G = \pi r^2 h_a \Delta G_v + 2\pi r \gamma_e, \quad (2.1.3.18)$$

where h_a is the height of a 2D nucleus or a monolayer. The quantities r^c and ΔG^c are now

$$r^c = -\frac{\gamma_e}{h_a \Delta G_v}, \quad (2.1.3.19)$$

$$\Delta G^c = \frac{1}{2} L \gamma_e = -\frac{\pi \gamma_e^2}{h_a \Delta G_v}, \quad (2.1.3.20)$$

where $L = 2\pi r$ is the nucleus edge length, and ΔG^c is 1/2 of the edge energy. For ΔG_v Eq. (2.1.1.13) is still valid, but it needs to be modified as follows:

$$\Delta G_v = \frac{kT}{\Omega} \ln \frac{n_e}{n_a} = -\frac{kT}{\Omega} \ln(1 + S_{sat}), \quad (2.1.3.21)$$

where n_e represents the concentration of the adatoms that have the same chemical potential as the edge nuclei, and n_a represents the total concentration of adatoms. Accordingly, the supersaturation S_{sat} is defined as

$$S_{sat} = \frac{n_a - n_e}{n_e}. \quad (2.1.3.22)$$

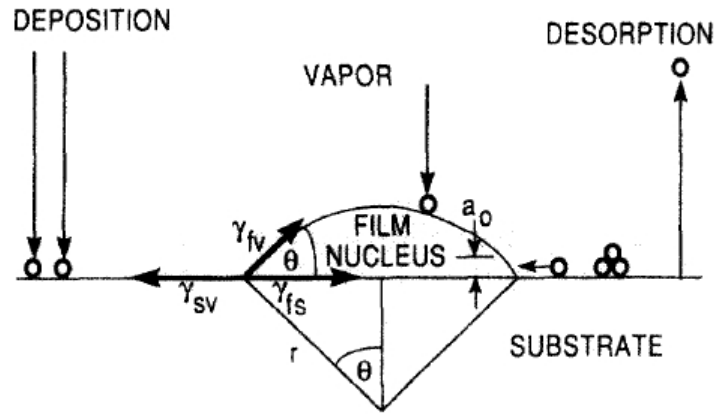


Fig 2.1.5 3D heterogeneous nucleation process, after Ref. [68].

The more complicated case of 3D heterogeneous nucleation is shown in Fig. 2.1.5, after Ref. [68]. Balancing horizontal tensions at the edge of a nucleus results in Young's equation

$$\gamma_{sv} = \gamma_{fs} + \gamma_{fv} \cos \theta, \quad (2.1.3.23)$$

or

$$\cos \theta = (\gamma_{sv} - \gamma_{fs}) / \gamma_{fv}. \quad (2.1.3.24)$$

This also has a connection to the different growth modes. If $\gamma_{sv} < \gamma_{fs} + \gamma_{fv}$, then $\theta > 0$ and the growth is 3D (the Volmer – Weber mode). If $\gamma_{sv} > \gamma_{fs} + \gamma_{fv}$, then $\theta = 0$ and the growth is 2D (Frank – Van der Merwe mode). If $\gamma_{sv} \approx \gamma_{fs} + \gamma_{fv}$, then $\theta \approx 0$ and the growth is pseudo 2D (Stranski – Krastanov mode).

The quantities of ΔG , r^c and ΔG^c associated with Fig. 2.1.5 are

$$\Delta G = a_3 r^3 \Delta G_V + a_1 r^2 \gamma_{fv} + a_2 r^2 \gamma_{fs} - a_2 r^2 \gamma_{sv}, \quad (2.1.3.25)$$

$$r^c = -\frac{2(a_1 \gamma_{fv} + a_2 \gamma_{fs} - a_2 \gamma_{sv})}{3a_3 \Delta G_V}, \quad (2.1.3.26)$$

and

$$\Delta G^c = \frac{4(a_1 \gamma_{fv} + a_2 \gamma_{fs} - a_2 \gamma_{sv})^3}{27a_3^2 (\Delta G_V)^2}, \quad (2.1.3.27)$$

with geometric factors $a_1 = 2\pi(1 - \cos\theta)$, $a_2 = \pi \sin^2 \theta$, and $a_3 = \pi/3(2 - 3\cos\theta + \cos^3 \theta)$.

From Young's equation it can be shown that $a_1 \gamma_{fv} + a_2 \gamma_{fs} - a_2 \gamma_{sv} = 3a_3 \gamma_{fv}$. Then the above equations can also be written as

$$r^c = -\frac{2\gamma_{fv}}{\Delta G_V}, \quad (2.1.3.28)$$

$$\Delta G^c = \frac{1}{3} \sum_n A_n \gamma_n = \frac{16\pi(\gamma_{fv})^3}{3(\Delta G_V)^2} \left(\frac{2 - 3\cos\theta + \cos^3 \theta}{4} \right). \quad (2.1.3.29)$$

Here ΔG^c is 1/3 of the total surface energy. It equals to the homogeneous nucleation barrier energy of Eq. (2.1.3.17) times a wetting factor $F(\theta)$, which is the term in braces. At $\theta = 0$, $F(\theta) = 0$, which means complete wetting with no nucleation barrier. At $\theta = 180^\circ$, $F(\theta) = 1$, which means no wetting. Here the heterogeneous nucleation barrier energy is the highest, and the only possibility is homogeneous nucleation. Values of θ between 0 and 180° represent situations where growth is intermediate between these two extremes.

Due to statistical energy fluctuations, nuclei of various sizes can be formed during the initial stage of nucleation. Those with radii larger than r^c are stable, since the nucleation barrier ΔG^c has been overcome. They will grow larger to further minimize free energy. On the other hand, nuclei formed with radii smaller than r^c are not stable, since in order to reduce ΔG they may shrink. Thus quasi-equilibrium will exist between stable critical nuclei

and monomers. We define the respective concentrations to be N^c and n_a , respectively. Then according to Eq. (2.1.1.9)

$$N^c = n_a \exp(-\Delta G^c / kT). \quad (2.1.3.30)$$

Here ΔG^c is assumed to be the same as that in the standard state. This equation is not to be confused with Eq. (2.1.3.21), which gives the supersaturation of a 2D ideal gas.

For heteroepitaxy exhibiting 3D growth, for example GaP on (001)Si, nucleation must be enhanced to develop a continuous film at the earliest stage. Thus r^c and ΔG^c need to be reduced, and N^c increased.

To increase N^c , the pre-exponential factor in Eq. (2.1.3.30), which is the monomer concentration n_a , needs to be increased. As suggested by the Langmuir isotherm of chemisorption, Eq. (2.1.3.2), this can be achieved by reducing the substrate T, or by increasing the adsorption rate, partial pressure, or equivalently, the supersaturation of precursors.

The absolute value of ΔG_v can be increased by increasing the degree of supersaturation S_{sat} , as suggested by Eq. (2.1.1.13). This increases the denominators of Eqs. (2.1.3.26) and (2.1.3.27), and hence reduces r^c and ΔG^c . An example on the Monte Carlo simulation of the change of nucleation behavior with increasing supersaturation is given in Fig. 2.1.6 after Ref. [77], which depicts the surface morphology at 20% surface coverage. Low supersaturation results in the growth of widely spaced large 3D islands as shown in (a), and increasing the supersaturation 1.85 times higher results in higher nucleation density and smaller nuclei sizes, as shown in (b).

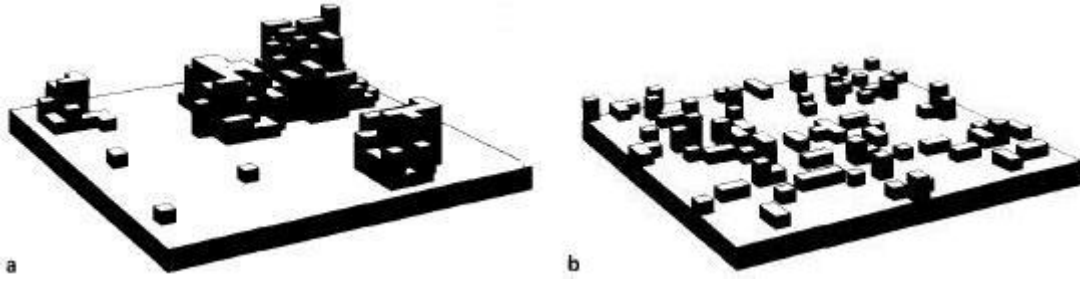


Fig 2.1.6 Monte Carlo simulation of surface morphology at 20% surface coverage under different supersaturations, after Ref. [77].

Other parameters can also be tuned. For example, the substrate surface energy γ_{sv} can be increased, and/or the film surface energy γ_{fv} and the film-substrate interfacial energy γ_{fs} decreased. This reduces the numerators of Eqs. (2.1.3.26) and (2.1.3.27), hence also r^c and ΔG^c . An example of reducing the film surface energy γ_{fv} is the use of reactive species also known as surfactants. These are found to increase nucleation density through enhanced wetting. Using the atomistic nucleation theory, Markov has calculated that surfactants can reduce the edge energy of 2D nuclei. This reduces the critical radius and the nucleation barrier energy, as shown in Fig. 2.1.7 after Ref. [81]. The numbers on each line represents the efficiency of surfactant $S = 1 - \omega/\omega_0$, with $\omega = (\psi_{cc} + \psi_{ss})/2 - \psi_{sc}$ and $\omega_0 = \psi_{cc}/2$. Here, ψ is the energy required to break a bond between two surfactant (crystal) atoms or a surfactant atom with a crystal atom.

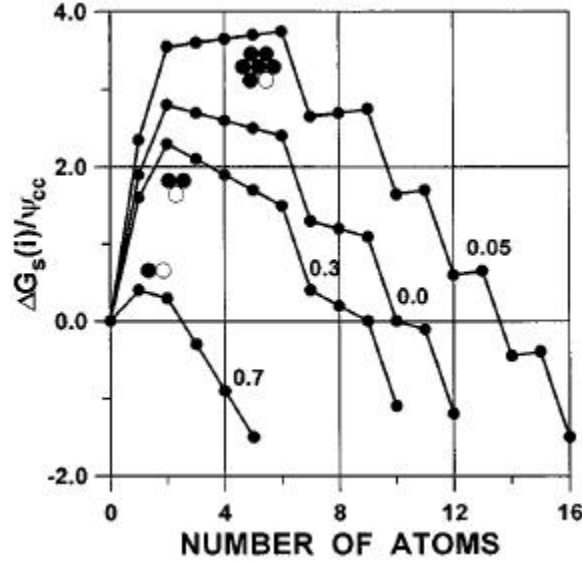


Fig 2.1.7 Effect of surfactants on the critical nucleus size and nucleation barrier energy, after Ref. [81].

We can identify optimum ranges of the growth parameter, the substrate temperature T and deposition rate \dot{R} , by requiring $(\partial r^c / \partial T)_R > 0$, $(\partial \Delta G^c / \partial T)_R > 0$, $(\partial r^c / \partial \dot{R})_T < 0$, and $(\partial \Delta G^c / \partial \dot{R})_T < 0$. Here \dot{R} is assumed to be proportional to the vapor pressure. Since r^c and ΔG^c both increase with T and decrease with \dot{R} , N^c will accordingly decrease with T and increase with \dot{R} . As a result, growth at low T and high \dot{R} is preferred to achieve smaller r^c and ΔG^c as well as larger N^c .

It is interesting to evaluate quantitatively the critical radius and energy barrier for nucleation. Assuming that the GaP nuclei have $\{111\}$ facets on (001) Si, then $\cos \theta = \sqrt{3}/3$, $\gamma_{fv} = 1.7 \text{ J/m}^2$ and $\gamma_{sv} = 2.53 \text{ J/m}^2$. From Young's equation (2.1.3.9), $\gamma_{fs} = 1.55 \text{ J/m}^2$. The atomic volume is $\Omega = (5.45 \times 10^{-10})^3 / 9 = 1.80 \times 10^{-29} \text{ m}^3$. The supersaturation under our current conditions is usually on the order of 100. Using these figures, we obtain the results such that $r^c = 1.1 \text{ nm}$ and $\Delta G^c = 6.2 \text{ eV}$. The supersaturation is large enough so that the resulting critical radius is only the size of a few atoms, and the

corresponding nucleation energy barrier is unrealistically high. This is because at the atomic scale the bonding effect of atoms cannot be ignored. Thus the macroscopic capillarity theory is not valid quantitatively here. This is in agreement with Refs. [68, 69].

2.1.3.3 Epitaxy

After the nuclei coalescence, a film develops with certain properties including surface morphology and crystalline structure. These are usually different from those of the substrate. Epitaxy is the subsequent growth of this film. Discussion of this topic can be found in Refs. [78, 80]. Some important points are summarized here.

Figure 2.1.8 presents the three different kinds of surfaces that can be exposed on a simple cubic lattice: the flat (F), stepped (S) and kinked (K) surfaces, which are defined to be parallel to either two, one, or zero atomically dense rows, respectively. Among all three the kink surface is the roughest and has the highest density of unsaturated bonds. Figure 2.1.9 further illustrated the five different positions that an atom can occupy on these surfaces. Table 2.2 summarizes their properties. Atoms attached at the kink sites have the same number of saturated and unsaturated bonds, and the surface energy will not change by either incorporation or detachment. Thus the kink sites are the thermodynamically preferred position for atoms to incorporate when supersaturation exists, and they determine the equilibrium between the crystal and the ambient.

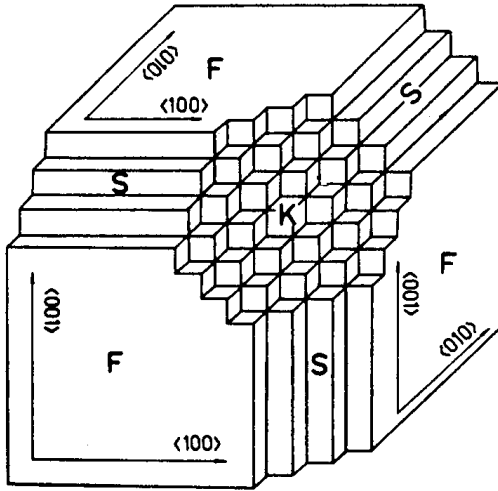


Fig 2.1.8 Schematic representation of flat (F), stepped (S), and kinked (K) surfaces of a simple cubic lattice, after Refs. [78, 80].

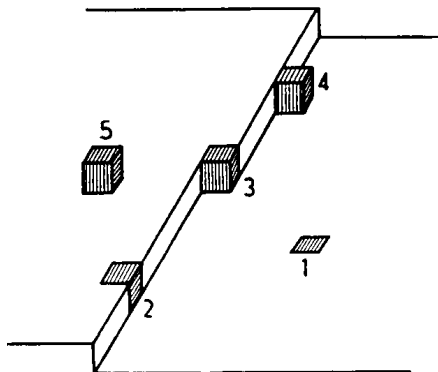


Fig 2.1.9 Different positions that an atom can occupy, after Refs. [78, 80].

Table 2.2 Number of saturated and unsaturated bonds for atoms in Fig 2.1.9, after Refs. [78, 80].

Number	Position	# of unsaturated bonds	# of saturated bonds
1	In surface	1	5
2	In step	2	4
3	At kink	3	3
4	At step	4	2
5	At surface	5	1

For epitaxy on an ideal defect-free flat surface, Young's equation (2.1.3.23) has described three different growth modes which are 2D or 3D nucleation mediated, and they can be treated using the nucleation theory of the above Section.

In reality epitaxy on non-ideal surface is typical. For epitaxy on a stepped surface, if 2D nucleation is favored, the adatom density is low, and the diffusion length is large, growth will follow the step flow mode which appears as the advance of steps. This is because the adatoms have stronger tendency to bond to the step edge than to form 2D nuclei. Similarly for epitaxy on a surface with lattice imperfections and impurities, if 3D nucleation is favored, the adatom density is low, and the diffusion length is large, then growth will occur only on those imperfections where the nucleation energy barrier is small.

For epitaxy on a rough surface exhibiting a high density of kinks, nucleation is not necessary. Continuous growth is achieved by atoms impinging on the surface being directly incorporated into kink sites. The growth rate is given by

$$R = a v \left(\frac{a}{\delta} \right)^2 \exp\left(-\frac{\Delta S_m}{k} \right) \exp\left(-\frac{\Delta U}{kT} \right) \left[1 - \exp\left(-\frac{\Delta G_a}{kT} \right) \right], \quad (2.1.3.31)$$

where a and δ are the distance between ordinary and kink sites, respectively, and $(a/\delta)^2$ is thus the geometric probability of finding a kink site. Also v is the adatom vibration

frequency, $\Delta S_m = \Delta h_m / T_m$ is the entropy of the phase transition under equilibrium at temperature T_m , ΔU is the energy barrier of adsorption, and ΔG_a is the free-energy change per atom. For small supersaturations $\Delta\mu \ll kT$, the Taylor expansion of the above gives $R \propto \Delta G_a$.

The other mode of epitaxy is spiral growth, which is initiated on the screw dislocations of a surface. Here, the growth rate is given by

$$R = C \frac{\sigma^2}{\sigma_c} \tanh\left(\frac{\sigma_c}{\sigma}\right), \quad (2.1.3.32)$$

where $\sigma = \frac{\Delta G_a}{kT}$, the characteristic supersaturation $\sigma_c = \frac{19\gamma_e a^2}{2n\lambda_s kT}$, and the rate constant

$C = a\nu \exp\left(-\frac{\varphi_{1/2}}{kT}\right)$. Here γ_e is the edge energy, n is number of screw dislocations, λ_s is the

surface diffusion length, and $\varphi_{1/2}$ is the energy to detach an atom from the kink site. For

small supersaturations $\frac{\sigma_c}{\sigma} \gg 1$, $\tanh\left(\frac{\sigma_c}{\sigma}\right) = 1$ and $R = C \frac{\sigma^2}{\sigma_c}$. This is the BCF parabolic

law. For large supersaturations $\frac{\sigma_c}{\sigma} \ll 1$, $\tanh\left(\frac{\sigma_c}{\sigma}\right) = \frac{\sigma_c}{\sigma}$ and $R = C\sigma$, which is the

BCF linear growth rate.

The equilibrium shape of a stable nucleus or a crystal is determined by the Wulff theorem

$$\gamma_n / h_n = \text{constant}, \quad (2.1.3.33)$$

where n represents different crystal facets. Here, h_n is the distance between the crystal facet n to the Wulff's point, which is usually the center of the crystal. The above is derived from the thermodynamics requirement of surface Gibbs free energy minimization for a crystal with constant volume and anisotropic surface energy γ . Also from a kinetics point of view, the

growth rate will be higher on facets with larger γ_n due to the stronger bonding of adatoms. Thus the area of these high-energy surfaces will be reduced in size as growth continues. When the surface energy is minimized, the exposed facets under equilibrium are usually those having the lowest surface energies.

2.2 Polarimetry

2.2.1 The polarimeter

A polarimeter is an optical instrument that combines the functions of a reflectometer and ellipsometer, measuring both the reflectance and complex reflectance ratio of a specular sample. These data are then analyzed for the properties of the sample, which are summarized in its dielectric response. We discuss these aspects here.

An ideal rotating-compensator polarimeter without misalignment or depolarization artifacts can be described by the Jones-matrix product

$$\begin{pmatrix} E'_x \\ E'_y \end{pmatrix} = \begin{pmatrix} 1 & 0 \\ 0 & 0 \end{pmatrix} \begin{pmatrix} \cos(C - A) & -\sin(C - A) \\ \sin(C - A) & \cos(C - A) \end{pmatrix} \begin{pmatrix} e^{i\delta_1} & 0 \\ 0 & e^{i\delta_2} \end{pmatrix} \begin{pmatrix} \cos C & \sin C \\ -\sin C & \cos C \end{pmatrix} \begin{pmatrix} r_p & 0 \\ 0 & r_s \end{pmatrix} \begin{pmatrix} \cos P & -\sin P \\ \sin P & \cos P \end{pmatrix} \begin{pmatrix} 1 & 0 \\ 0 & 0 \end{pmatrix} \begin{pmatrix} E_x \\ E_y \end{pmatrix} \quad (2.2.1.1)$$

where P , C , and A are the azimuth angles of the polarizer, compensator, and analyzer, respectively, relative to the sample normal, r_p and r_s are the p- and s- polarized complex reflectances of the sample, and $\delta_1 = d \frac{\omega}{c} n_1$, and $\delta_2 = d \frac{\omega}{c} n_2$ are the phase shifts associated with the two principal axes of the compensator. The effects of the polarizer, sample, compensator, and analyzer are described in matrix forms. The rotation matrices are used to change field projections between local and laboratory frames.

The intensity that arrives at the photodiode array detector (PDA) has the form

$$I = |E'_x|^2 = I_0 \{1 + \alpha_2 \cos 2C + \beta_2 \sin 2C + \alpha_4 \cos 4C + \beta_4 \sin 4C\}. \quad (2.2.1.2)$$

The coefficients α_2 , β_2 , α_4 , and β_4 are obtained by rotating the compensator according to $C = \omega t$. This results in a frequency modulation, from which the coefficients can be determined by Fourier analysis. In terms of reflectances I_0 and the coefficients in Eq. (2.2.1.2) can be written as

$$I_0 = \frac{|E_x|^2}{4} \left\{ 2(1 + \cos \delta) \left[|R_p|^2 \cos^2 A + |R_s|^2 \sin^2 A + \operatorname{Re}(R_p R_s^*) \sin 2A \right] + (1 - \cos \delta) \left[|R_p|^2 + |R_s|^2 \right] \right\}; \quad (2.2.1.3)$$

$$\alpha_2 = \frac{|E_x|^2}{I_0} \sin \delta \sin 2A \operatorname{Im}(R_p R_s^*); \quad (2.2.1.4)$$

$$\beta_2 = -\frac{|E_x|^2}{I_0} \sin \delta \cos 2A \operatorname{Im}(R_p R_s^*); \quad (2.2.1.5)$$

$$\alpha_4 = \frac{|E_x|^2}{I_0} (1 - \cos \delta) \left\{ \left(|R_p|^2 - |R_s|^2 \right) \cos 2A + 2 \operatorname{Re}(R_p R_s^*) \sin 2A \right\}; \quad (2.2.1.6)$$

$$\beta_4 = \frac{|E_x|^2}{I_0} (1 - \cos \delta) \left\{ \left(|R_p|^2 - |R_s|^2 \right) \sin 2A - 2 \operatorname{Re}(R_p R_s^*) \cos 2A \right\}; \quad (2.2.1.7)$$

where $\delta = \delta_2 - \delta_1$, $R_p = r_p \sin P$, and $R_s = r_s \sin P$.

The dc component of the intensity I_0 provides reflectance data. The 2ω and 4ω Fourier coefficients α_2 , β_2 , α_4 , and β_4 are normalized with respect to the dc component, and are used to extract the sample dielectric function through least-squares fitting.

In real situations many factors contribute to the intensity signal. Table 2.3 shows the information content carried by the lowest 10 Fourier coefficients of this rotating-compensator polarimeter, including the degree of polarization. The 0, 2, and $4\omega t$ terms carry the sample information. The 1, 3, and $5\omega t$ terms are used for compensator alignment. The $8\omega t$ term describes system nonlinearity. The 6, 7, and $9\omega t$ terms show the background noise level. The $10\omega t$ term is the reflectance difference spectroscopy (RDS) measurement. The degree

of polarization (DOP) provides information about crosstalk and component leakage.

Table 2.3 Information content in the harmonic of a rotating-compensator polarimeter with a monoplate compensator.

Term	0 ωt (dc)	1 ωt	2 ωt	3 ωt	4 ωt	5 ωt
Information	Sample	Alignment	Sample	Alignment	Sample	Alignment

Table 2.3 (continued)

Term	6 ωt	7 ωt	8 ωt	9 ωt	10 ωt	DOP
Information	Background noise level	Background noise level	System nonlinearity	Background noise level	RDS	Crosstalk, component leakage

2.2.2 Two, three and four phase models

Our objective is to obtain information about the sample from the measured reflectance and complex reflectance ratio. The procedure to be used depends on the sample.

In the simplest case of an isotropic material with no overlayers, we use the two-phase model. This consists of an ambient and a substrate, as shown in Fig 2.2.1 (a). The properties of the sample are described entirely by its dielectric function ϵ , which is related to the complex reflectances according to

$$r_{sa}^p = \frac{\epsilon_s n_{a\perp} - \epsilon_a n_{s\perp}}{\epsilon_s n_{a\perp} + \epsilon_a n_{s\perp}}; \quad (2.2.2.1)$$

$$r_{sa}^s = \frac{n_{a\perp} - n_{s\perp}}{n_{a\perp} + n_{s\perp}}; \quad (2.2.2.2)$$

where $n_{j\perp} = \sqrt{\epsilon_j - \epsilon_a \sin^2 \theta}$, and j represents either s or a, and θ is the angle of incidence.

The dielectric function can be calculated from ρ according to

$$\frac{\epsilon_s}{\epsilon_a} = \sin^2 \theta \left(1 + \tan^2 \theta \left(\frac{1-\rho}{1+\rho} \right)^2 \right). \quad (2.2.2.3)$$

The more general case of a substrate with an overlayer requires the three phase model, which is shown in Figure 2.2.3 (b). The overlayer is described by a thickness d and dielectric function ϵ_o . Now the complex reflectances are given by

$$r_{soa}^{p,s} = \frac{r_{oa}^{p,s} + Z r_{so}^{p,s}}{1 + Z r_{so}^{p,s} r_{oa}^{p,s}}, \quad (2.2.2.4)$$

where $Z = \exp\left(i \frac{4\pi}{\lambda} n_{o\perp} d\right)$. r_{soa}^p and r_{soa}^s cannot be solved analytically in general for ϵ_o and d , even if all the other quantities are known. Numerical analysis is required. An exception occurs when $d/\lambda \ll 1$, in which case we have the simple analytic form

$$\langle \epsilon \rangle = \epsilon_s + \frac{4\pi i d n_a}{\lambda} \frac{\epsilon_s (\epsilon_s - \epsilon_o) (\epsilon_o - \epsilon_a)}{\epsilon_o (\epsilon_s - \epsilon_a)} \left(\frac{\epsilon_s}{\epsilon_o} - \sin^2 \theta \right)^{1/2}. \quad (2.2.2.5)$$

where $\langle \epsilon \rangle$ is the pseudodielectric function. $\langle \epsilon \rangle$ is the quantity calculated from ϵ in the two-phase model, Eq. (2.2.2.3) ignoring the presence of the overlayer. For $|\epsilon_s| \gg |\epsilon_o| \gg \epsilon_a = 1$, Eq. (2.2.2.5) can be simplified further to yield

$$\langle \epsilon \rangle = \epsilon_s + \frac{4\pi i d}{\lambda} \epsilon_s^{3/2}. \quad (2.2.2.6)$$

The complete absence of ϵ_o in eq. (2.2.3.5) means that under these limiting conditions the material can be studied without having to identify the overlayer.

Further generalization leads to the four-phase model, which has the configuration substrate / bulk overlayer / top overlayer / ambient, as shown in Fig 2.2.1 (c). It differs from the three-phase model by splitting the overlayer into separate bulk and top layers. The four-phase model is required when dealing with films having rough surfaces. It also ensures a better representation of $\langle \epsilon \rangle$. The overlayer part summarizes the average dielectric

response of the underneath the rough surface, which is only accessible by light with large penetration depths. Thus it primarily contributes to the low-adsorption region of $\langle \epsilon \rangle$. If the film is thick enough, this region of the spectrum will also exhibit interference oscillations. In contrast, the top overlayer describing the outermost region may be opaque at sufficiently short wavelengths, again depending on its thickness. Consequently, it affects most strongly the higher energy part of $\langle \epsilon \rangle$.

Since after growth the deposited film is usually terminated with a rough surface, the question remains as to how to represent its dielectric response. The effective dielectric function of the top layer is usually approximated using a Bruggeman EMA with 50% voids, as discussed below. The thickness of the rough layer is obtained by least-squares fitting.

The above procedure allows for a universal comparison between different results, but it does suffer from several drawbacks. First, data about the rough-surface layer obtained by fitting a pseudodielectric function yields only average information over a relatively large area. This may not accurately represent the real surface. Second, unless the spot size is restricted, SE cannot provide information about lateral correlations. In fact, as will be seen in Ch. 4, SE cannot detect grains on surfaces where the sizes and shapes of the grains are larger than the wavelengths of light. Third, the four-phase model defines a rough-surface layer that is optically distinct from the bulk. This approximation works well if there actually is a sharp boundary between the rough surface and the next layer down. In this case the discrepancy between AFM and SE data is the smallest. However, if the bulk of the film also has a high fraction of voids, then the boundary between the bulk and rough-surface layer will not be so well defined, and the four-phase-model will not necessarily be a good approximation.

Thus AFM must be used together with SE to provide the best description for surface roughness. Nevertheless, the ellipsometrically determined thickness of the rough-surface layer is an indispensable supplement to the AFM RMS roughness data, since it provides information about possible porous structures lying underneath the top surface, which

obviously cannot be accessed by AFM.

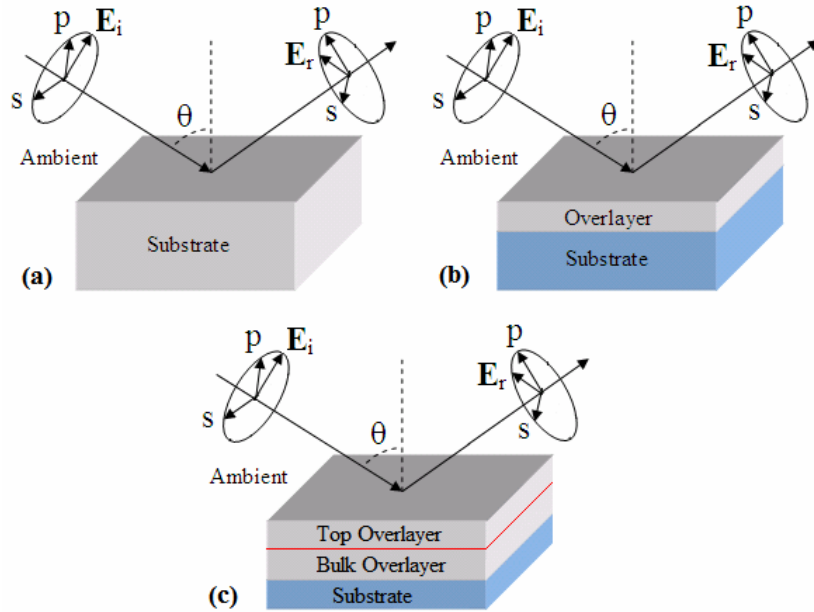


Fig 2.2.1 (a) Two phase model, (b) Three phase model, and (c) Four phase model.

2.2.3 Dielectric function and the Bruggeman effective medium approximation

The dielectric functions ϵ that are returned by analyzing the complex reflectances in the two-, three-, and four- phase models provide an average description of the microscopic response of the associated materials to applied electromagnetic field. This response is usually in the form of induced dipoles.

To get some feeling for the origin of ϵ , we start from the specific microscopic Maxwell's Equation of interest,

$$\nabla \cdot \mathbf{E} = 4\pi\rho. \quad (2.2.3.1)$$

An average over the volume V together with some mathematic yields

$$\nabla \cdot \langle \mathbf{E}(\mathbf{r}) \rangle = 4\pi \langle \rho(\mathbf{r}) \rangle = 4\pi \langle \rho_0(\mathbf{r}) \rangle - 4\pi \nabla \cdot \langle \mathbf{P}(\mathbf{r}) \rangle \quad (2.2.3.2)$$

where ρ_0 is the unperturbed charge density and $\langle \mathbf{P}(\mathbf{r}) \rangle$ the dipole density per unit volume. We combine the two divergences by defining a displacement field \mathbf{D} as

$$\mathbf{D}(\mathbf{r}) = \langle \mathbf{E}(\mathbf{r}) \rangle + 4\pi \langle \mathbf{P}(\mathbf{r}) \rangle = \varepsilon \langle \mathbf{E}(\mathbf{r}) \rangle, \quad (2.2.3.3)$$

where in linear optics ε relates \mathbf{D} to the average applied field $\langle \mathbf{E}(\mathbf{r}) \rangle$. We have assumed that the medium is isotropic and that the response of \mathbf{P} to \mathbf{E} is linear. Generalization to anisotropic media is straightforward.

Often in OMCVD the grown film is a mixture of two or more materials, e.g., GaP and voids. If we assume that the inhomogeneous regions are smaller than 10% of the wavelength of light but still large enough to have their own dielectric identity, and that they are distributed randomly, ε of this mixture can be represented by the Bruggeman effective medium approximation (EMA) [82]

$$0 = f_a \frac{\varepsilon_a - \varepsilon}{\varepsilon_a + 2\varepsilon} + f_b \frac{\varepsilon_b - \varepsilon}{\varepsilon_b + 2\varepsilon}, \quad (2.2.3.4)$$

where ε_a and ε_b are the dielectric functions of materials a and b, and f_a and f_b their volume fractions. Two limiting cases exist if the intermixing is laminar [82]. If all boundaries are parallel to the applied field, the screening vanishes and

$$\varepsilon = f_a \varepsilon_a + f_b \varepsilon_b. \quad (2.2.3.5)$$

If all boundaries are perpendicular to the field, the screening is maximized and

$$\varepsilon^{-1} = f_a \varepsilon_a^{-1} + f_b \varepsilon_b^{-1}. \quad (2.2.3.6)$$

The most common applications of Eq. (2.2.3.4) are to analyze deposited films for their void fractions, if any, and to model the dielectric response of a rough surface. In the latter case the rough surface is usually considered to consist of 50% of the underlying material and 50% voids, as noted in Sec. 2.2.2.

2.2.4 Spectral analysis near critical points

One of the primary features of ϵ is that its wavelength dependencies is a function of the material and can be used to identify the presence of this material in the real-time data. The connection to material properties is made through the electronic band structure. Figure 2.2.2 is the electronic band structure of Si calculated by the $\mathbf{k}\cdot\mathbf{p}$ method, with the main interband critical points labeled conventionally as E_0 , E_1 , and E_2 [83]. These refer to the features associated with transitions along the Γ , Λ , and X directions respectively, where the conduction and valance bands are parallel.

Dielectric function spectra near critical points can be represented by the standard analytic expressions [83]:

$$\epsilon(\omega) = C - Ae^{i\Phi}(\omega - E_g + i\Gamma)^n \quad (2.2.4.1)$$

The structure is described by four parameters: the amplitude A , threshold energy E_g , broadening parameter Γ , and phase angle Φ . The exponent n is the dimension of the critical point, and is $-1/2$ for 1D, 0 for 2D, and $1/2$ for 3D transitions, respectively.

Critical-point energies are usually determined by assuming a model line shape then obtaining its parameters through least-squares analysis. Second-energy derivatives of the spectra are often used for this purpose. The generic form is [83]

$$\frac{d^2\epsilon}{d^2\omega} = \begin{cases} n(n-1)Ae^{i\Phi}(\omega - E + i\Gamma)^{n-2}, & n \neq 0 \\ Ae^{i\Phi}(\omega - E + i\Gamma)^{-2}, & n = 0 \end{cases} \quad (2.2.4.2)$$

An analysis of the E_1 critical point (2D, $n = 0$) for room-temperature Si is given in Fig 2.2.3, as an example. The resultant critical point energy of the $E_1 = 3.361 \pm 0.006$ eV. We shall use this approach to calibrate sample temperatures in the OMCVD reactor.

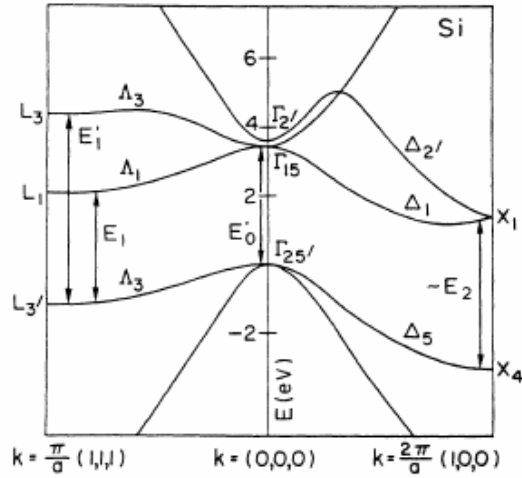


Fig 2.2.2 Electronic band structure of Si, after Ref. [83].

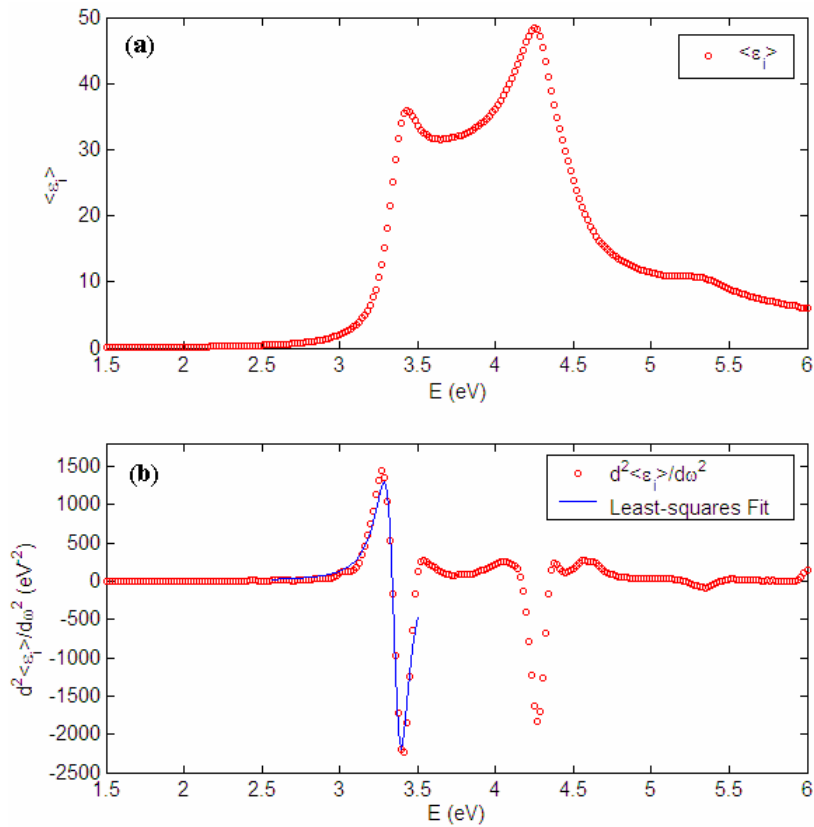


Fig 2.2.3 (a) Imaginary part of the dielectric function $\langle \epsilon_i \rangle$ of the room temperature Si; (b) Second energy derivative of $\langle \epsilon_i \rangle$ along with the least-squares fit of Eq. (2.2.2.2).

Alternatively, spectra can be analyzed by Fourier-transforming them into reciprocal space [84]. This avoids the need for differentiation, and results in improved elimination of noise and better separation of critical-point parameters. Specifically, the critical point energy can be readily extracted from the phase-coherent condition, independent of the other parameters. However, disadvantages occur for spectra with broad structures, e.g., spectra at high temperatures. Here, there are too few Fourier coefficients to work with, and the phase coherence is difficult to evaluate. Examples of using this method can be found in Ref. [84].

Chapter 3 Experiment

This chapter describes our experimental configuration and procedures. Section 3.1 provides an overview of the instrument, specifically a modified commercial OMCVD reactor with an integrated spectroscopic polarimeter. Section 3.2 lists various materials that are used for the experiment, including carrier gases, organometallic and hydride reactive species, and epitaxial substrates. The operation of the burst growth mode is also covered. Section 3.3 introduces briefly the polarimeter calibration steps. Section 3.4 discusses calibration of sample temperature, which relates the thermocouple reading to the actual temperature of the sample surface. Section 3.5 describes the thickness-profile measurement. Section 3.6 introduces the various methods to generate nrSi for use in GaP heteroepitaxy.

3.1 Instrument Overview

Figure 3.1.1 gives a schematic view of our integrated OMCVD/polarimeter system. The rotating-compensator polarimeter operates at an angle of incidence of 70.2° and acquires relative-intensity (RI) and pseudodielectric function $\langle \epsilon \rangle$ spectra at wavelengths λ from 230 to 840 nm at a 4 Hz rate, allowing real-time diagnostics on this time scale. The OMCVD reactor is a modified EMCORE GS3300 model with a vertical flow, shower head, cold wall, and rotating-disk design. Precursors with carrier gas are injected into the chamber through different inlets of the shower head, first reaching a compartment whose lower bound is a fine stainless steel mesh. Various species intermix within the compartment and are then transported away through the mesh in a pattern that is nominally homogeneous horizontally. Samples are usually rotated at 1200 rpm by a Baldor motor, which is synchronized at a 5:1 ratio to the rotation of the compensator to separate the anisotropic response from the $2\omega t$ and

4 ω t harmonics that carry sample information through $\langle \varepsilon \rangle$. Nominally, the flow over the sample surface is laminar due to the pulling action exerted on the ambient gas by rotation, but as we show later basically the same results were obtained when samples were held stationary. The shower head, optical ports, and reactor walls are constantly cooled by running water to prevent the temperature from increasing, and therefore damaging the various vacuum seals.

Figure 3.1.2 is a cross view of our spindle assembly, which features a capability to adjust sample wobble while the spindle is rotating [85]. The two bottom micrometer screws adjust the sample tilt in two orthogonal directions through a mechanical linkage. The top of the spindle shaft is a molybdenum arbor, on which the Mo susceptor is mounted by a stainless steel screw. The sample holder sits on the susceptor, located by three pins and holes. Runout is measured using a He-Ne laser beam that enters nearly in parallel to the Xe lamp beam but with a larger angle of incidence. Wobble is minimized by adjusting the spindle to minimize travel of the laser spot that is projected on a monitoring screen after the beam is reflected from the sample.

To reduce vibration, we replaced the original solid susceptor with a light-weight, wheel-like version with spokes and an outer rim. This also enabled the graphite heater to function more efficiently since the sample holder is heated directly rather than indirectly through the susceptor, as will be shown in Sec. 3.4.

At temperatures above 700 °C sample runout is significantly more difficult to control, probably due to an overall loosening of the structure because of the different thermal expansions of the molybdenum susceptor and the stainless steel screw, and also the molybdenum sample holder and the sample. To obtain a better signal-to-noise ratio, we occasionally rotated the spindle in a local mode independent of the compensator. This allows us to operate at a rotation speed that minimizes residual vibration. The above procedure did not cause any obvious changes in the results.

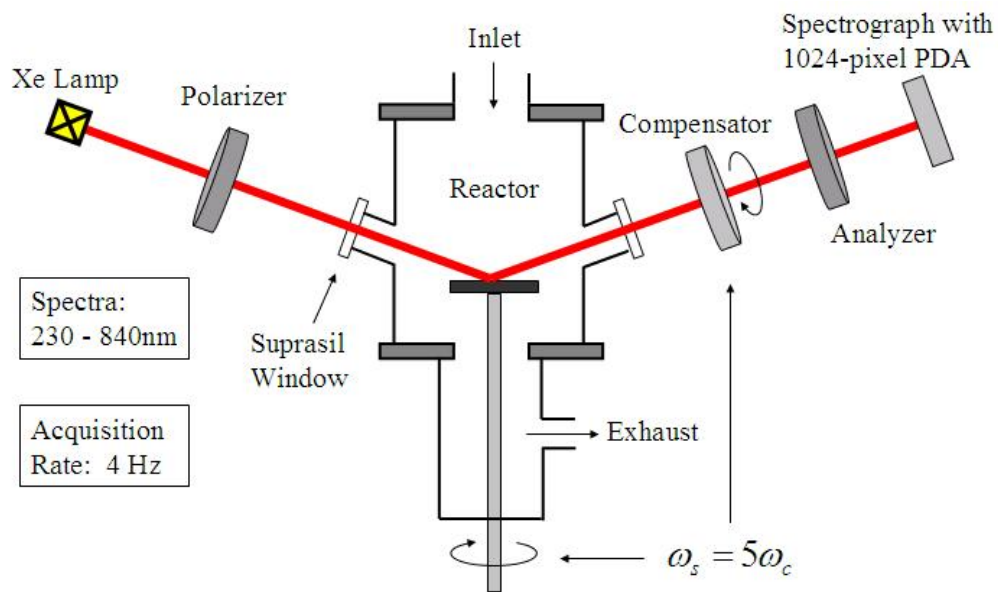


Fig 3.1.1 Integrated OMCVD/polarimeter system.

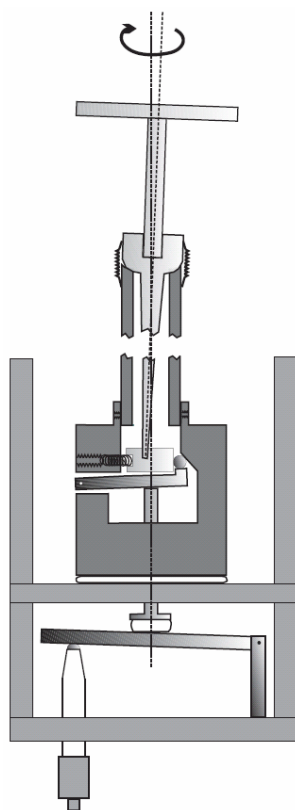


Fig 3.1.2 Spindle assembly with real-time wobble adjustment [85].

3.2 Materials

The carrier gases are ultrahigh purity (99.9996% minimum) N₂, generated as boiloff from a liquid N₂ dewar, and H₂. Both were obtained from National Welders. N₂ is also used for baking out the system and purging the mechanical pump.

The hydride group-V precursor used in the experiment is ultra-high purity (99.9996% minimum) Phosphine (PH₃) obtained from Matheson Tri-Gas. The flow rate is set by a mass flow controller.

Organometallic group III precursors used are Trimethylgallium (TMG, melting point -15.8 °C) and Trimethylaluminium (TMAI, melting point 15.4 °C), obtained from Rohm and Haas. These are stored in bubblers as 3-phase mixtures at temperatures of -16 °C and 16 °C respectively. The organometallic vapor pressures as a function of temperature can be expressed as [67]:

$$\log(P[\text{Torr}]) = a - b/T[\text{K}] \quad (3.2.1)$$

Vapor pressures at the storage temperatures we use are calculated to be 28.02 Torr for TMG with $a = 1703$, $b = 8.07$, and 6.92 Torr for TMAI with $a = 2135$, $b = 8.224$.

Figure 3.2.1 is a schematic drawing of an organometallic bubbler [86]. The mass flow controller meters the input carrier gas, and the pressure controller regulates the pressure inside the bubbler. The net flow rate of the organometallic precursor F_{OM} that goes into the reactor is calculated as [87]:

$$F_{OM} = F_C P_V / (P_{PC} - P_V) \quad (3.2.2)$$

where F_C is the flow rate of the carrier gas, P_V is the vapor pressure of the organometallic precursor, and P_{PC} is the total pressure inside the bubbler set by the pressure controller.

Equation (3.2.2) assumes that the partial-pressure ratio is the same as the flow-rate ratio, and is only meaningful under steady flow conditions. If P_{PC} is reset to a higher value, then no flow will occur until the pressure inside the bubbler reaches the reset value. The delay

obviously depends on the flow rate as well as the pressure change. On the other hand if P_{PC} is set to a lower value by 100 Torr or more, the output side is fully opened, and a substantial fraction of the gas mixture in the bubbler is rapidly dumped into the reactor over a period of several seconds. The growth rate may then momentarily exceed the steady-state rate by an order of magnitude. We use this mode occasionally and term it the burst mode of growth.

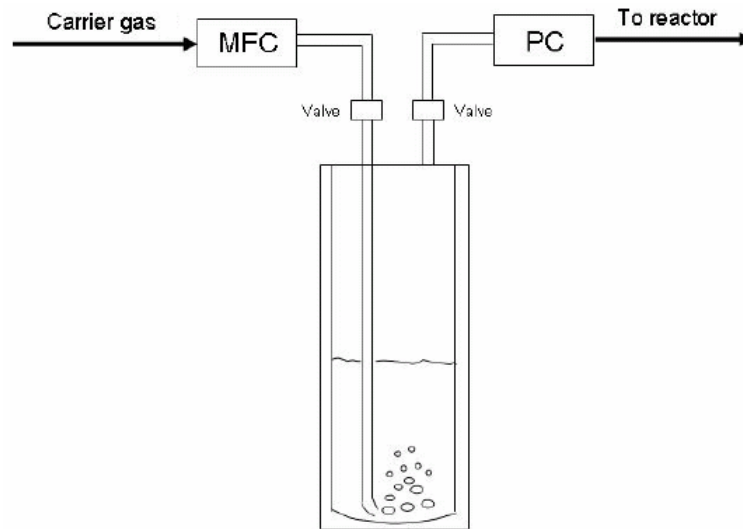


Fig 3.2.1 Schematic drawing of an organometallic bubbler [86].

Various 2" Si and GaAs epi-ready substrates were used for GaP heteroepitaxy, as shown in Table 3.1.

Table 3.1 Various 2" epi-ready wafers

Material	Orientation	Doping	Supplier
GaAs	(001) $\pm 0.1^\circ$	N	American Xtal Technology
Si	(001) $4^\circ \pm 0.5^\circ$ toward $\langle 110 \rangle$	N	Umicore
Si	(001) $\pm 0.1^\circ$	P	Virginia Semiconductor

3.3 Polarimeter Calibration

The polarimeter must be calibrated before any data are acquired. In practice we follow a detailed procedure developed previously [88], which includes 5 sequential steps: (1) determination of the zero reference azimuth of the polarizer; (2) determination of the PDA acquisition delay; (3) determination of the analyzer zero azimuth; (4) wavelength calibration of the diodes; and (5) correction for higher-order effects.

As the first optical element, the polarizer establishes the polarization state of the beam emitted from the Xe arc lamp. At $P = 0$, the 2ω Fourier coefficients are identically zero, and the 4ω coefficients satisfy $\beta_4/\alpha_4 = \tan(2A)$, so ideally $\arctan(\beta_4/\alpha_4)$ is a horizontal line across the entire 1024-diode range. But since there is a $5 \mu\text{s}$ reading delay between adjacent diodes, the Fourier coefficients are actually measured at different compensator azimuths. When this delay is taken into account the relation is

$$\tan^{-1}(\beta_4/\alpha_4) = 2A + \Delta\Phi_c, \quad (3.3)$$

where for a 5 Hz rotation rate $\Delta\Phi_c = 4\omega_c\Delta t = 4 \times 2\pi \times 5 \text{ (Hz)} \times 5 \times 10^{-6} \text{ (s)} = 6.28 \times 10^{-4}$. The zero azimuth of the polarizer is thus found by adjusting P to obtain the best fit of the measured $\arctan(\beta_4/\alpha_4)$ vs. diode number to a straight line with slope 6.28×10^{-4} . The PDA acquisition delay is also obtained in the fitting procedure.

Once the polarizer is calibrated, P is set to 90° and the zero azimuth reference of the analyzer is determined next. The compensator is removed for this step. At $P = 90^\circ$, the beam reflected from the sample is s-polarized. However, at $A = 0$, only p-polarized light can pass through. Thus the analyzer zero azimuth is found by adjusting A to the value that gives the least detected intensity.

The wavelength calibration of the diodes is done by using the RI data recorded from a Hg/Ar lamp, as shown in Fig. 3.3.1 [89]. Various peaks are identified, with wavelengths that can be found in literature [90]. In our system the wavelengths are equally spaced from

diode to diode, and a linear fit yields the two calibration parameters.

With the polarimeter operating over the entire spectral range of 230 to 840 nm, the lower energy pixels can also detect second and/or third order light diffracted from higher-energy pixels. To correct for this we use a series of CVI optical narrow band pass filters at wavelengths of 239 nm, 253 nm, 300 nm and 360 nm to determine the relations of the higher-order intensities with respect to the first order. The higher-order effects are then subtracted from the final spectrum.

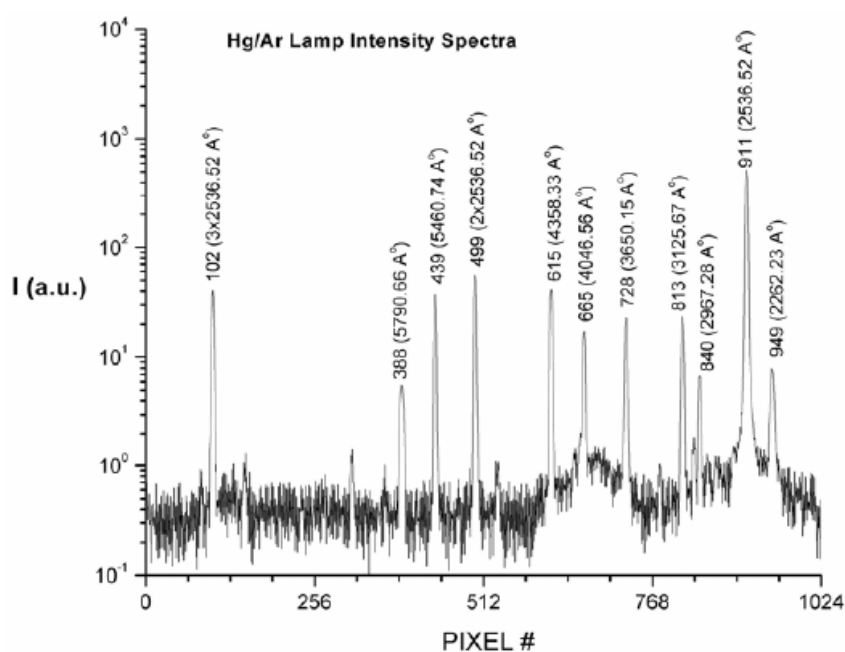


Fig 3.3.1 Relative intensity spectrum of a Hg/Ar lamp [89].

3.4 Temperature Calibration

The OMCVD growth temperature is a crucial parameter that needs to be accurately determined. In our system the temperature of the sample in the growth chamber is measured approximately by a thermocouple placed 1 cm under the graphite heater, and the

mV signal is returned to a Eurotherm display that converts the voltage to degrees Celsius. The sample is actually heated by contact through the sample holder, which rests on the susceptor 2 cm above the heater. With so many intervening elements and flowing carrier gas, the thermocouple reading is obviously not the real sample temperature. For example, during experiments we have observed that our solid molybdenum susceptor operates at a higher color temperature than the molybdenum sample holder, which means that the susceptor impedes heat flow to the sample. To improve efficiency, we replaced the original susceptor with a lightweight, wheel-like version with only spokes and an outer rim. This allows the susceptor to be heated directly.

Temperature calibration is done using the temperature dependence of the energy of the E_1 transition of Si, which is available in the literature [83]. A (001) Si wafer is treated with HF, and then loaded into the chamber. We then flow H_2 at 10 SLM to simulate actual growth conditions. The heater power supply voltage is increased in steps and after the Eurotherm reading has stabilized, a spectrum averaged over 10 seconds is recorded. The spectrum is then analyzed by the methods described in Chapter 2 to extract the E_1 transition energy at those temperature readings, which calibrates the thermocouple.

In Figure 3.4.1 we show in red the measured Si E_1 transition energies at various thermocouple readings for the system with the original susceptor. Plotted in blue are the real Si temperatures at those E_1 transition energies from reference [83]. The corresponding real temperatures vs. thermocouple readings are plotted in Figure 3.4.2. The difference is significant, as expected, especially at higher temperatures. For example the actual temperature is about 650 °C when the reading is 800 °C.

Figure 3.4.3 is the equivalent of Figure 3.4.1 for the new susceptor, and Figure 3.4.4 shows the new calibration. The sample temperature now tracks the thermocouple reading much more closely. This is beneficial because we can now achieve the same sample temperature with much lower power input, reducing the thermal load on the chamber.

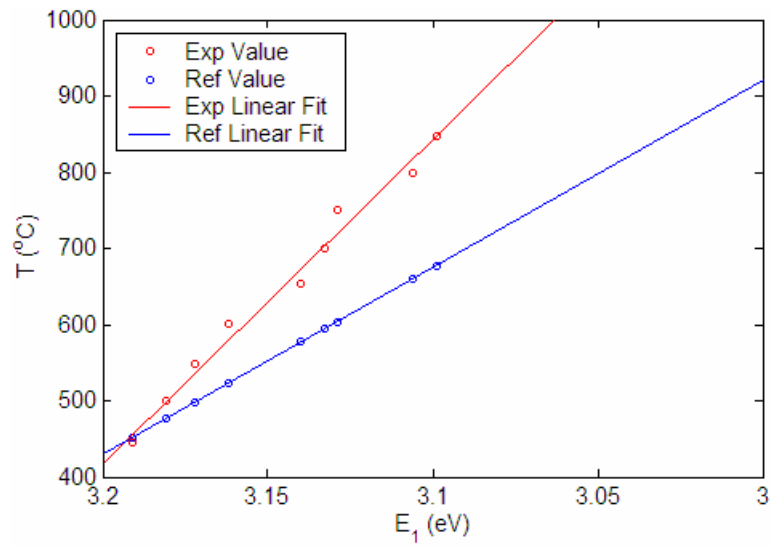


Fig 3.4.1 Thermocouple readings vs. measured Si E₁ transition energies for the original susceptor (red), along with the T dependence of the Si E₁ transition energy from Ref. [83].

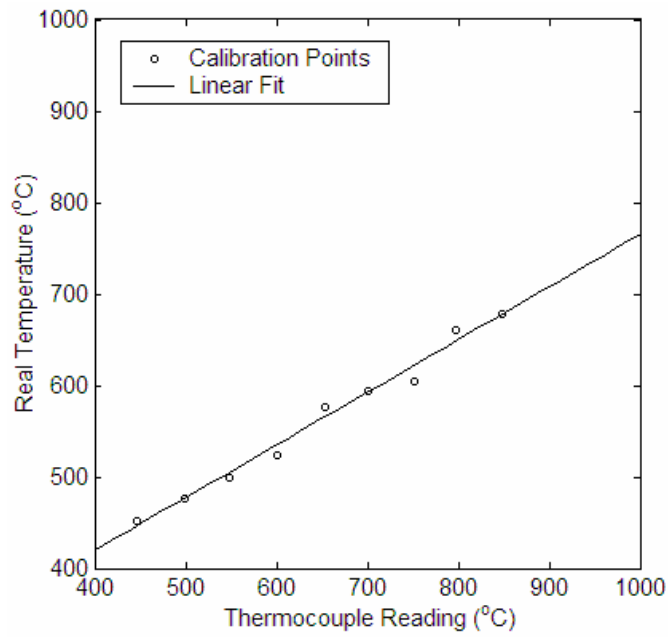


Fig 3.4.2 Temperature calibration curve for the original susceptor.

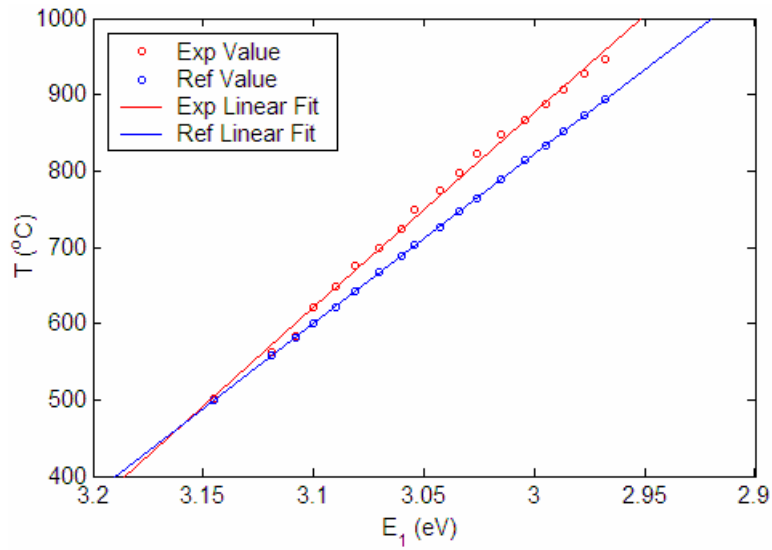


Fig 3.4.3 As Fig 3.4.1, but with the new susceptor.

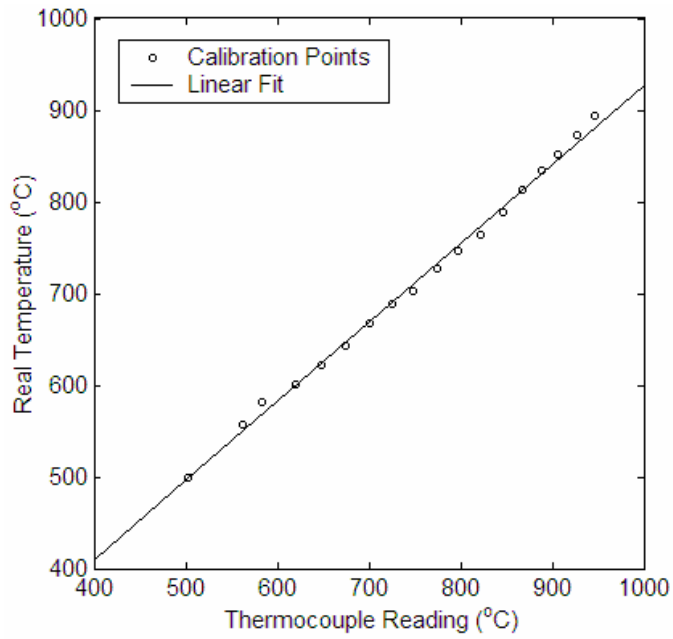


Fig 3.4.4 As Fig 3.4.2, but for the new susceptor.

3.5 Thickness-profile measurements

Figure 3.5 (a) illustrates the ellipsometer beam positions across an arbitrary 1” wafer radius, where 20 bench SE spectra are taken at evenly spaced intervals of $25.4/20 = 1.27$ mm. Figure 3.5 (b) illustrates the beam path in the entrance arm. The ellipsometer beam size is defined by a 1 mm diameter aperture placed 2 cm before the sample, perpendicular to the direction of incidence at 67.08° . Thus the beam spot hitting the surface is approximately elliptical with an area about $\pi \cdot (0.5)^2 / \cos(67.08^\circ) \approx 2 \text{ mm}^2$. The 1 mm minor axis is aligned with the radius of interest, so two adjacent measurements do not overlap with each other, since the distance between beam centers is larger than the minor axis length of the beam spot. An average thickness representing the area under beam illumination can be extracted by performing four-phase-model least-squares fittings to the local $\langle \epsilon \rangle$ spectrum, and results expressed as a nominal thickness (T_N) = bulk thickness + top thickness, or as an effective thickness (T_E) = bulk thickness \times bulk concentration + top thickness \times top concentration.

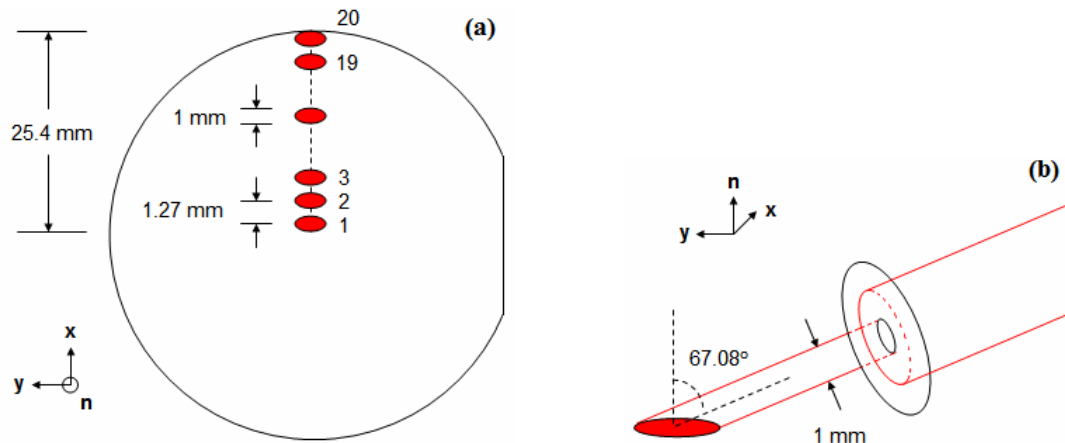


Fig 3.5.1 (a) Ellipsometer beam measurement positions across an arbitrary 1” wafer radius; (b) Ellipsometer beam path in the entrance arm. The scale is for illustration purpose only.

3.6 Formation of nrSi

One of the methods that we investigated to increase initial nucleation density was to roughen Si on a nanoscopic scale. Here, we describe various produces that can be used, including all those that were used.

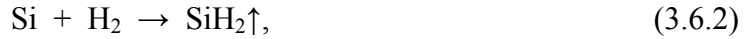
3.6.1 Si reaction with H₂

Both bare Si and Si with a thin SiO₂ layer can be roughened by reaction with H₂. Residual O₂ and H₂O in the H₂ may also contribute to the roughening process.

Gallois *et al.* [91] studied the etching of (001) Si with H₂ at temperatures from 1052 to 1277 °C. Nomarski interference microscopy and SEM showed the surfaces to be roughened considerably, exhibiting square pits having four (111) sides and a (001) bottom. The activation energy was calculated to be 314 ± 42 kJ/mol (or 3.25 ± 0.43 eV) from the etching rate determined by mass and thickness changes in the temperature range of 1052 – 1277 °C, which is about 10 nm/min at 1052 °C. The etching products are mainly SiH₄ and SiH₂, as determined from their thermodynamic calculations.

Habuka *et al.* [92] have studied the effect of H₂ on (001) Si covered with 1.4 nm native oxide layers at 800 – 1100 °C under atmospheric pressure. Their AFM data show the formation of square and triangular shaped pits on (001) and (111) surfaces, respectively. The pit size increases after longer heating, but the root-mean-square (RMS) roughness saturates at about 6 nm after 10 minutes at 900 °C. They attribute the pit formation and surface roughening to the faster etching of H₂ for Si than for SiO₂ at these temperatures, which they establish by step-height and ellipsometry measurements, respectively. Their etching rate of H₂ is smaller than Ref. [91], but is still on the order of nm/min. The proposed reactions are





All generated species are volatile at these temperatures.

Yanase *et al.* [93] have observed a similar effect in that the (001) Si surface is considerably roughened under H₂ annealing at 900 – 1100 °C. However, they attribute the etching to the presence of oxygen and moisture of the level of ppm in the H₂ ambient. They also found Si etching to be faster than the reaction of H₂ with the native oxide, thus resulting in surface roughness.

Besides the reaction of various gaseous species with Si, other possible effects such as thermal etching [94] during the pretreatment may also roughen the Si surface.

3.6.2 Si reaction with O₂

We had originally planned to generate nrSi through the active oxidation of Si with the generation of volatile SiO according to



However, as noted by Ref. [95, 96], in order to prevent the passive oxidation of Si according to



the O₂ concentration must be lower than a critical value that is given by [95]

$$P_c(T) = P_0 \exp(-\Delta E / kT), \quad (3.6.5)$$

where $P_0 = 4.4 \times 10^{12}$ Torr and $\Delta E = 3.93$ eV for (111) Si, and $P_0 = 2.0 \times 10^{12}$ Torr and $\Delta E = 3.83$ eV for (001) Si as shown in Fig. 3.6.1 after Ref. [95]. For our maximum sample operating temperature of 850 °C, $P_c = 1.3 \times 10^{-5}$ Torr, which is a condition that is difficult to achieve with our equipment. Thus the reaction of (001) Si with O₂ will proceed as passive

oxidation thermally generating SiO₂.

Figure 3.6.2 presents the variation of the height of the E₁ (3.15 eV) and E₂ (4.06 eV) peaks in Si <ε_i> obtained during a typical thermal oxidation process at 800 °C. Under these conditions a passivating SiO₂ layer is formed. This was confirmed by post-oxidation ellipsometric measurements, where removal of the overlayer by HF was observed.

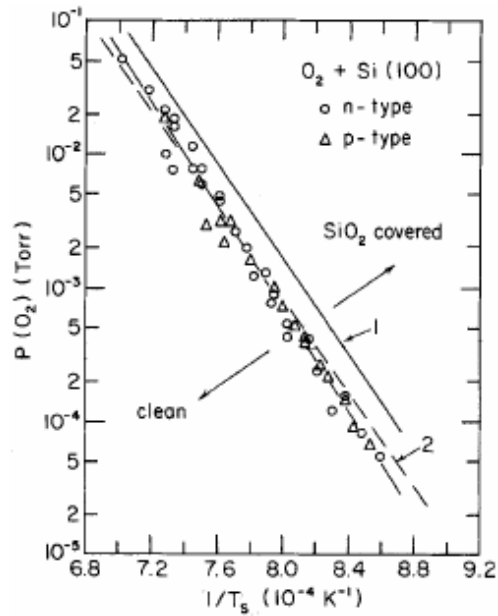


Fig 3.6.1 Critical concentration of O₂ for the transition between active and passive oxidation, after Ref. [95].

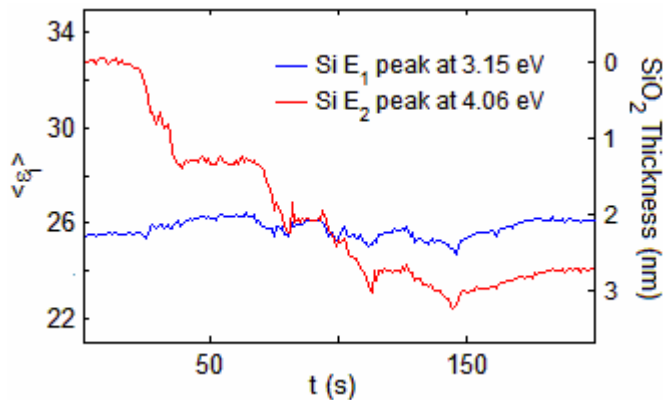
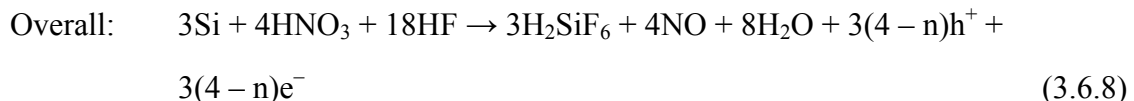
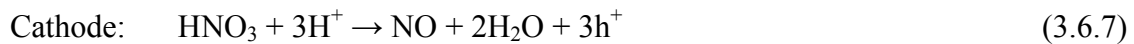
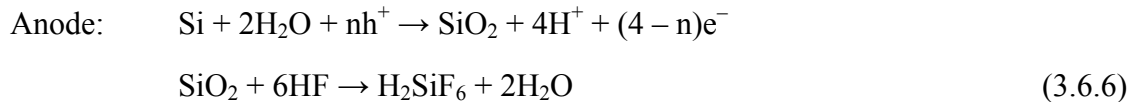


Fig 3.6.2 Variation of ϵ_2 at 3.15 and 4.06 eV observed during thermal oxidation of (001) Si at 800 °C.

We have observed that the reproducibility of GaP growth on thermally generated SiO₂ is generally poor because the initial thermal oxidation process is sample-dependent. Even though we follow the same procedure, different saturation thicknesses and morphologies were obtained on different Si wafers. For example, wafers with higher surface defect densities exhibit more etch pits following oxidation due to competition with active oxidation. Therefore the heteroepitaxy results of GaP on oxidized Si should be viewed with some caution.

3.6.3 Isotropic etching of Si by HF + HNO₃ + H₂O

The etching of Si using chemical solutions usually proceeds through Si oxidation following by SiO₂ reduction. For mixtures of HF, HNO₃, and H₂O, the oxidizing reagent is HNO₃ and the reducing reagent is HF. The reaction can be viewed as an electrochemical anodizing process [97]:



where n (= 2 to 4) is the average number of holes required to dissociate one Si atom.

Etching from various concentrations of HF:HNO₃:H₂O at 25 °C has been studied by Schwartz and Robbins, as shown in Fig. 3.6.3 after Ref. [98]. The etching rates are listed as the numbers on the contour in mils/min (1 mils/min = 0.42 nm/s). At high rates etching is diffusion-limited and isotropic. In this work we used the HF:HNO₃:H₂O compositions 1:1:1 and 1:3:5 respectively. The positions of these mixtures are marked on Figure 3.6.3. Our etching rates are expected to be smaller than 0.25 nm/s, which will assist roughening.

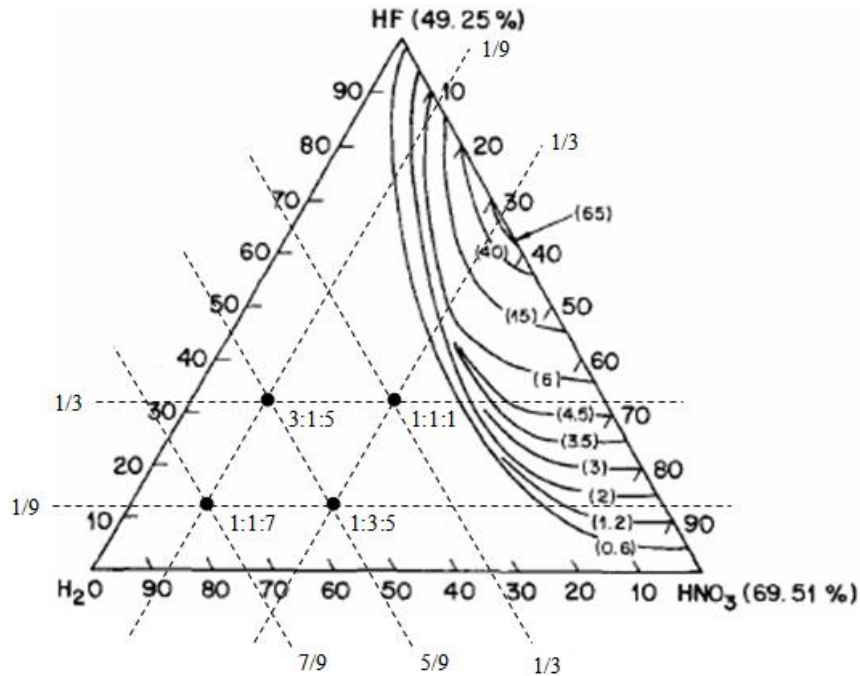


Fig 3.6.3 Si etching rates in mils/min for different solution compositions at 25 °C, after Ref. [98].

Figure 3.6.4 presents the AFM micrographs of (001) Si that had been etched in 1:1:1 solutions for (a) 10 s and (b) 30 s. The corresponding RMS roughnesses are 2.95 nm and 7.15 nm, respectively. The surface consists of randomly distributed concave etch pits with dimensions smaller than 50 nm. However it should be noticed that the AFM probe has a radius larger than 20 nm, thus any lateral features with dimension smaller than that cannot be resolved. Figure 3.6.5 presents the SE spectra for the same samples along with three-phase-model fittings. The parameters describing the top rough layers are 74.67% Si and 3.69 nm thickness in the former case, and 56.59% Si 6.74 nm in the later.

Figure 3.6.6 presents AFM micrographs of (001) Si etched in 1:3:5 solutions for (a) 1 min (1.49 nm), (b) 3 min (1.96 nm), (c) 4 min (5.81 nm), (d) 5 min (9.09 nm), (e) 6 min (16.12 nm) and (f) 7 min (27.22 nm). The RMS roughnesses are given in the brackets. Figure 3.6.7 presents the SE spectra for the same samples, along with one that had been

etched for 2 min. The spectra in Figure 3.6.7 (c) and (d) exhibit oscillation patterns, from which the rough layer thickness can be estimated to be 251 nm for 5 min, 282 nm for 6 min and 315 nm for 7 min etching. However, the corresponding RMS roughnesses in Figure 3.6.6 only have values of the order of or less than 30 nm. This means that prolonged etching in 1:3:5 solutions generates thick layers of porous Si (pSi), the structure of which can only be probed by SE and not AFM.

We believed that it would be interesting to study GaP heteroepitaxy on pSi, however the pSi samples were destroyed at growth temperatures. Figure 3.6.8 presents the change of pSi $\langle \epsilon \rangle$ at 600°C under 4 Torr (a) H₂ for 250 s, and (b) N₂ for 430 s. It can be seen that the oscillation pattern gradually shrinks, which means that the porous structure is lost. The reason is that the porous Si layer is actually a compound of various species such as H, O, Si, and maybe also F and N. When heated it dissociates thereby changing the SE spectrum. The discussion of the effect of heat treatment on pSi can be found in many places, for example Ref. [99].

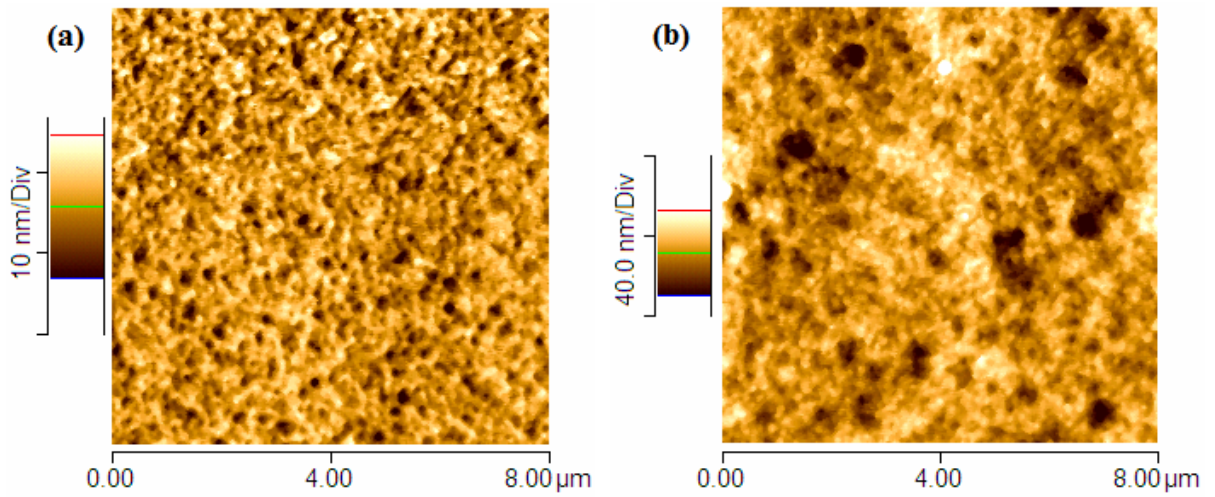


Fig 3.6.4 AFM micrographs of (001) Si etched in HF:HNO₃:H₂O = 1:1:1 solutions for (a) 10 s and (b) 30 s.

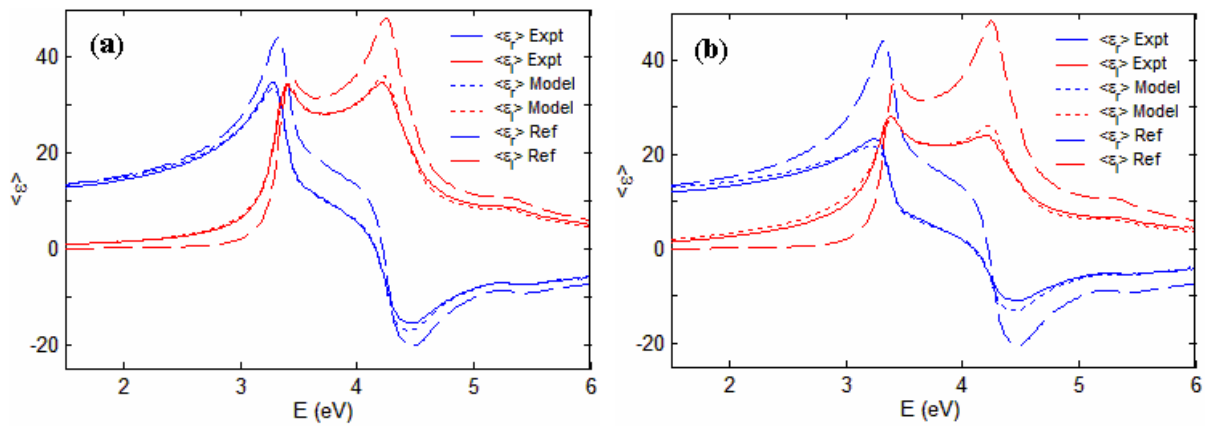


Fig 3.6.5 SE spectra for the samples of Fig. 3.6.4.

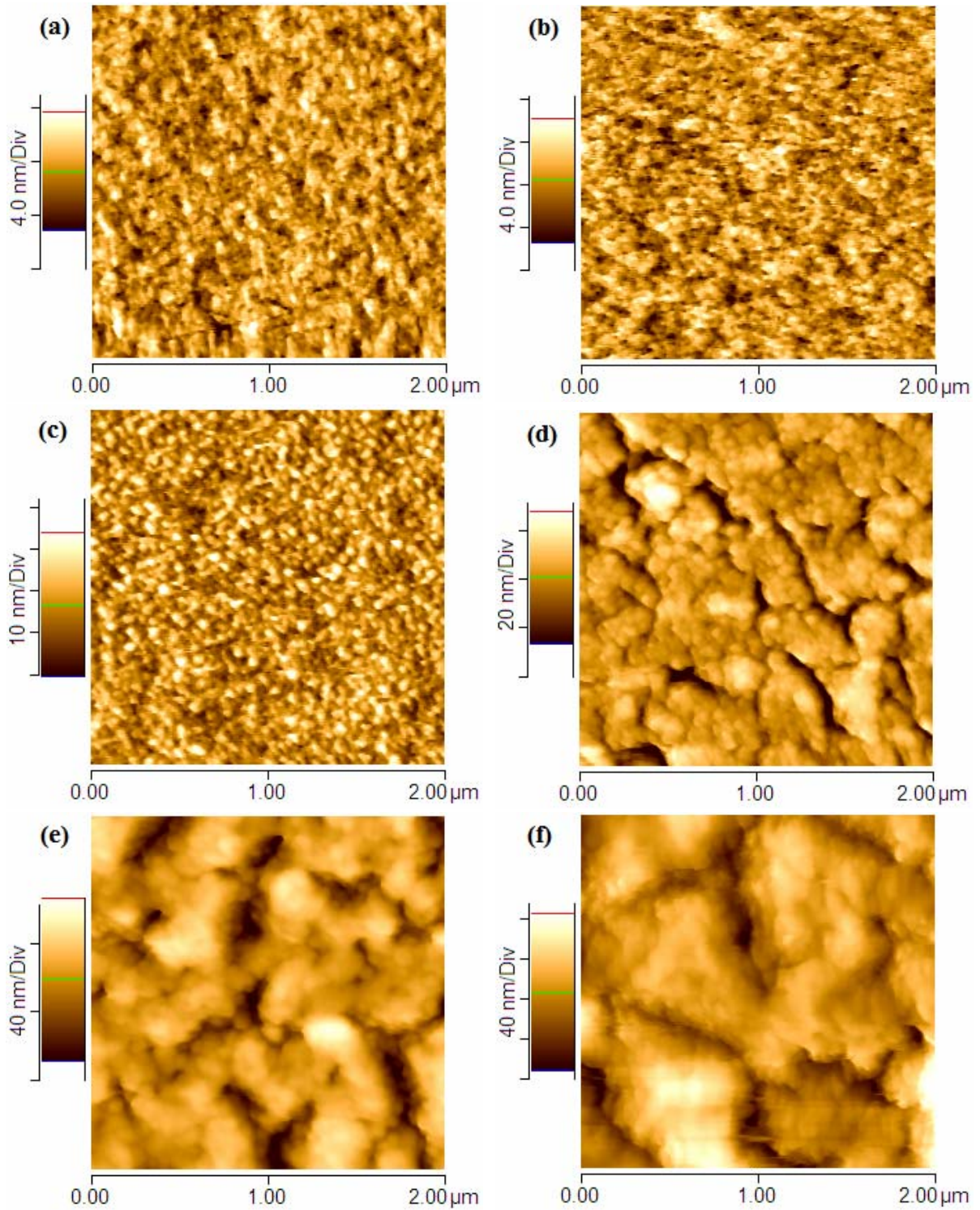


Fig 3.6.6 AFM micrographs of (001) Si etched in HF:HNO₃:H₂O = 1:3:5 solutions for (a) 1 min, (b) 3 min, (c) 4 min, (d) 5 min, (e) 6 min and (f) 7 min.

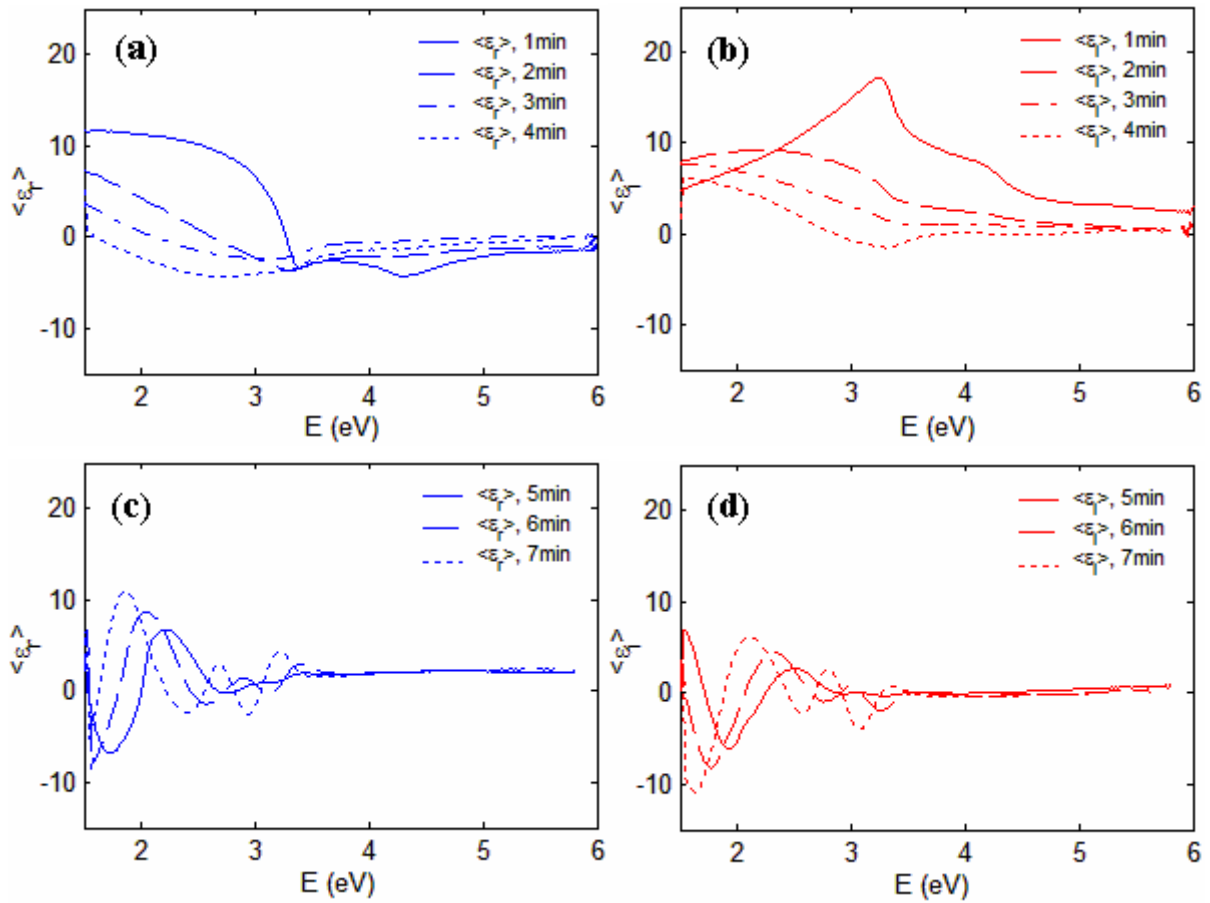


Fig 3.6.7 SE spectra for the samples in Fig 3.6.6, with (a) $\langle \epsilon_r \rangle$ and (b) $\langle \epsilon_i \rangle$ for (001) Si etched for 1 – 4 min, and (c) $\langle \epsilon_r \rangle$ and (d) $\langle \epsilon_i \rangle$ for (001) Si etched for 5 – 7 min.

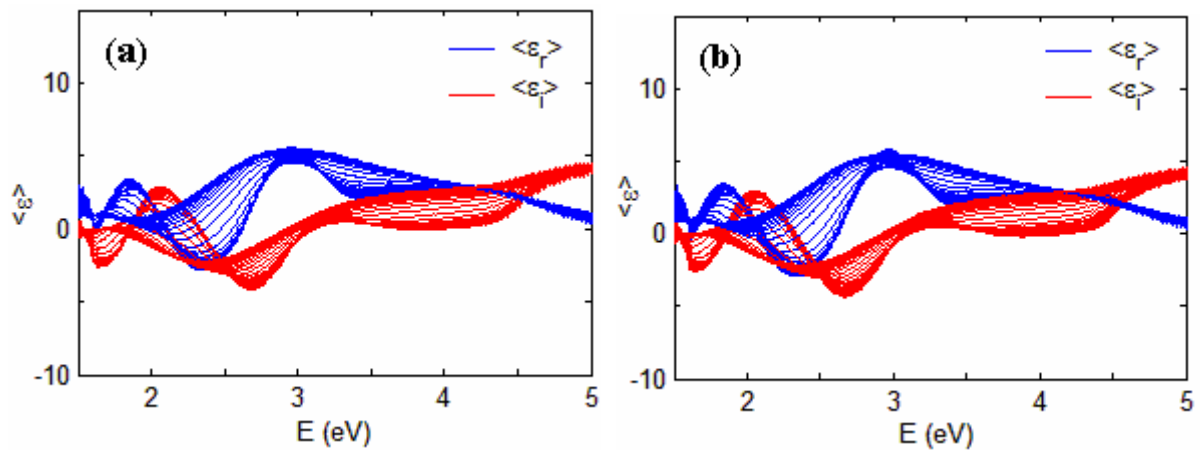
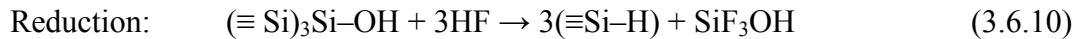
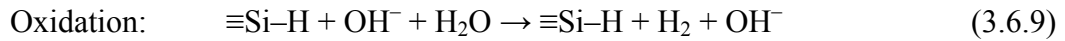


Fig 3.6.8 Evolution of pSi spectra at 600°C under 4 Torr (a) H₂ for 250s, and (b) N₂ for 430 s.

3.6.4 Anisotropic etching of Si by NH₄F and NH₄OH

Another method for generating nrSi is to use weak solutions of NH₄F and NH₄OH. Here temperatures of about 80°C are preferred in order to increase the dissociation equilibrium constant. The etch rate is strongly orientation-dependent, and usually much faster for {001} than for {111} surfaces. Thus the etching is reaction-rate limited and anisotropic in nature [100, 101].

The etching of Si by NH₄F solutions is found to be highly site-selective, and the following mechanism has been proposed [102]:



Here, oxidation is the rate-limiting step, with etching rates ranked as kink > dihydride step > monohydride step >> terrace [102, 103]. These are defined in Fig. 3.6.9 for a (111) Si surface, after Ref. [102].

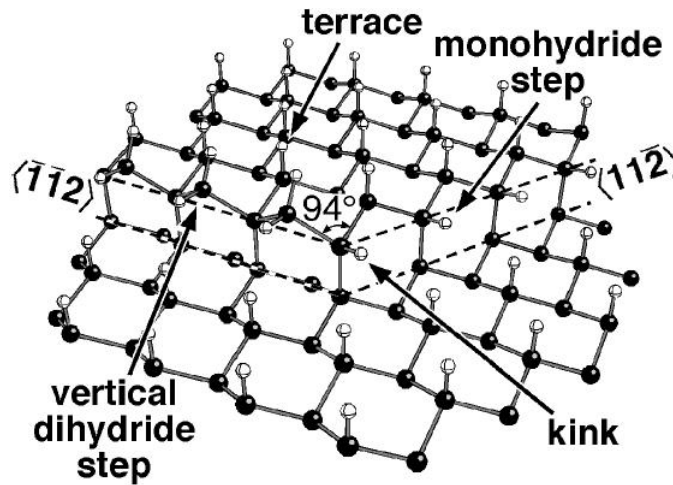


Fig 3.6.9 Systematic representation of various surface features on a vicinal (111) Si surface, after Ref. [102].

The etching mechanism of Si using base solutions such as NH_4OH follows the steps [104]:



Here, H_2O first attacks a Si-Si back bond, then OH^- attacks the Si-H bond that is generated. The process repeats until a water-soluble molecule of silicic acid is generated. The overall reaction for dissolving one Si atom is [104]

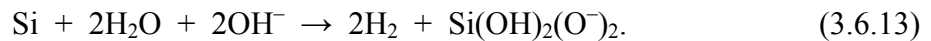


Figure 3.6.10 presents the AFM micrographs of (001) Si etched at 80°C in (a) 1% NH_4F for 7 min, and (b) 1% NH_4OH for 5 min, with RMS roughness 11.72 nm vs. 6.11 nm respectively. The surfaces are mainly composed of regularly shaped grains exposing $\{111\}$, $\{211\}$, or similar low energy facets. Figure 3.6.11 presents the SE spectra for the same samples along with three-phase-model fittings. The parameters describing the top rough layers are (a) 48.39% Si 10.96 nm and (b) 56.22% Si 6.17 nm.

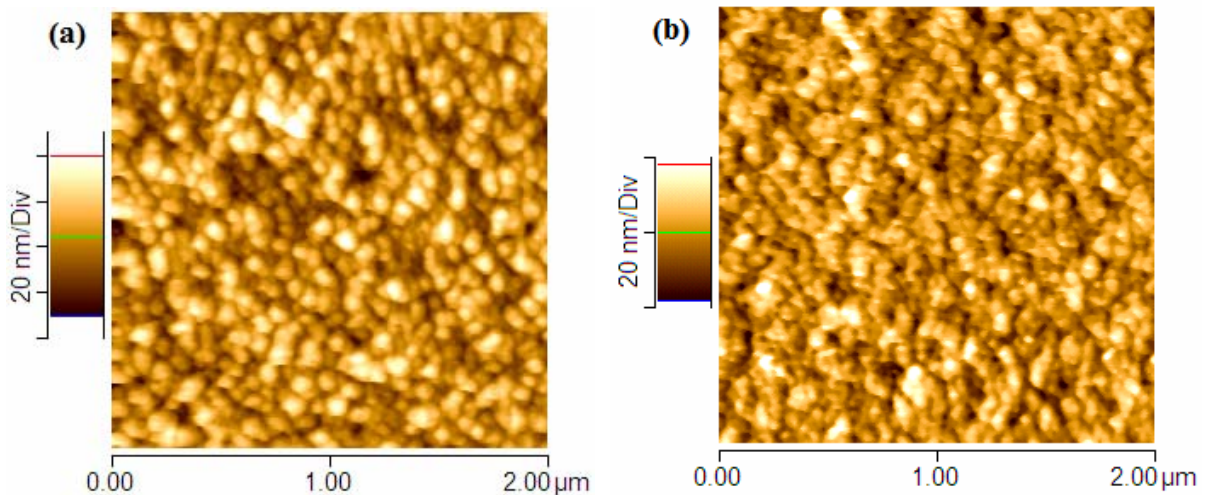


Fig 3.6.10 AFM micrographs of (001) Si etched at 80°C in (a) 1% NH_4F for 7 min, and (b) 1% NH_4OH for 5 min.

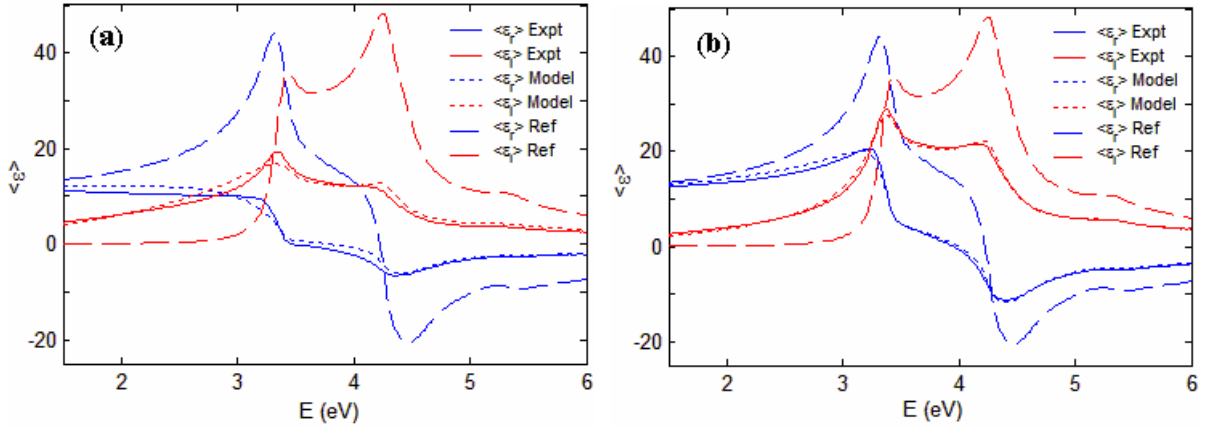


Fig 3.6.11 SE spectra for the samples in Figure 3.6.10.

A summary is given here for the methods mentioned above. The first two methods of using H_2 etching and active oxidation to generate nrSi are not implemented due to our system limitations, since the sample temperature cannot be brought up higher than $900^\circ C$ and the pressure cannot be brought down lower than 0.1 Torr. Nevertheless passive oxidation is used to generate SiO_2 thermally.

Chemical etching can generate nrSi surfaces with various degrees of roughness. Etching by mixtures of HF, HNO_3 , and H_2O is usually rapid, and is diffusion-limited and isotropic. The nrSi generated usually exhibits randomly distributed fine structures of mainly concave etch pits with dimensions smaller than 50 nm. Thus it may contain a high density of kink sites. On the contrary, etching by weak solutions of NH_4F or NH_4OH at elevated temperatures is usually slow, and is reaction-rate limited and anisotropic. The nrSi surfaces generated are mainly composed of regularly shaped convex grains exposing $\{111\}$, $\{211\}$, or similar low energy facets. Since the anisotropic etching rates are higher for kinks and steps, the densities of such sites are expected to be very low, which makes the nrSi not suitable for our purpose of increasing the initial nucleation density. This is consistent with our data on the heteroepitaxy of GaP on both types of nrSi surfaces, which is reported in the next Chapter.

Chapter 4 Results and Discussion

4.1 GaP Heteroepitaxy on (001) GaAs

4.1.1 Growth and characterization

The GaAs substrates used here are 2” n-type epi-ready wafers oriented within $0 \pm 0.1^\circ$ of (001). They were obtained from American Xtal Technology. They were used as-is without any surface treatment.

We selected 6 representative depositions are selected for detailed analysis. Growth conditions are listed in Table 4.1.1. The 6 runs were grouped into 3 categories according to precursor arrival rates: normal, PH₃-deficient, and TMG-burst. In normal growth the flows of TMG and PH₃ flows are nominally constant, although small deviations can occur, e.g., if TMG is flowing into the chamber when the pressure in the bubbler is changed. We realize short periods of PH₃-deficient growth by holding the TMG flow constant while reducing the PH₃ flow significantly. Typical V/III ratios here are about 10 compared to normal values of at least 3000. The TMG burst mode deviates from normal growth by keeping the PH₃ flow constant while decreasing the pressure in the TMG bubbler. This introduces TMG at a very high flow rate for about 10 seconds, briefly reducing the V/III ratio by one or more orders of magnitude and causing a corresponding increase in the growth rate. The high growth rate distinguishes the burst mode from the PH₃-deficient mode above.

The choice of the growth conditions above are based on the following considerations. It is relatively easy to grow GaP heteroepitaxially on GaAs over a fairly wide range of temperatures, thus the temperature differences among the different runs shown in Table 4.1.1 are unimportant. Although continuous GaP epilayers can be obtained at V/III ratios as low

as several hundred, higher V/III ratios generally yield better material. Thus 3 deposits, run A, B, and C, are done in the normal growth mode but with varying V/III ratios. As suggest by nucleation theory, increasing the precursor supersaturation reduces the nucleation barrier energy and the critical nucleus size, and the initial nucleation density increases accordingly. For the two precursors used here, Ga is generally thought as the rate-limiting species, while P is always available in larger quantities than needed, so it is already highly supersaturated. Thus 2 depositions, E and F, are done in the TMG-burst mode so we can study the effect of Ga supersaturation on initial nucleation and growth rate. A TMG burst also results in a low V/III ratio, but this can be partially overcome by using a higher PH₃ flow, as done in run F. A PH₃-deficient run D is included to study growth under the same low V/III ratio as the above, but by reducing the flow of PH₃ instead of increasing that of TMG. Thus the growth rate does not experience a sudden change.

These 6 depositions well serve our purpose, which is to obtain baseline information about heteroepitaxy of chemically matched systems for comparison to the more challenging problem of III – V heteroepitaxy on Si. The growth rate obtained in normal growth mode is directly comparable to that of Si heteroepitaxy under the same growth conditions, since the same homoepitaxy process will become dominant as soon as a continuous GaP layer is formed. Since the GaP epilayer quality is usually better when grown on GaAs, the mechanism of homoepitaxy is easier to identify. It is also applicable for the study of growth on Si. The information gained from the TMG-burst and PH₃-deficient modes will also be instructive for Si heteroepitaxy, such as to determine whether the initial nucleation density can be improved under higher Ga supersaturations and whether low V/III ratios should be avoided.

We now present our results, and defer further discussion on growth rates and mechanisms until Section 4.5. Figure 4.1.1 presents post-deposition $\langle \epsilon \rangle$ data from 1.5 to 6 eV obtained on these samples by SE, together with the results of four-phase-model analysis.

The top GaP oxide was removed prior to measurement using a solution of 10% NH₄OH in water. The fitting parameters in the four-phase model (bulk concentration, bulk GaP thickness, top GaP thickness assuming 50% void concentration) are summarized in Table 4.1.2. Figure 4.1.2 shows AFM micrographs taken near the center region of the final films, and the RMS roughness is also summarized in Table 4.1.2. It can be seen that the RMS roughness measured by the AFM is much larger than the thickness of the rough-surface layer obtained from SE, although the SE data are unrealistic for reasons already discussed in Sec. 2.2.3.

Real-time SP analyses of some of these growth runs are provided in Figs. 4.1.3, 4.1.4, 4.1.6 and 4.1.8. These show (a) RI and (b) $\langle \epsilon \rangle$ data at 2.64 eV together with least-squares-model fitting for the initial stages of runs # A, B, E, and F, respectively. The extracted growth rates and GaP compositions are summarized in Table 4.1.3. Data for the entire TMG-burst growth runs E and F are also shown in Figs. 4.1.5 and 4.1.7.

Table 4.1.1 Growth conditions for representative GaP/GaAs depositions.

Run	Type	T (°C)	PH ₃ (sccm)	TMG (sccm)	V/III	Carrier Gas	Rot.
A	Normal	570	1700	0.52	3269	H ₂	Y
B	Normal	570	1700	0.25	6800	H ₂	Y
C	Normal	580	200	0.38	526	H ₂	N
D	PH ₃ -Deficient	600	10 / 200	0.38	26 / 526	N ₂	N
E	TMG-Burst	620	200	13 / 0.93	15 / 215	H ₂	N
F	TMG-Burst	580	1000 / 200	14 / 0.38	71 / 526	H ₂	N

Table 4.1.2 Characterization parameters for the GaP/GaAs depositions in Table 4.1.1.

Run	SE Bulk GaP Comp. (%)	SE Bulk GaP Thickness (nm)	SE Top GaP Thickness (nm)	AFM RMS Roughness (nm)
A	96.9%	76.0	0.18	0.9
B	100%	208.5	0.20	0.9
C	96.9%	130.5	0.16	1.6
D	97.9%	153.7	0.03	3.2
E	94.7%	279.9	0.38	3.4
F	95.9%	156.1	0.17	3.9

Table 4.1.3 Initial stage growth parameters for several GaP/GaAs depositions in Table 4.1.1.

Run	Duration (s), with steps in SE	Growth Rate (nm/s), with uncertainties	GaP Comp. (%), with uncertainties
A	17 (323 – 340)	0.10 (0.004)	71.5 (2.4)
	25 (340 – 365)	0.12 (0.004)	77.8 (2.0)
B	71 (10 – 81)	0.01 (0.0004)	65.7 (2.2)
	69 (81 - 150)	0.03 (0.0004)	100
E	2 (345 – 347)	1.77 (0.23)	81.2 (7.3)
	4 (347 - 351)	1.81 (0.02)	96.6 (0.5)
F	4 (84 – 88)	2.11 (0.09)	99.5 (1.7)
	4 (88 - 92)	2.12 (0.09)	96.6 (1.4)

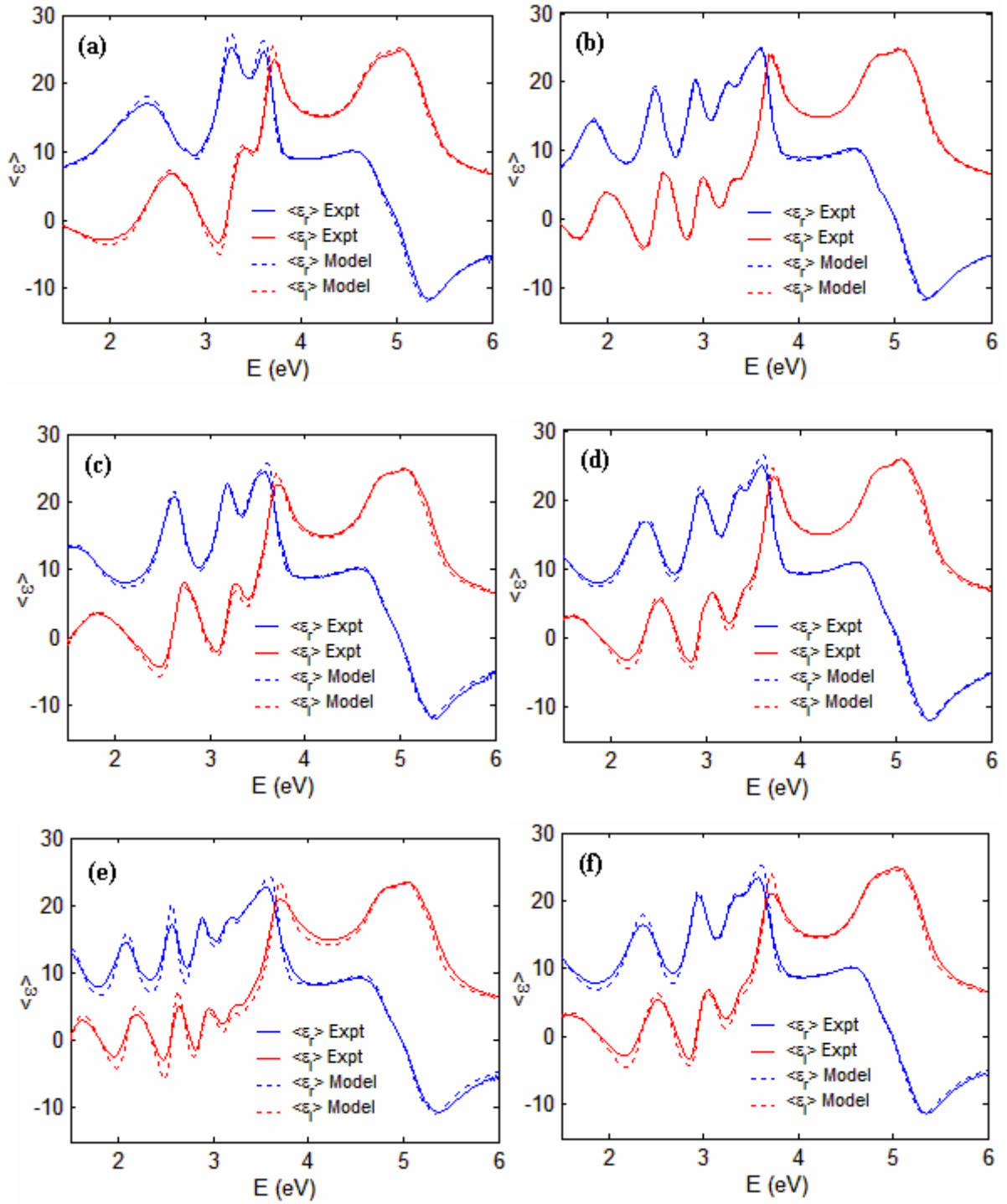


Fig 4.1.1 $\langle \epsilon \rangle$ from 1.5 to 6 eV for GaP/GaAs depositions A - F measured with the bench SE, together with least-squares fitting with the four-phase model.

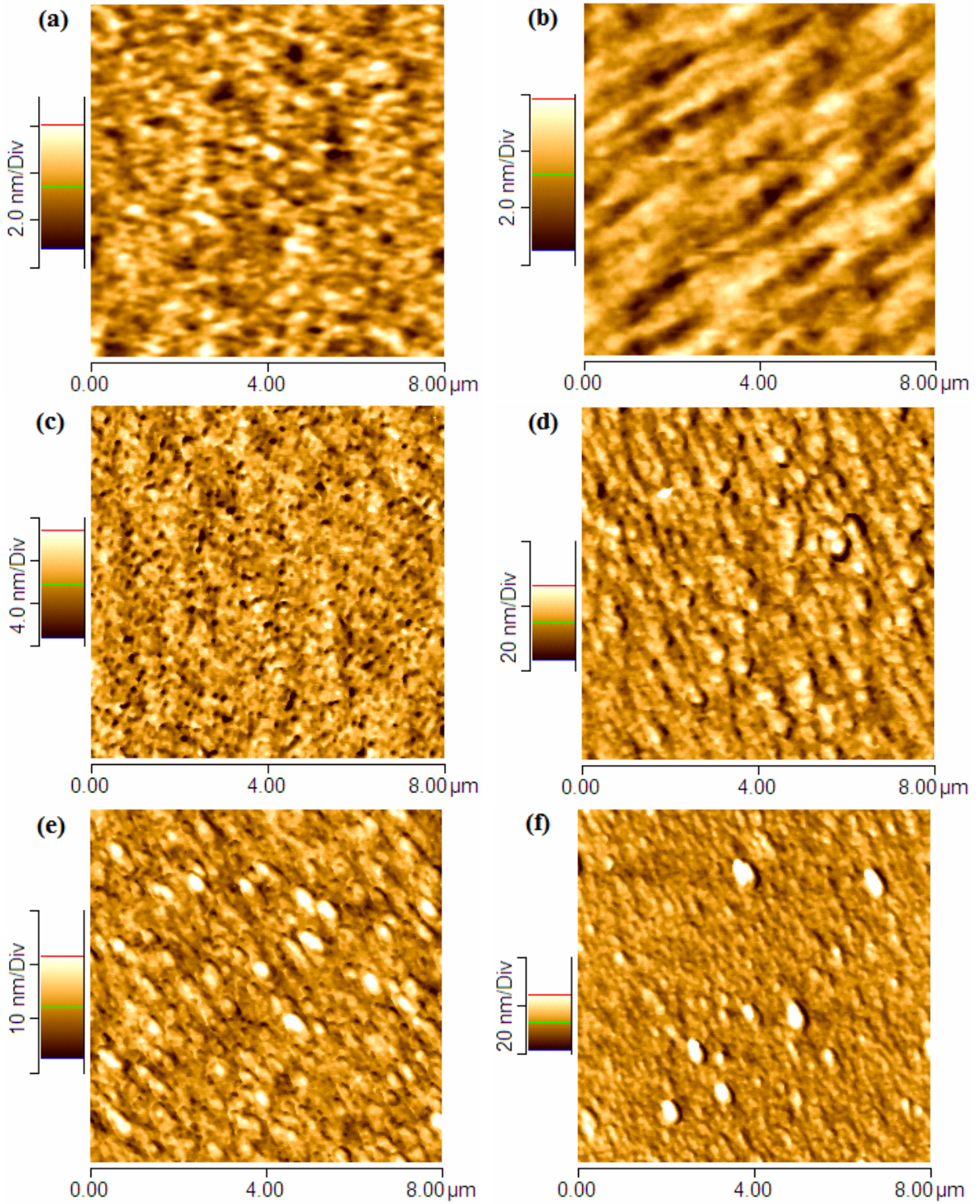


Fig 4.1.2 AFM micrographs for GaP/GaAs depositions A - F.

It can be seen that continuous heteroepitaxial GaP films were grown on (001) GaAs in all cases, and that the surface roughnesses of the films are related to the V/III ratio.

Runs A, B, and C, done under normal growth conditions, have very smooth surface morphologies as revealed by AFM. Run C with V/III = 526 and a TMG flow 0.38 sccm has a slightly larger RMS roughness of 1.6 nm. Run A uses V/III = 3268 and a TMG flow of 0.52 sccm, and the RMS roughness is lower, of 0.9 nm. Run B has the largest V/III ratio of 6800 and the smallest TMG flow of 0.25 sccm. This gives the smoothest surface of all. The grains show a preferable binding direction, and the surface is rugate due accumulated lattice strain. The bulk GaP crystalline quality of run B is also the best, with a concentration that is modeled at 100%, compared to 96.9% for runs A and C.

The initial stage of heteroepitaxy is also closely related to growth conditions. For the first 17 s of run A the growth rate is 0.10 nm/s, and the overlayer is 72% GaP plus voids. In the next 25 s the growth rate changes to 0.12 nm/s and GaP concentration to 78%. The initial growth rate of run B is only 0.01 nm/s, and for the first 71 s the epilayer consists of 67% GaP plus voids. After that the GaP concentration increases to 100%. The average homoepitaxial growth rates are 0.15 and 0.13 nm/s for runs A and B, respectively. It is only 0.06 nm/s for run C, which has a larger TMG flow than run B but is grown with no spindle rotation.

The film morphologies are generally poorer, for growth runs D, E, and F, which are done under short exposures of an irregularly smaller V/III ratio, obtained either by decreasing PH₃ flow (D) or by increasing TMG flow (E and F).

The PH₃-deficient growth run D uses a V/III ratio of 10 for the initial 80 s, which is then raised to 526 by increasing PH₃ flow. The bulk film has an average GaP concentration of 97.89% by four-phase-model fitting, but the AFM micrographs show that the surface has a large RMS roughness of 3.19 nm. Thus the grain boundaries and roughness generated at the

initial stage propagate through the film as growth continues. Although the grain boundaries appear to be terminated and become internal, the roughness could not be eliminated, at least on the thickness scale when growth is terminated (153.73 nm).

TMG-burst growth runs E and F were initiated by multiple TMG bursts before continuous growth, with each generated by reducing the pressure in the TMG bubbler by setting the PC of the TMG bubbler to a lower value. After each burst the TMG input line was valved off to allow pressure to build up inside the bubbler for the next burst, or to deliver a normal flow. Meanwhile PH_3 was kept flowing to prevent the grown material from deteriorating.

Run E achieved two TMG bursts by changing the PC from 300 to 100 Torr. The input H_2 carrier gas is kept at 9 sccm by the MFC, and the TMG temperature is -16°C . The TMG flow before and immediately after the burst with the PC stabilized is calculated to be 0.93 and 3.50 sccm respectively. However, the actual TMG flow that enters the chamber could be as high as ~ 13 sccm, if we assume that the growth rate is proportional to the TMG partial pressure. It should be noted that the TMG flow profile vs. burst time is thus deduced indirectly and may not be accurate. The PH_3 flow of 200 sccm is fixed during growth, so the V/III ratio could range from 15 to 57 during bursts and is 215 afterwards. For the initial 2 s the growth rate is 1.77 nm/s and GaP concentration is 81%, and they change to 1.81 nm/s and 97% in the next 4 s.

Run F uses three TMG bursts, accomplished by changing the PC from 400 to 200 Torr, with 5 sccm input H_2 and same TMG temperature of -16°C . The TMG flows before and immediately after the burst are 0.38 and 0.81 sccm, respectively. The maximum flow during the burst is ~ 14 sccm. PH_3 flow is 1000 sccm during the TMG bursts and 200 sccm afterwards, thus the V/III ratio varies between 71 and 1235 during bursts and is 526 for continuous growth. For the initial 4 s the growth rate is 2.11 nm/s and GaP concentration is 99%. These values change to 2.12 nm/s and 97% in the next 4 s.

Despite the high growth rate, TMG bursts in general result in poorer material qualities. Runs E and F have bulk GaP concentrations of 94.7% vs. 95.9%, and AFM RMS roughnesses of 3.4 nm vs. 3.9 nm, respectively. Both films are terminated with large clusters of ~ 500 nm in diameter, which probably originated from the grain boundaries generated during TMG bursts. The cluster density is smaller for run F, which is done under larger PH_3 flow. The high surface roughness was not eliminated by homoepitaxy.

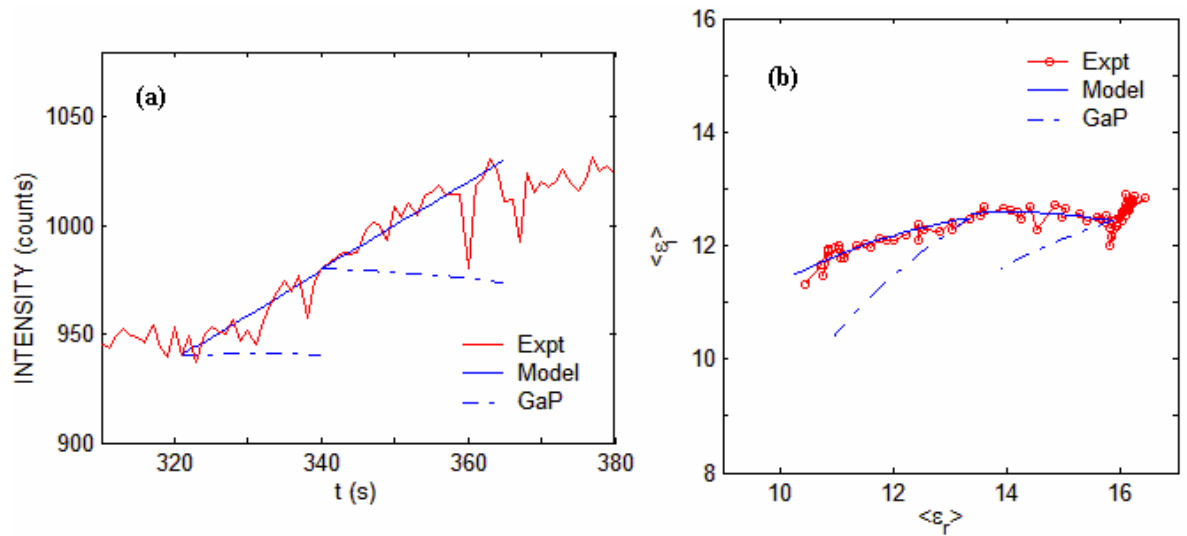


Fig 4.1.3 (a) RI and (b) $\langle \epsilon_r \rangle$ data at 2.64 eV for the initial stage of GaP/GaAs run A.

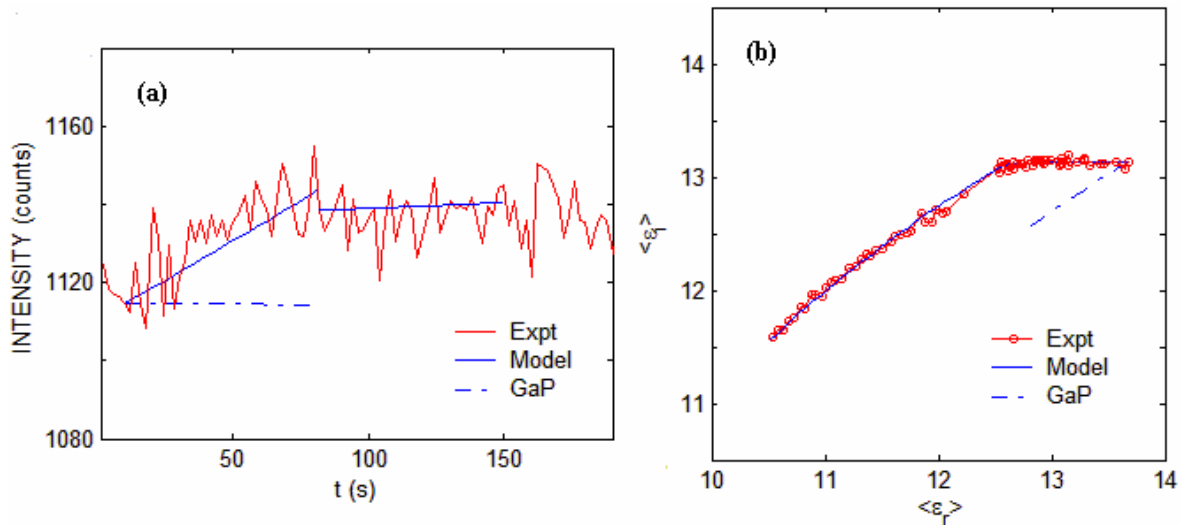


Fig 4.1.4 As Fig 4.1.3, but for run B.

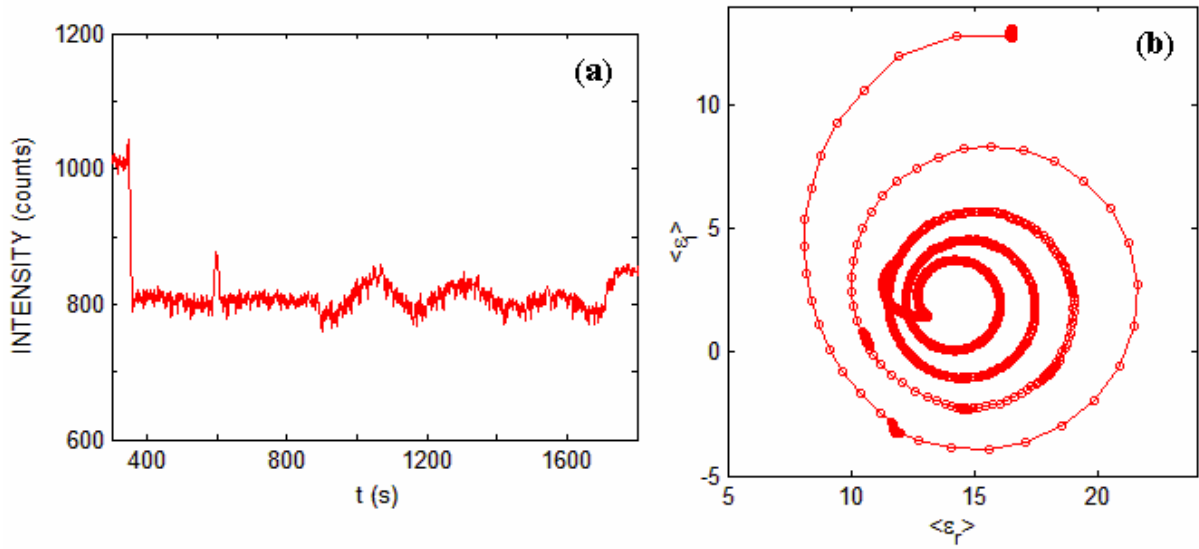


Fig 4.1.5 Complete (a) RI and (b) $\langle \epsilon_r \rangle$ data at 2.64 eV for GaP/GaAs growth run E.

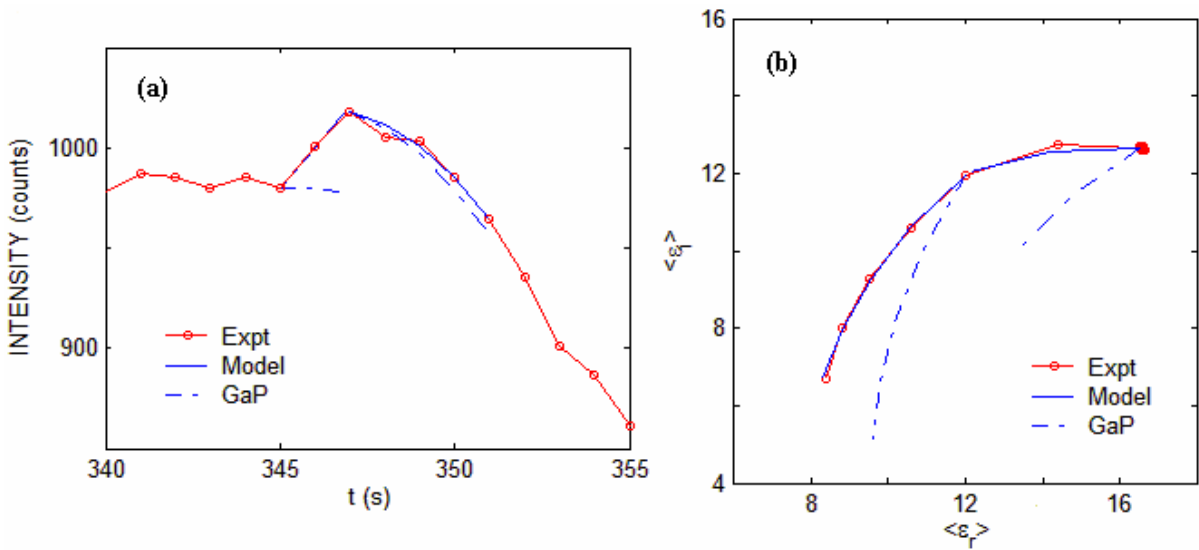


Fig 4.1.6 (a) RI and (b) $\langle \epsilon_r \rangle$ data at 2.64 eV for the initial stage of GaP/GaAs run E.

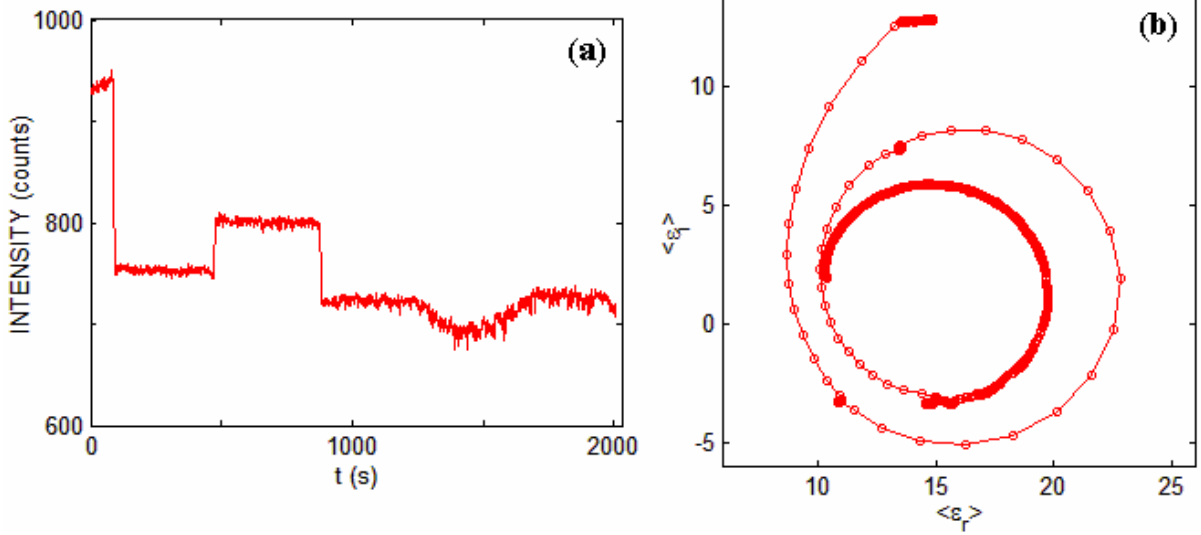


Fig 4.1. 7 As Fig 4.1.5, but for run F.

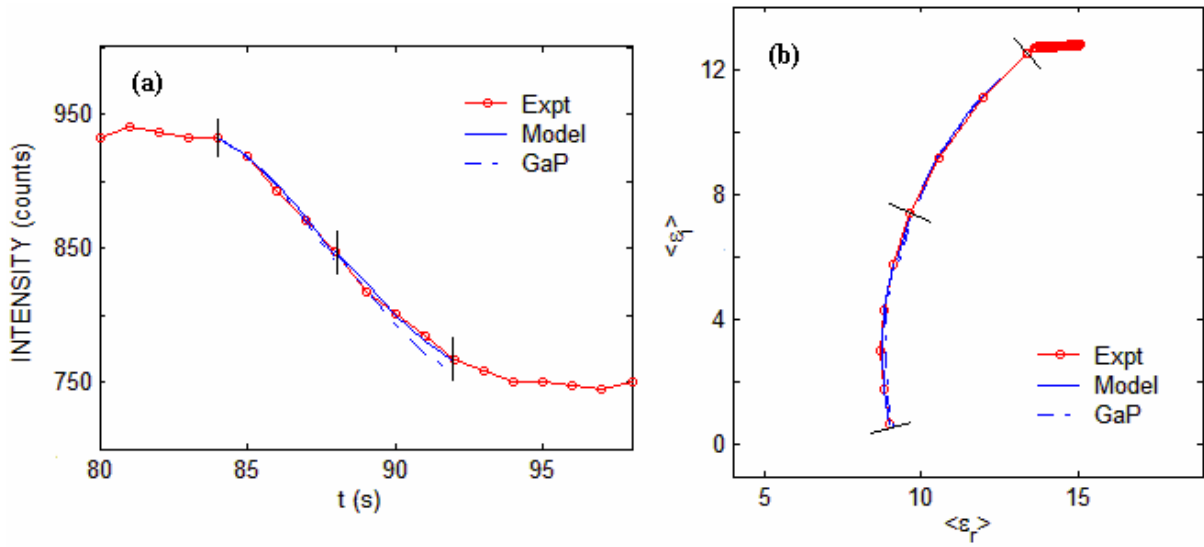


Fig 4.1.8 As Fig 4.1.6, but for run F.

We next consider P – As exchange, which is a process that can occur in GaP / GaAs heteroepitaxy before growth is initiated. The decomposition temperature of GaAs is about 580 °C. Above this temperature As evaporates as As₂, leaving Ga droplets behind. Thus GaAs substrates usually start to deteriorate when brought to growth temperatures in the absence of AsH₃. If PH₃ is flowing instead of AsH₃, some P - As exchange will occur as the supersaturation P in the gas phase will replace the evaporating As. This is also consistent from a bond-strength point of view. The bond dissociation energy is 229.7 kJ/mol for Ga – P and 202.5 kJ/mol for Ga – As. Hence the former is favored. From expected values of the exchange current, the GaP layer should form at a rate of the order of 0.001 nm/s. If the TMG flow is initiated along with that of PH₃, growth will occur immediately but the initial heteroepitaxial rate is slightly smaller than the homoepitaxial growth rate.

Figure 4.1.9 shows an example of P - As exchange taken from growth run # C. The composition and growth rate are fitted using the least-square method. The parameters are found to be: 72.7 (± 0.5)% GaP + 27.3% voids at 0.0030 (± 0.00002) nm/s for t = 1 to 83s, and 80.1 (± 0.4) % GaP + 19.9% voids at 0.0034 (± 0.00002) nm/s for t = 84 to 170s.

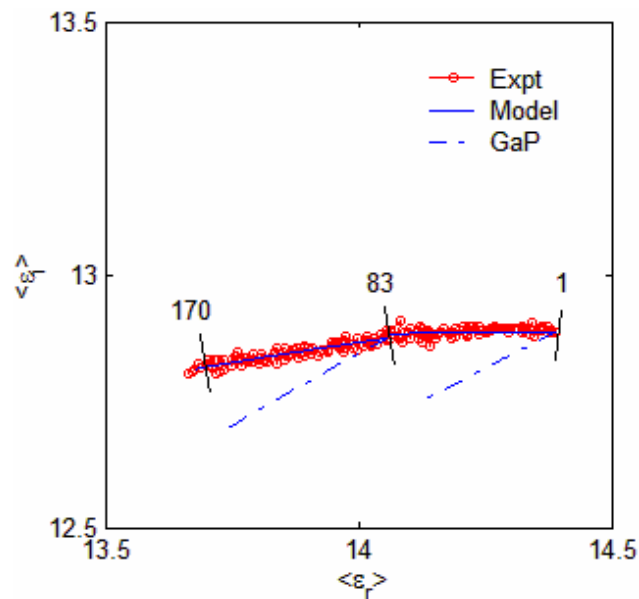


Fig 4.1.9 $\langle \epsilon \rangle$ during the initial phase of run C under PH₃ only, illustrating P - As exchange.

4.1.2 Lateral thickness profile of GaP / (001) GaAs

One of the common characteristics that we observe is that the thickness of a deposited film is generally different at the edges of a wafer than at its center. This is independent of whether the sample is rotated or not, and is not due to depletion of the supply of TMG in the gas phase, as is usually assumed.

Figure 4.1.10 presents the lateral thickness profile of the normal growth run A, with $x = 0$ and 25.4 representing the center and edge of the wafer, respectively. These data were obtained by analyzing multiple $\langle \epsilon \rangle$ spectra recorded with the SE beam restricted to a small spot then stepped across the wafer. Details are provided in Sec 3.5. In the four-phase model analysis the top layers are assumed to contain 50% voids. The effective thickness dependence is accurately described as exponential, specifically $T_E = (74.53 - 0.26 e^{x/5.52 \text{ mm}})$ nm. The film is thinner at the edge than in the center. Since under the relevant conditions growth is mass-transport limited, this shows that the thickness variation is due to out-diffusion of reactants with a characteristic length of 5.52 mm. The corresponding calculated concentration dependence is shown in Fig. 4.1.11 (a), and has the form $\Delta n = -0.0035 e^{x/5.52 \text{ mm}}$ normalized to the center value. Figure 4.1.11 (b) shows the associated calculated diffusion current $J = e^{(x - 25.4 \text{ mm})/5.52 \text{ mm}}$ normalized to the flow at the edge.

Figures 4.1.12 and 4.1.13 present similar data for the normal growth run # C. Here $T_E = (134.31 - 0.58 e^{x/5.98 \text{ mm}})$ nm, $\Delta n = -0.0042 e^{x/5.98 \text{ mm}}$, and $J = e^{(x - 25.4 \text{ mm})/5.98 \text{ mm}}$. As seen from Table 4.1.1, the main difference in growth conditions beyond precursor settings is that run A was done with the sample rotating at 1200 rpm, while the sample in run C is stationary. Although the growth rate for run A is 3 times larger than that of run C, the thickness profiles are essentially the same. Thus despite the claimed need for rotation to achieve uniformity, we conclude that sample rotation has little effect and that the major cause of thickness nonuniformity is lateral diffusion of reactants between the wafer and the susceptor. We will

discuss this in detail in Sec. 4.5.

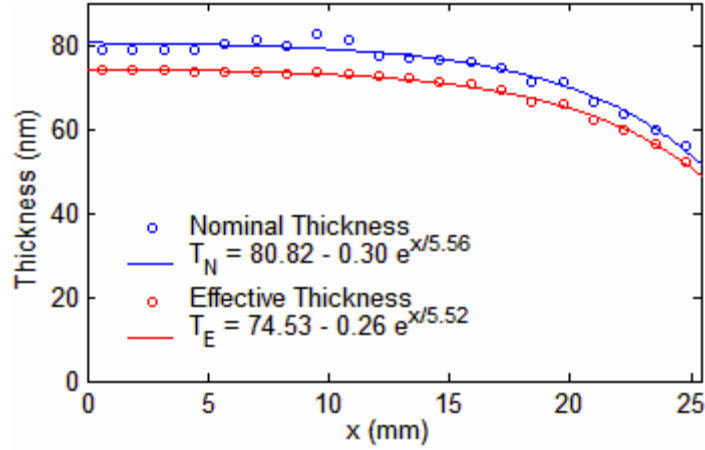


Fig 4.1.10 Lateral thickness profile of GaP / GaAs run A. Thicknesses are in nm, and dimensions in the exponent are mm.

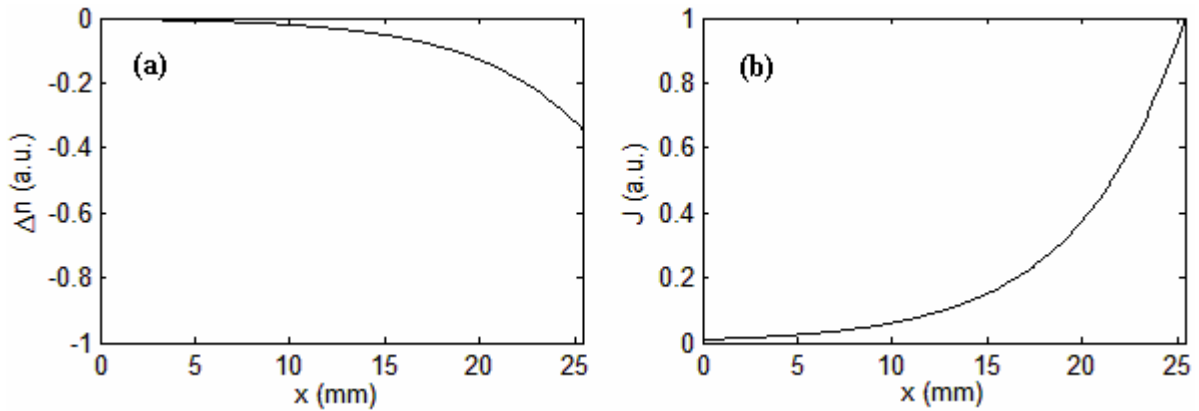


Fig 4.1.11 (a) Calculated concentration dependence of the gas-phase reactants along a radius for GaP / GaAs run A, assuming that the thickness is proportional to concentration. The curve is normalized to the concentration at the center. (b) Calculated diffusion current resulting from (a) normalized to the flow at the edge.

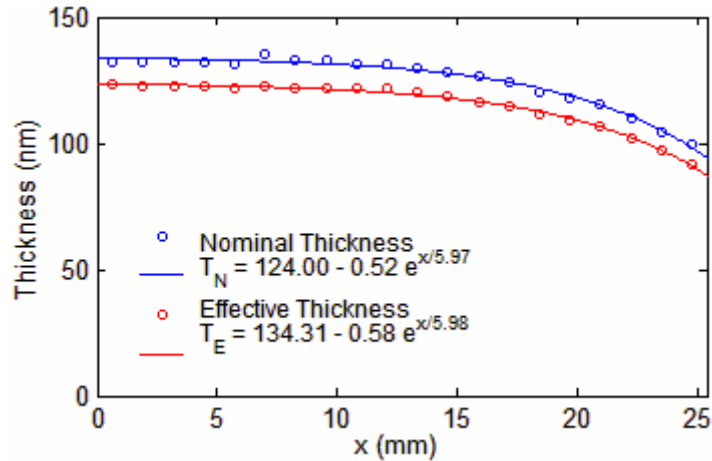


Fig 4.1.12 As Fig 4.1.10, but for run C.

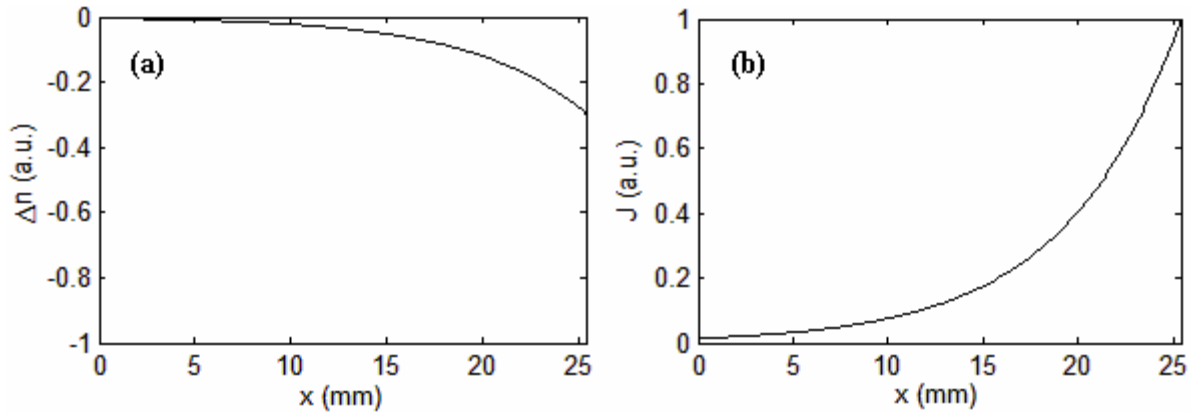


Fig 4.1.13 As Fig 4.1.11, but for run C.

Although the thicknesses are nonuniform, GaP films grown on GaAs under normal conditions are shiny and of similar quality everywhere. The colors at the center and edge regions differ due to interference. This explains the gold center and blue edge of run # A, and the dark green center and gold edge run C. However, films grown under other conditions usually exhibit edge qualities that are significantly worse. Thus runs D, E and F all have shiny dark green centers, but the edge rings are faint blue in runs D and F, and very faint in run E. As an example, in Figure 4.1.14 we show an Epson Scanner image for a

piece of the sample of run E. The featureless shiny center can be contrasted to the faint edge.

The film morphology is also closely related to nutrient flow. For TMG-burst growth, the P concentration does not change but the Ga concentration is at least 10 times larger. The resulting higher growth rate facilitates the depletion of active P species from the gas phase. The net effect is that a reasonably large P/Ga ratio is still maintained over the central part of the film, but as gas is transported outward, the P/Ga ratio becomes smaller. The result is that the growth quality is reasonable at the center, but the material quality is poorer at the edge. The situation could be alleviated by using a higher PH_3 flow rate as in run F. We defer further discussion of this topic to Sec. 4.5.3, where we will also consider growth results obtained with other substrates.



Fig 4.1.14 Photograph of a portion of GaP / GaAs run E.

4.2 GaP heteroepitaxy on (001) Si

4.2.1 Growth and characterization of GaP on non roughened Si substrates

Three representative runs on as-received polished Si substrates are shown here with growth conditions listed in Table 4.2.1. Both singular (001) and vicinal (001) 4° to $\langle 110 \rangle$

substrates were used. They were given a standard RCA clean and a 5% HF rinse before being loaded into the chamber. The resulting surfaces are very smooth with only residual sample defects or atomic-scale steps. The AFM-determined RMS roughness is usually smaller than 0.3 nm. These samples are run as controls to assess the effect of roughening on a nanoscopic scale, data for which will be presented later. Before growth, the substrates were heated to 850 °C under H₂ for 10 min to remove any residual oxide.

Table 4.2.1 Growth conditions for representative GaP / Si runs on as-polished wafers.

Run	Substrate	T (°C)	PH ₃ (sccm)	TMG (sccm)	V/III ratio	Carrier Gas	Rot.
A	(001) 4° off to <110>	500	1600	0.52	3077	H ₂	Y
B	(001) 4° off to <110>	700	1600	0.52	3077	H ₂	Y
C	(001) on-axis	550	4000	0.63	6349	N ₂	N

Figure 4.2.1 presents the AFM micrographs of the deposited GaP films for (a) run A and (b) run B. It can be seen that in both cases GaP grew as widely spaced 3D islands. A continuous film was not formed. The characteristic length of the sizes and spacings of the islands are both of the order of microns. The same flow conditions at the higher temperature result in a higher density of smaller islands. The higher V/III ratio of run C also resulted in more closely spaced islands, but the 3D growth mode is retained.

Figure 4.2.2 presents the RI at 2.64 eV for run A, which is done with repetitive short exposures to TMG. With each exposure, the intensity decreases rapidly. Meanwhile, the $\langle\epsilon\rangle$ data show no change, continuing to exhibit the spectral dependence of the bare substrate. Since the f number of the polarimeter is about 100, this is consistent with the fact that the deposited 3D GaP islands have both sizes and spacings much larger than λ . They therefore scatter light out of the beam, thus reducing the intensity. The apparent value of $\langle\epsilon\rangle$ is

unaffected because the polarization state of the collected light to which the ellipsometer responds is determined by the bare regions between islands. As a result, $\langle \epsilon \rangle$ is characteristic of Si.

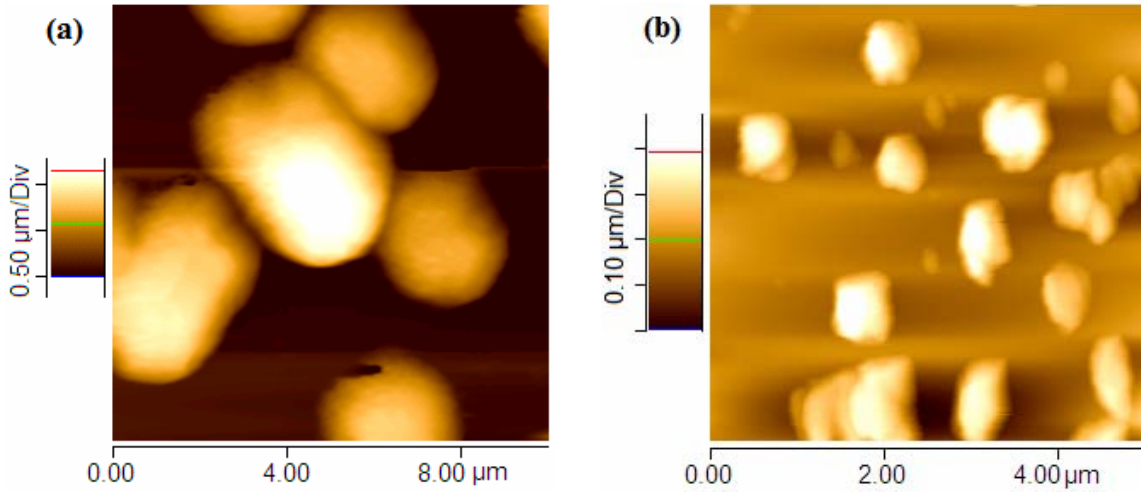


Fig 4.2.1 AFM micrographs of GaP / Si run (a) A and (b) B.

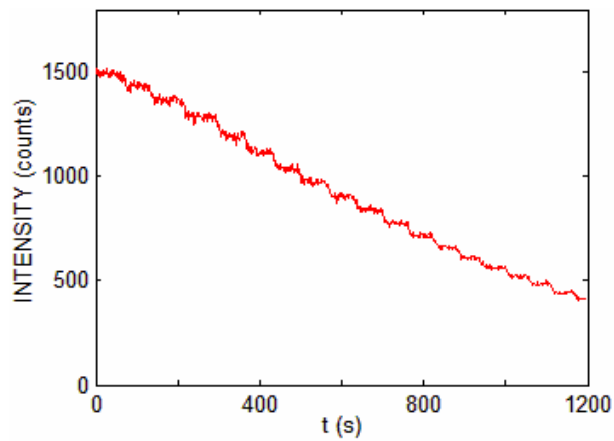


Fig 4.2.2 RI at 2.64 eV for GaP / Si run A.

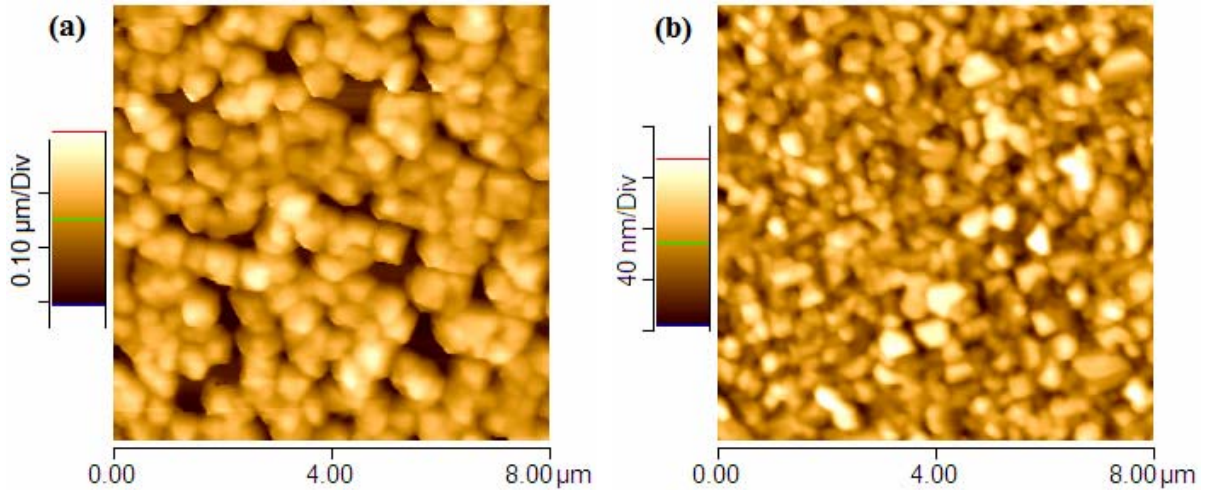


Fig 4.2.3 AFM micrographs for (a) center and (b) edge of GaP / Si run C.

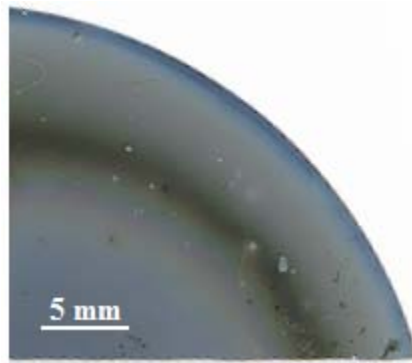


Fig 4.2.4 A piece from GaP / Si run C.

Figure 4.2.3 presents AFM micrographs taken on the (a) center and (b) edge of run C, which show RMS roughnesses of 53.15 and 22.01 nm, respectively. Since a larger V/III ratio of 6349 is used, the nucleation density of run C is higher than that of runs A and B, and the resulting GaP islands have almost coalesced in the central region. Another point of interest is that a quasi continuous rough GaP film is deposited around the edge, consisting of fine polycrystalline grains that have coalesced from the original GaP islands.

Figure 4.2.4 is an Epson Scanner image taken of a corner of run C. A 4 mm wide Si belt appearing as a shiny dark green band separates the edge from the center. The density of

deposited GaP islands gradually increases along both inward and outward directions. The transition in morphology is gradual, so actual boundaries are difficult to define. The edge consists approximately of a 2 mm wide faint belt close to the inner bare Si region, and also an outer 2 mm wide shiny light blue belt representing rough GaP. The central region has a faint blue color, and is bounded by several rings of different colors indicating different morphologies. These differences provide clear evidence that different growth kinetics occur at different regions of the sample. As will be discussed later, the edge growth in particular is due to the back-diffusion of reactive species generated on the susceptor.

Thus to obtain continuous GaP coverage on Si, the nucleation density must be increased in the initial stage. Possible ways are to generate nanoscopic roughness on Si, and to introduce certain impurities that can facilitate surface reactions. These will be the topics of the remaining sections.

4.2.2 Analysis of earlier data of GaP / Si

One of the motivations for the present work was to reproduce a sample of GaP on Si that was done by previous students before the present work was begun. This sample, which in the following we term run # 10, is the best that has been achieved in our OMCVD system so far. However, it has never been analyzed in detail. At the time the SP was operated in a rotating-analyzer configuration, with a data acquisition step of 1.65 s. The growth conditions were those appropriate to the homoepitaxy of bulk material: the sample temperature was 610 °C and the chamber pressure was 60 Torr. N₂ at 10.15 slm was used as the carrier gas, the PH₃ flow was 600 sccm, and the V/III ratio was nominally 10000. However, the growth parameters varied during the initial stage, as will be given below.

Figure 4.2.5 presents the $\langle \epsilon \rangle$ spectrum from 1.5 to 6 eV taken by SE after growth. Also shown are the reference ϵ spectrum of bulk GaP, and the four-phase-model fitting. The

fitting reveals that the bulk layer is ~ 247.76 nm thick and approximately 100% GaP. The top layer is 0.17 nm thick and 50% GaP. Therefore, the crystalline quality appears to be very good.

Figure 4.2.6 presents AFM micrographs of (a) 8 μm and (b) 2 μm wide regions taken after growth. The film is seen to be very smooth, with RMS roughnesses of 0.96 and 0.83 nm respectively. However, the surface contains many irregularly shaped boundaries, which are probably due to the propagation of anti-phase domains as the edges are too high for biatomic steps.

Figure 4.2.7 presents STEM micrographs taken under Z-contrast mode at magnifications $\times 120\text{K}$ for (a) and (b), $\times 5\text{M}$ for (c), and $\times 8\text{M}$ for (d). The low-magnification micrographs (a) and (b) include the entire film. The GaP layer is seen to be heteroepitaxial on Si, and is free of threading or misfit dislocations, although stacking faults do exist and as noted above probably extend to the surface. The high-resolution micrographs (c) and (d) are taken near the interface of GaP and Si. In the Z-contrast mode the image brightness is proportional to the local atomic-number density. Thus a Ga-P pair ($Z = 46$) appears brighter than a Si-Si pair ($Z = 28$). It can be seen that the brightness does not change suddenly, but that a 2 – 3 nm thick transition region exists at the interface. This transition region has an average atomic number between that of Si and GaP, and is clearly a mixture of the two. This region is probably resulted from the roughening of Si by PH_3 during the high-temperature pretreatment.

The $\langle\epsilon\rangle$ data taken during growth essentially agrees with the STEM results. Figure 4.2.8 presents the variation of the E_1 and E_2 peaks of $\langle\epsilon_i\rangle$ at 3.14 eV and 4.03 eV, respectively, during the PH_3 pretreatment and initial growth of GaP on Si, (a) for steps 900 – 2000, and (b) and (c) of enlarged views for steps 900 to 1130 and 1250 to 1480, respectively. The growth conditions are as follows:

- (1) At step 947, $T = 850$ °C and PH_3 is turned on at flow rate of 800 sccm. PH_3 flow is

reduced to 400 sccm at step 1055.

- (2) From steps 1143 to 1244, T is gradually reduced from 850 °C to the growth temperature of 610 °C. At step 1275, the PH₃ flow is increased from 400 sccm to 800 sccm.
- (3) At step 1286, the TMG is turned on with 2 sccm N₂ input carrier gas. The TMG flow rate is nominally 0.06 sccm.
- (4) At step 1721, an inadvertent burst of TMG occurs, and the PH₃ flow changes from 800 to 600 sccm.

Figure 4.2.8 (b) shows that the E₂ peak drops immediately upon the introduction of 800 sccm PH₃ at 4.38 Torr partial pressure at step 947, and continues to decrease gradually until step 1055. Meanwhile, the E₁ peak shows almost no change. This indicates that the Si substrate is being roughened. It is known that PH₃ at this pressure and temperature etches the Si surface on the atomic scale, and a Si-P compound may also be formed. As a result, once TMG is introduced, GaP can readily nucleate due both to the presence of this compound and the rough surface morphology. Again, the results are consistent with the observation of a transition layer with apparent atomic-scale intermixing as revealed by the STEM micrographs.

The previous studies of the reaction of PH₃ with Si in the literature have mostly been done in UHV, with PH₃ partial pressures in the range of 10⁻⁹ to 10⁻⁷ Torr. However, Hannappel et al. [105] have studied the annealing of (001) Si in AsH₃ and PH₃ under typical OMCVD conditions. The (001) Si surface was found to exhibit a rough morphology with peak-to-valley heights of approximately 3 nm under 0.83 Torr PH₃ at 875°C for 10 min, and the formation of a Si-P compound has been indicated from low-energy electron diffraction (LEED) patterns. This study agrees well with our findings. Also Wright et al. [26] have observed interface mixing for the MBE growth of GaP on Si, where the 92 eV Si signals in Auger electron spectroscopy drop exponentially with characteristic lengths of 5 nm for (100)

and 0.95 nm for (211) directions. These are both larger than the escape length of 0.69 nm for 92 eV electrons. Wright et al. explain this as being due to the effects of Si uptake and interface reconstruction driven by the need to reduce charge buildup at the interface. The effect is stronger for the (100) than the (211) orientation.

Figure 4.2.8 (c) shows that when TMG is turned on at step 1286, growth is very slow for the first 170 steps (~ 0.002 nm/step), but speeds up at 1450, as seen from the rapid decrease of both E_1 and E_2 peaks. We attribute this to an unstable reduced flow of TMG when it was first introduced into the growth chamber.

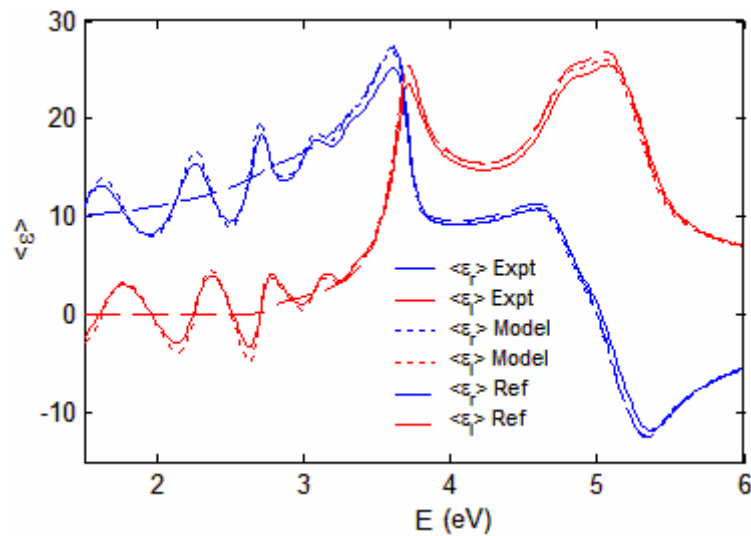


Fig 4.2.5 $\langle \epsilon_r \rangle$ from 1.5 to 6 eV for GaP / Si run # 10.

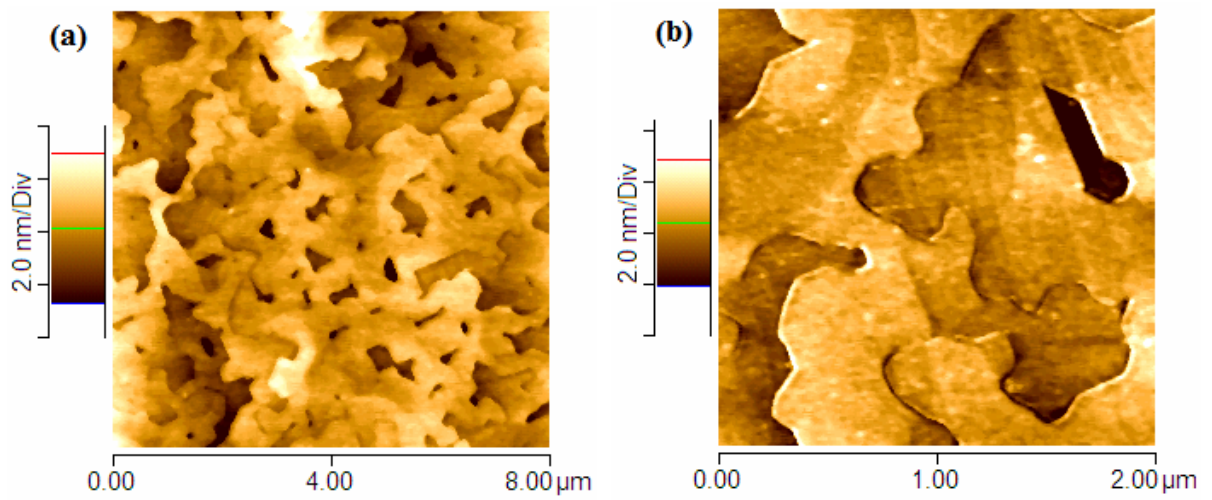


Fig 4.2.6 AFM micrographs at (a) 8 μm and (b) 2 μm for GaP / Si run # 10.

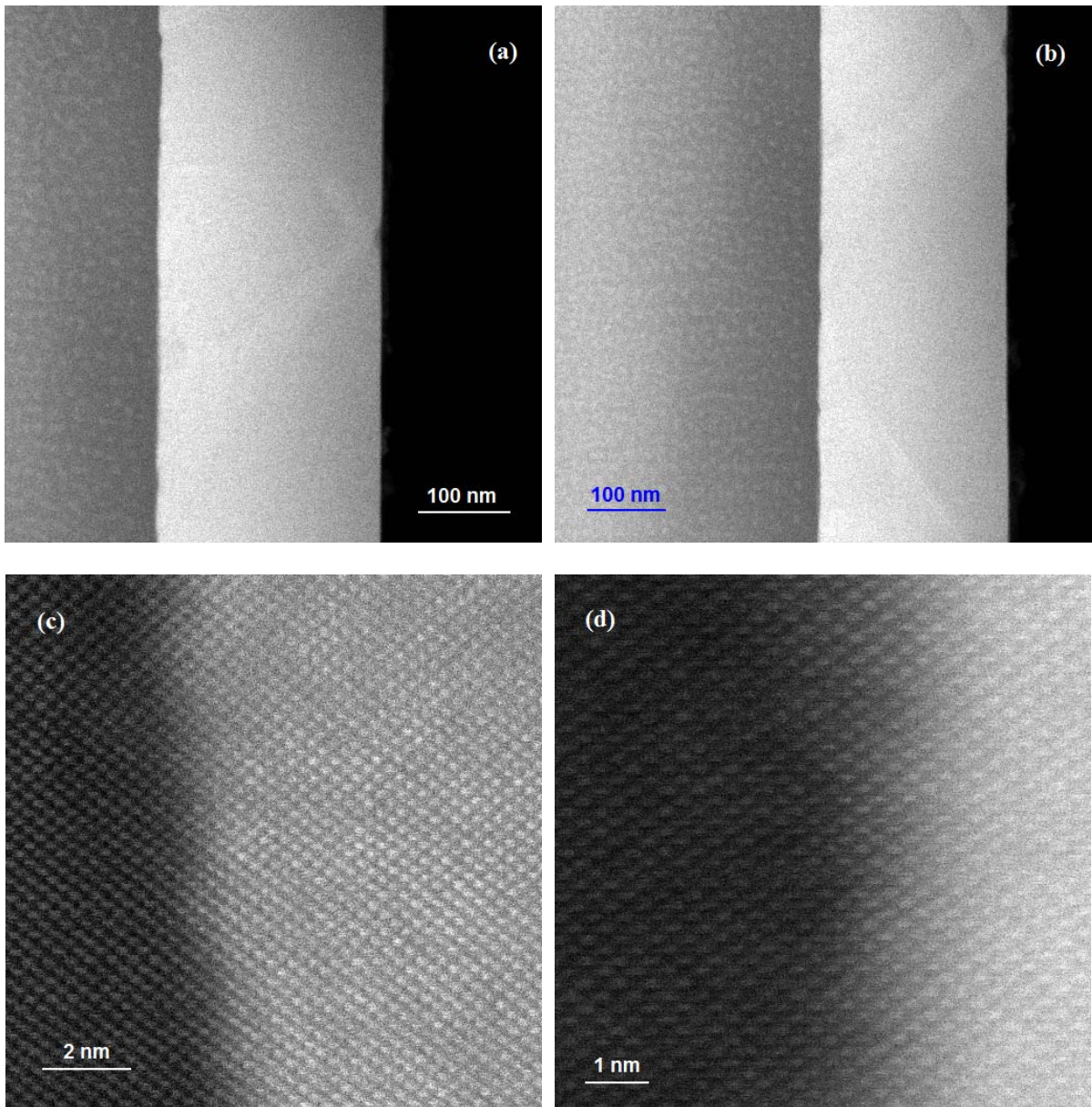


Fig 4.2.7 STEM micrographs for GaP / Si run # 10 in the Z-contrast mode. The magnifications are $\times 120\text{K}$ for (a) and (b), $\times 5\text{M}$ for (c), and $\times 8\text{M}$ for (d).

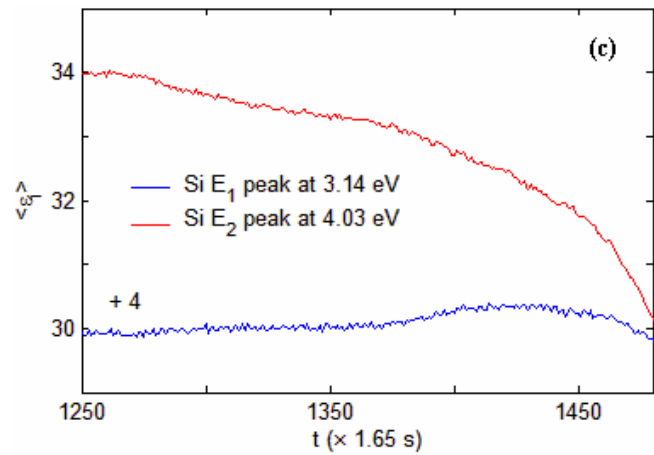
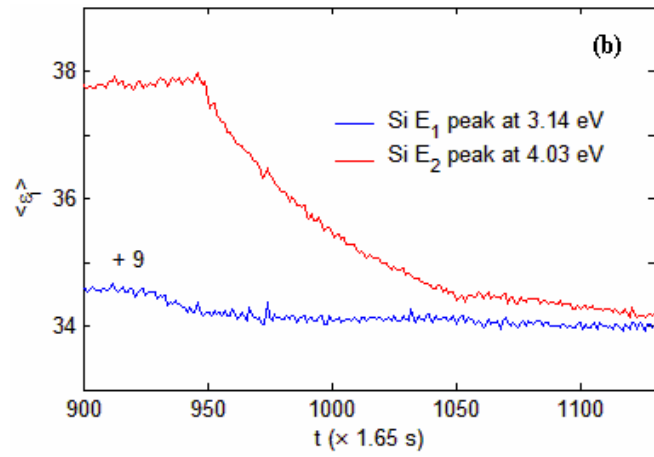
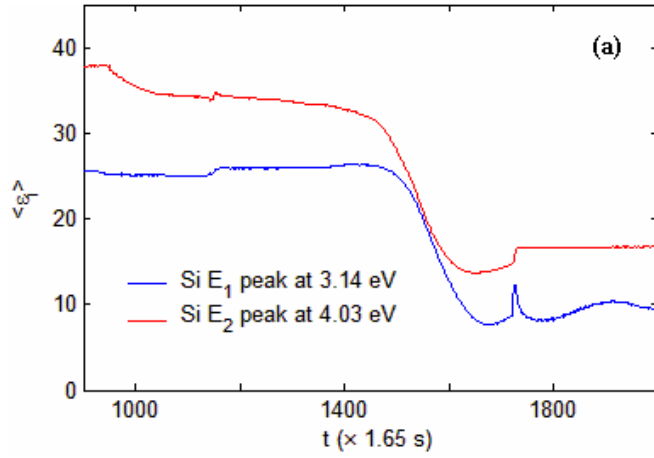


Fig 4.2.8 Variation of the E_1 (3.14 eV) and E_2 (4.03 eV) peaks of $\langle \epsilon_i \rangle$ for Si during the PH_3 pretreatment and growth of GaP in run # 10. Here (a) shows the data for steps 900 to 2000, and (b) and (c) enlarged views for 900 to 1130 and 1250 to 1480, respectively.

Figure 4.2.9 presents the change of $\langle \epsilon \rangle$ spectra from 1.7 to 5.2 eV during steps 1481 – 1661, in 20-step intervals (33 s). They are shifted by $5n$ ($n = 0, 1 \dots 9$) from 0 for clarity. The GaP structure, especially the E_2 peak at 4.75 eV, begins to develop after 60 steps. However, there is no evidence of any interference effects below 3 eV, indicating that the initial GaP layer is not uniform and/or the interface is not sharp. This is consistent with the STEM results. After the TMG burst the uniformity and the crystalline quality improve, although irregular domains may persist.

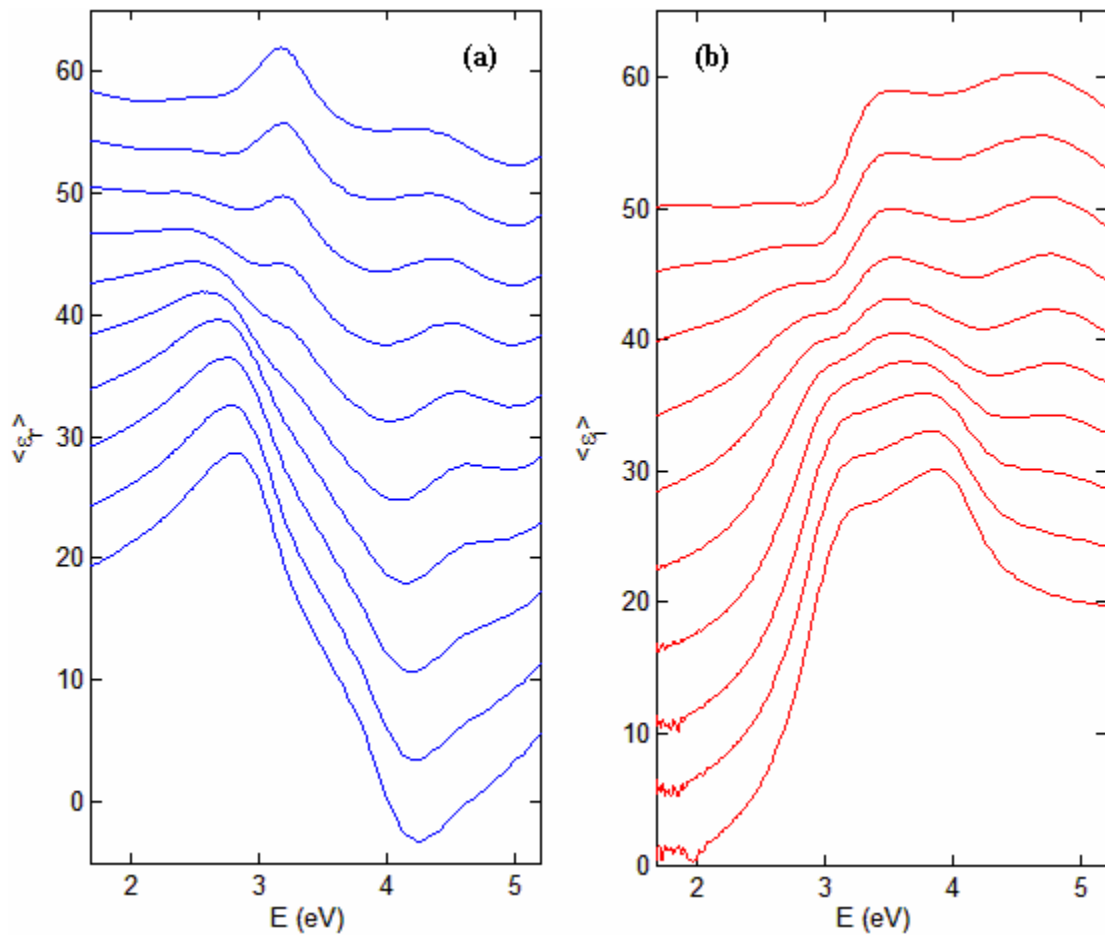


Fig 4.2.9 (a) $\langle \epsilon_i \rangle$ and (b) $\langle \epsilon_i \rangle$ from 1.7 to 5.2 eV during the growth steps 1481 to 1661 for GaP / Si run # 10. The spectra are shown for 20-step intervals (33 s) and are shifted by $5n$ ($n = 0, 1 \dots 9$).

Figure 4.4.10 presents RI and (b) $\langle \varepsilon \rangle$ data at 2.91 eV for the entire growth process. Growth during the TMG burst from steps 1721 to 1743 deviates from the normal spiral, which means that it does not follow a layer-by-layer mode as in the case of similar growth on GaAs. Figure 4.4.11 presents similar data but for the initial stage together with least-square model fittings for steps 1477 – 1542. One distinctive feature is that the growth proceeds as intermixing of GaP with Si, which is also consistent with the STEM results. The extracted growth rate and compositions are listed in Table 4.2.2.

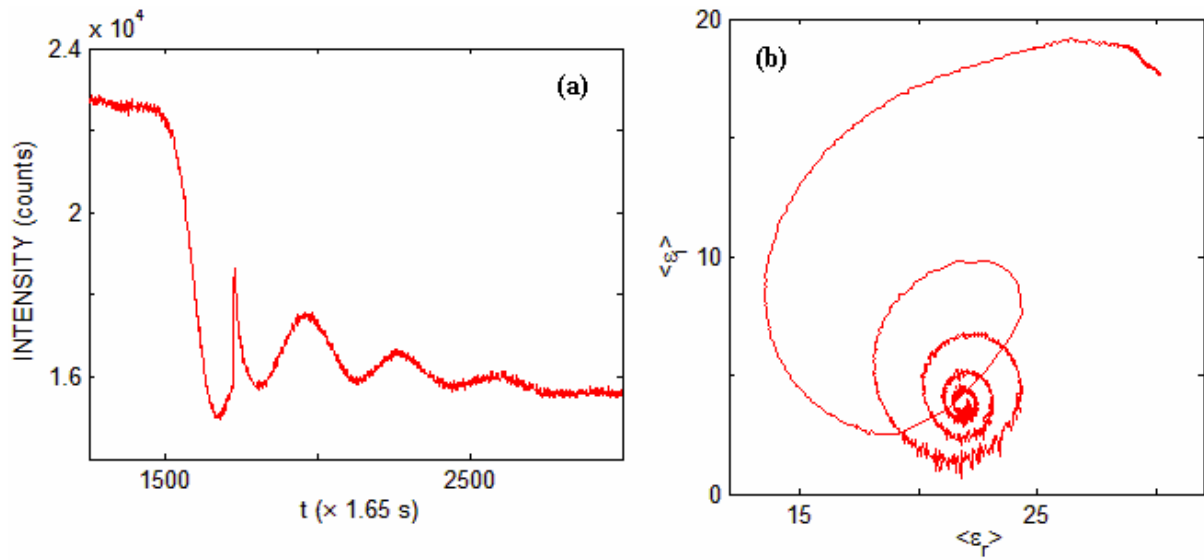


Fig 4.2.10 (a) RI and (b) $\langle \varepsilon \rangle$ data at 2.91 eV during growth of GaP / Si run # 10.

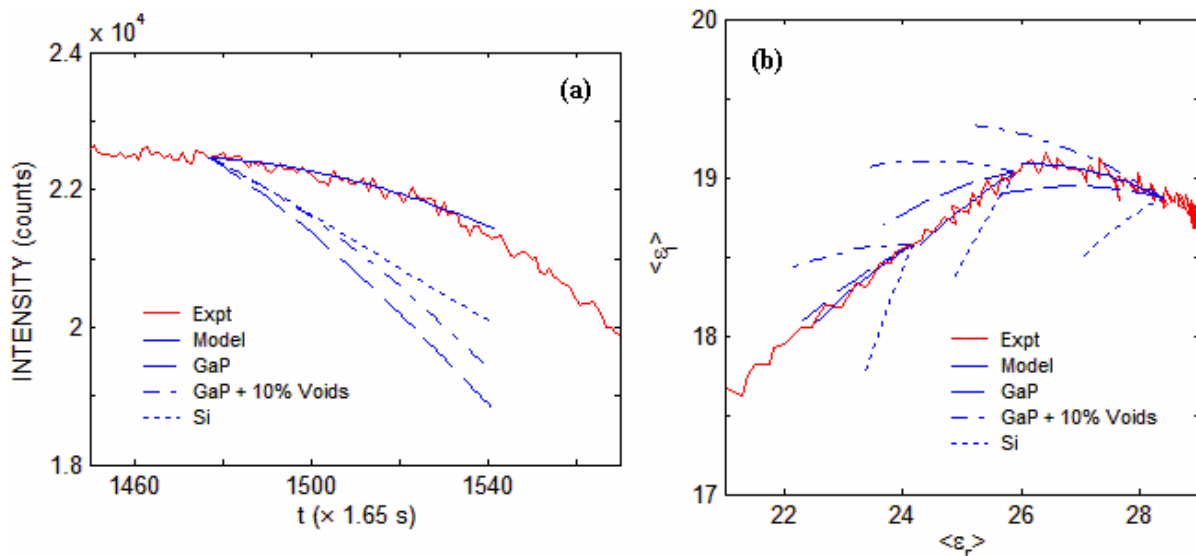


Fig 4.2.11 (a) RI and (b) $\langle \epsilon \rangle$ data at 2.91 eV along with model fittings for the initial stage of GaP / Si run # 10.

Table 4.2.2 Initial stage growth parameters for GaP / Si run # 10 (1 step = 1.65 s).

Data	Duration (step)	Growth Rate (nm/s)	GaP (%)	Si (%)	Voids (%)
RI	1477 - 1542	0.11 (0.01)	25.6 (2.9)	35.4	39.0
$\langle \epsilon \rangle$	1477 - 1510	0.03 (0.001)	18.0 (1.0)	72.1	9.9
	1510 - 1530	0.05 (0.001)	39.2 (0.7)	58.8	2.0
	1530 - 1542	0.07 (0.002)	68.2 (0.9)	29.2	2.6

4.3 GaP heteroepitaxy on nanoscopically roughened (001) Si

4.3.1 Growth and characterization of GaP / nrSi (1:1:1) and (1:3:5)

Several representative deposits of GaP / nrSi are shown in this section, with growth conditions listed in Table 4.3.1. The substrates are p-type (001) Si wafers that were etched

in solutions of either HF:HNO₃:H₂O = 1:1:1 for 30 s, or HF:HNO₃:H₂O = 1:3:5 for 1 min. AFM revealed that the RMS roughness is ~ 7 nm for nrSi (1:1:1) and ~ 1.5 nm for nrSi (1:3:5). The lateral scale is on the order of 50 nm, although smaller features may exist since the lateral resolution of AFM is limited by the radius of the probe, which is larger than 20 nm in our case. As discussed in Chapter 3, prolonged etching (> 4 min) in a HF:HNO₃:H₂O = 1:3:5 solution generates a porous Si layer consisting of compounds of various species including H, O, Si, and possibly also F and N. Although porous Si would in principle be the ultimate nanoscopically rough surface, we found that it could not be used for GaP heteroepitaxy, since the structure and $\langle \epsilon \rangle$ changed upon heating, probably due to dissociation.

Table 4.3.1 Growth conditions for representative GaP / nrSi (1:1:1) and (1:3:5) runs.

Run #	Substrate etching	T (°C)	PH ₃ (sccm)	TMG (sccm)	V/III	Carrier Gas	Rot.
A	HF:HNO ₃ :H ₂ O = 1:1:1, 30 s	600	2500	0.91	2747	N ₂	N
B	HF:HNO ₃ :H ₂ O = 1:3:5, 1 min	610	5000	1.88	2659	H ₂	N
C	HF:HNO ₃ :H ₂ O = 1:3:5, 1 min	610	5000	0.63	7937	H ₂	N

Figure 4.3.1 presents the $\langle \epsilon \rangle$ spectrum from 1.5 to 6 eV measured after deposition for the (a) center and (b) edge regions of GaP / nrSi (1:1:1) run # A, with the top GaP oxide removed with a solution of 10% NH₄OH. The GaP features can be identified, but the low $\langle \epsilon \rangle$ E₂ peaks and smaller oscillation patterns indicate inferior film quality, which may also be a result of polycrystallinity. Four-phase-model least-square fittings confirms this, showing that the bulk contains ~ 30% voids, and the edge is ~ 50 nm thicker than the center.

Figure 4.3.2 (a) and (b) present the AFM micrographs taken on the center and edge of run # A respectively. The RMS roughnesses are 10.85 and 12.69 nm for the two regions.

The surface is seen to consist of fine polycrystalline grains of 50 to 200 nm diameters. Also, the approximate morphology and the appearance of recessed pits are very similar to that of the original nrSi, indicating conformal deposition.

Figure 4.3.3 (a) and (b) present the AFM micrographs taken near the center region of GaP / nrSi (1:3:5) runs # B and C respectively. These films consist of only GaP islands. With a larger V/III ratio used, the film of run #B exhibits larger island density and smaller island size.

We assume that the reason that a continuous GaP layer can be grown on nrSi (1:1:1) but not nrSi (1:3:5) is due to the different density of kink sites available, which is larger in the former than the latter. This will be discussed more fully in Section 4.5.2.

The slow growth rate of 0.21 nm/s leads to thickness evolutions that are relatively small comparing to the characteristic size of the vertical Si roughness features of about 10 nm. Here a recognizably sharp growth front is hard to define. Thus the real-time RI and $\langle \epsilon \rangle$ data for continuous growth cannot be analyzed using a layer-by-layer model. As an alternative, we simply present in Figure 4.3.4 ten $\langle \epsilon \rangle$ spectra from 1.7 to 5.2 eV taken at 30 s intervals from the beginning of growth run # A, shown shifted by $3n$ ($n = 0, 1 \dots 9$) for clarity. The starting spectrum is nrSi. The GaP feature and interference oscillation become obvious after 90 s.

Figure 4.3.5 presents the evolution of $\langle \epsilon_i \rangle$ at 4.84 eV, which corresponds to the E_2 peak of GaP. $\langle \epsilon_i \rangle$ gradually saturates at a value of ~ 8.5 , which is low and indicates porous material. The fact that it saturates indicates that the roughness cannot be eliminated by further deposition. Thus the subsequent homoepitaxial growth results in almost identical surface conditions in the thickness range of our interests. This is consistent with the fact that growth on kink sites by direct incorporation generates similar kink sites, so the surface morphology is preserved.

Several other runs were also done using different V/III ratios and TMG flows, but the

results were very similar. Thus although continuous GaP films could be grown on nrSi (1:1:1) substrates, the layers exhibited high nanoscopic roughness and the crystalline quality was unsatisfactory.

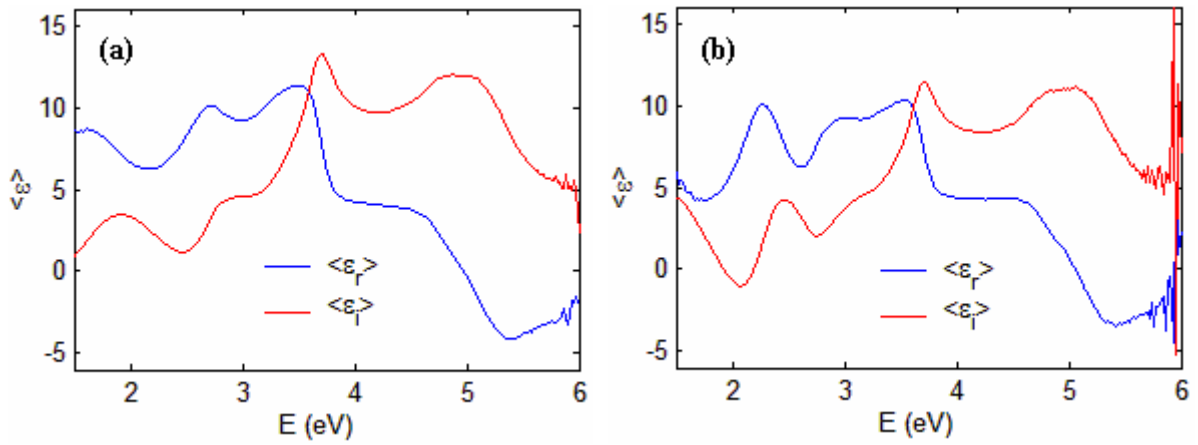


Fig 4.3.1 $\langle \epsilon \rangle$ spectrum from 1.5 to 6 eV for (a) center and (b) edge of GaP/nrSi measured after deposition.

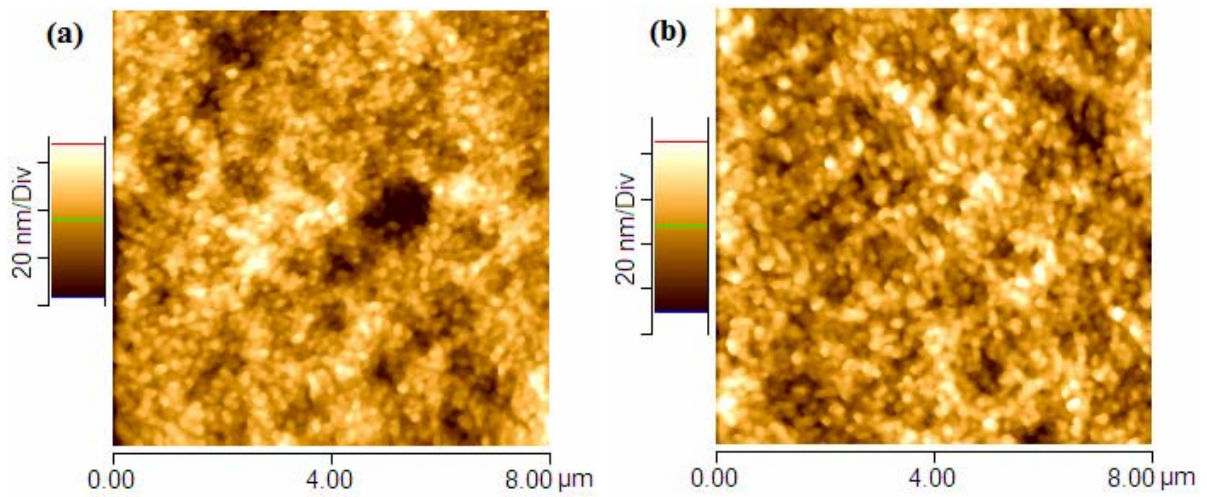


Fig 4.3.2 AFM micrographs of (a) center and (b) edge of GaP/nrSi (1:1:1) run A.

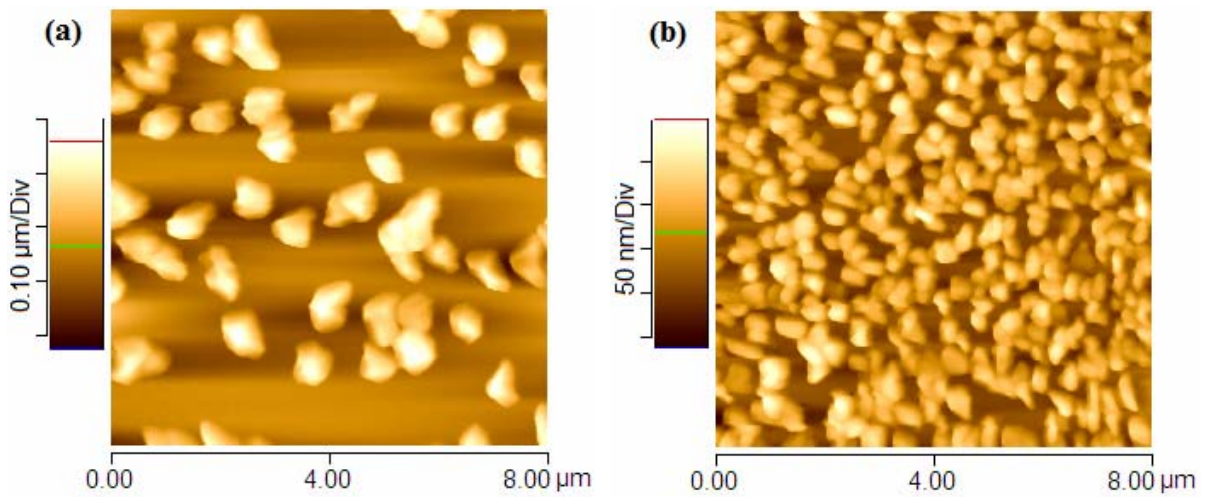


Fig 4.3.3 AFM micrographs of GaP / nrSi (1:3:5) run (a) B and (b) C.

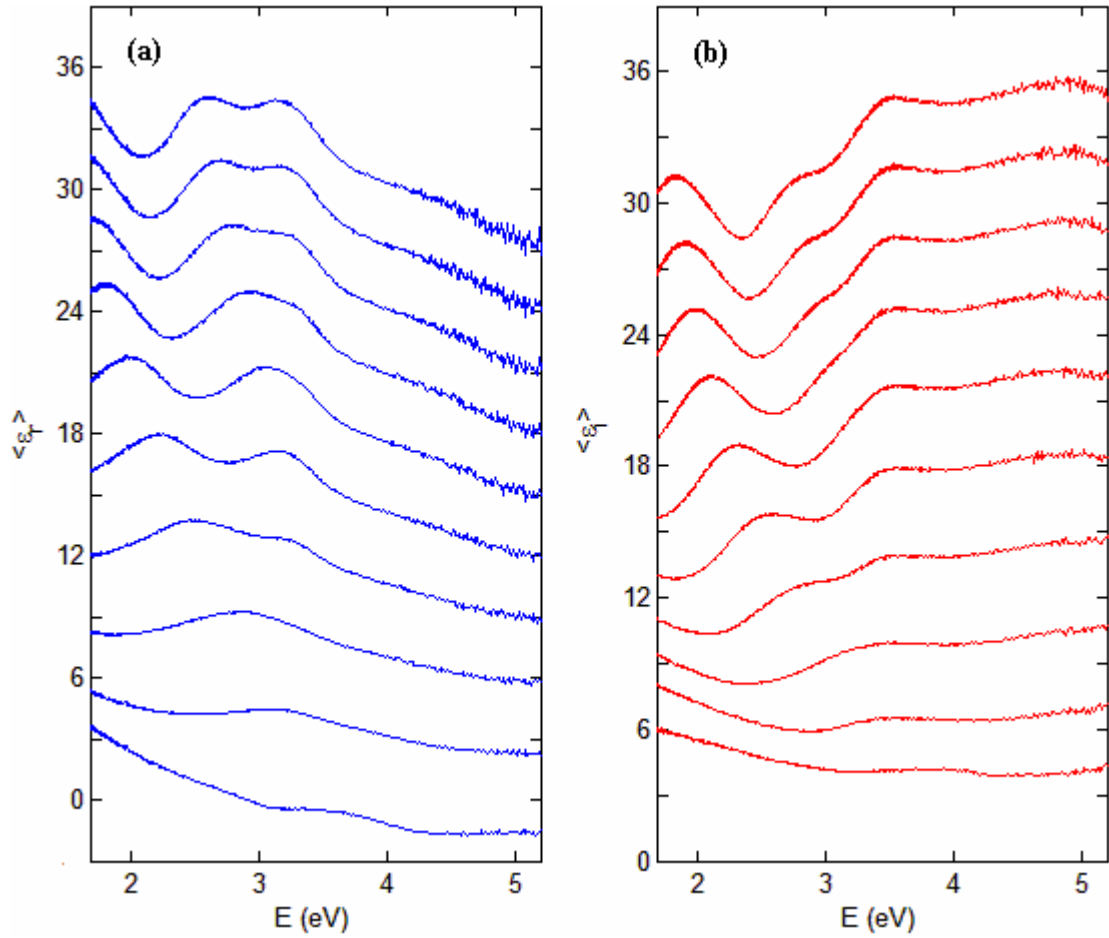


Fig 4.3.4 (a) $\langle \varepsilon_i \rangle$ and (b) $\langle \varepsilon_i \rangle$ from 1.7 to 5.2 eV during growth of GaP/nrSi (1:1:1) run A. The spectra are shown for 30 s intervals and for clarity are shifted by $3n$ ($n = 0, 1 \dots 9$).

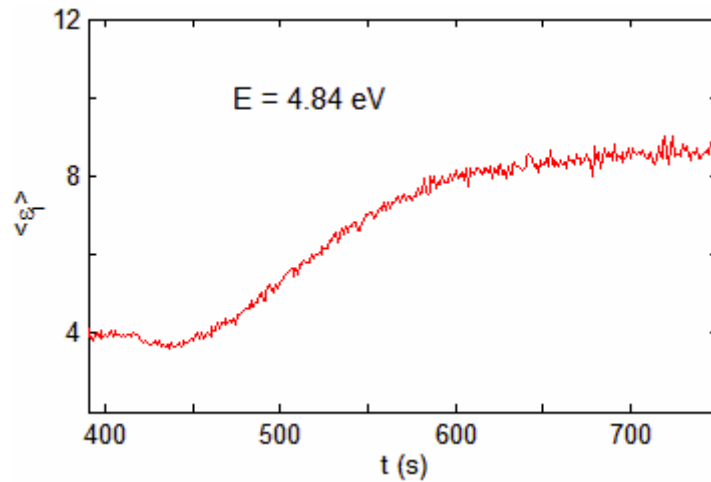


Fig 4.3.5 The change of the GaP E_2 peak of $\langle \varepsilon_i \rangle$ at 4.84 eV during growth of GaP/nrSi (1:1:1) run A.

4.3.2 Lateral thickness variation of GaP / nrSi (1:1:1)

Figure 4.3.6 presents the lateral thickness profile of GaP / nrSi (1:1:1). To extract thicknesses more accurately from $\langle \epsilon \rangle$ in least-squares analysis, a compositionally graded GaP and Si layer is introduced between the substrate and the bulk layer of the conventional four phase model. Once this is done we find that the effective thickness is $T_E = 107.29 + 0.33 e^{x/5.02}$. Here T_E is in nm and x is in mm. The edge is thicker than the center, and the thickness increases exponentially. The form of T_E best describes an inward diffusion process, which is of opposite to the case of outward diffusion as in GaP/GaAs. We will discuss it further in Section 4.5.3.

Figure 4.3.7 presents (a) the calculated concentration change of gas phase P reactive species along the radius $\Delta n = 0.0031 e^{x/5.02}$ (x in mm) which is normalized to the center concentration, and (b) the resulting calculated diffusion current $J = - e^{(x-25.4)/5.02}$ (x in mm), which is normalized to the edge flow. These are obtained from the data of Fig. 4.3.6 assuming a constant thickness of the stagnant layer. These results will be discussed in Section 4.5.3.

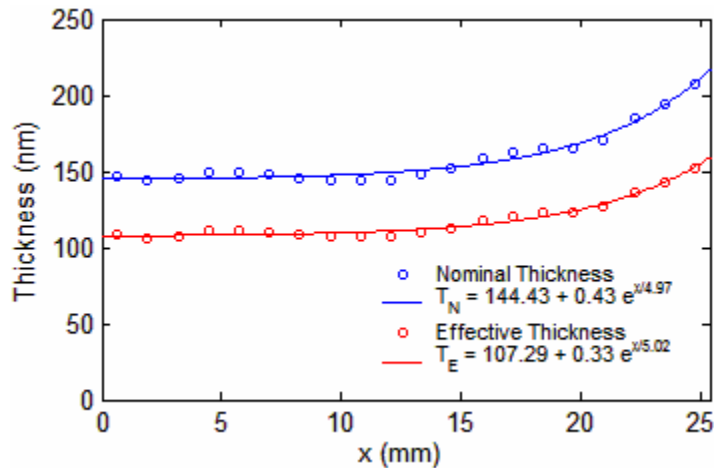


Fig 4.3.6 Thickness profile of GaP / nrSi (1:1:1) run A.

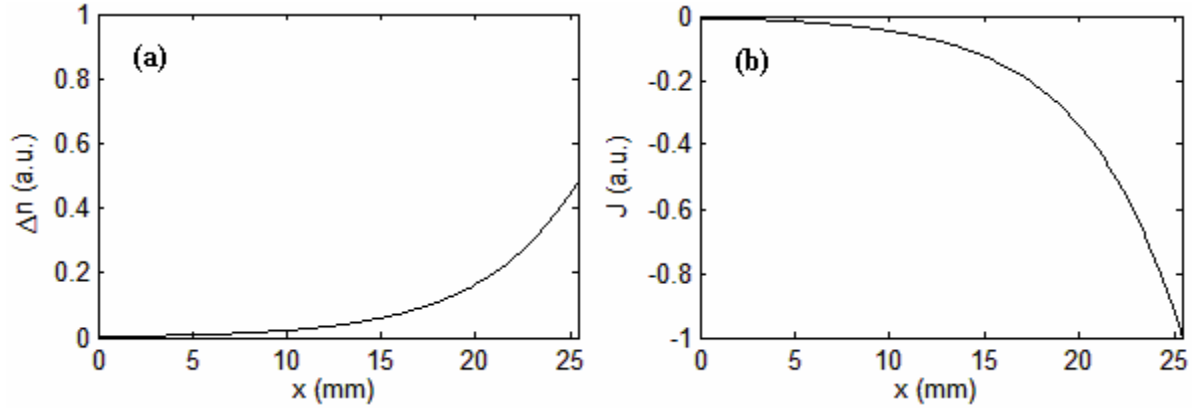


Fig 4.3.7 (a) Calculated concentration change of gas phase reactants along a radius for GaP / nrSi (1:1:1) run A that is required to obtain the observed thickness change, assuming a constant stagnant layer thickness. The scale is normalized to the center concentration. (b) Calculated diffusion current resulted from (a), normalized to the edge flow.

4.3.3 Growth and characterization of GaP / nrSi (1% NH₄F)

Two representative runs grown on another type of roughness are shown here, with growth conditions listed in Table 4.3.3. These nrSi substrates were generated by etching in 1% NH₄F solution at 80 °C, 2 min for run D and 7 min for run E. The RMS roughnesses are 3 and 12 nm, respectively.

Figure 4.3.8 presents the $\langle \epsilon \rangle$ data from 1.5 to 6 eV measured after deposition for the (a) center and (b) edge of GaP / nrSi (1% NH₄F) run D, with the GaP oxide removed with a solution of 10% NH₄OH. The center region exhibits the $\langle \epsilon \rangle$ spectrum of the rough Si resulted from NH₄F etching, and can be modeled using a top layer of 2.91 nm containing 50% Si. There is no evidence of any GaP. The edge-region spectrum shows GaP structure but the quality is low.

Figure 4.3.9 (a) and (b) present AFM micrographs of the center and edge, respectively, of run D. The RMS roughness of the edge is 26.5 nm. In the center region growth is of island type, consisting of widely spaced islands 2 to 3 μm in diameter. In contrast GaP

deposited on the edge is polycrystalline with grains of 50 – 300 nm in diameter. The appearance of two very different types of growth on one substrate under nominally identical conditions shows the importance of edge effects, to be discussed in Section 4.5.3.

Figures 4.3.10 and 4.3.11 present another set of $\langle \epsilon \rangle$ and AFM data but for run E. The $\langle \epsilon \rangle$ spectrum for the center of the film also shows only the rough Si substrate before growth, here exhibiting a roughness of about 25 nm with more than 50% voids. The $\langle \epsilon \rangle$ spectrum of the edge region is that of low-quality GaP. The AFM micrographs reveal the same pattern of island growth in the center and polycrystalline growth in the edge as with the sample run D, with a RMS roughness of 26.1 nm. An additional micrograph, Fig. 4.3.11 (c), is taken on a relatively flat area between islands in the center region, and shows Si with a RMS roughness of 15.8 nm.

Table 4.3.2 Growth conditions for representative GaP / nrSi (1% NH₄F) runs.

Run	Substrate etching	T (°C)	PH ₃ (sccm)	TMG (sccm)	V/III	Carrier Gas	Rot.
D	1% NH ₄ F, 80 °C 2 min	680	800	0.34	2353	N ₂	N
E	1% NH ₄ F, 80 °C 7 min	580	800	0.34	2353	N ₂	N

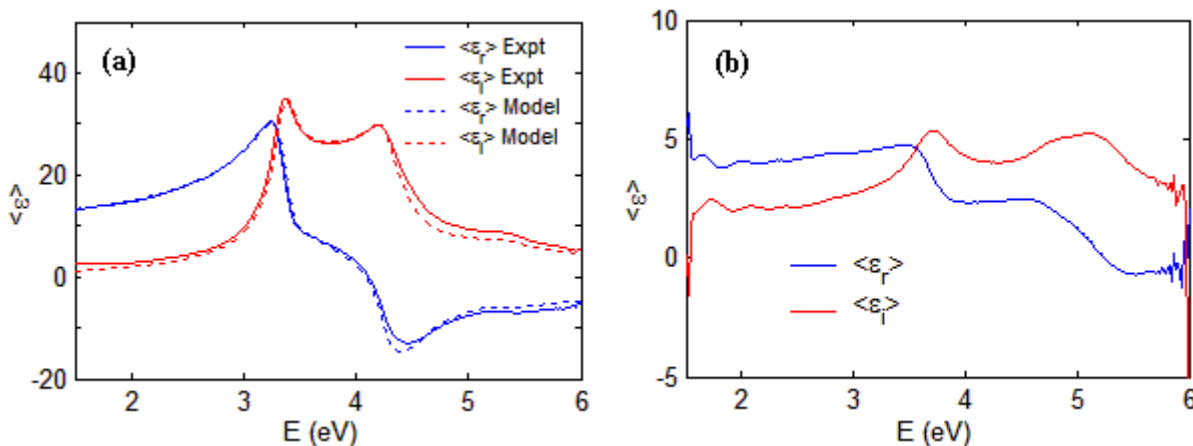


Fig 4.3.8 $\langle \epsilon \rangle$ spectrum from 1.5 to 6 eV for the (a) center and (b) edge regions of GaP / nrSi (1% NH₄F) run D, measured after deposition.

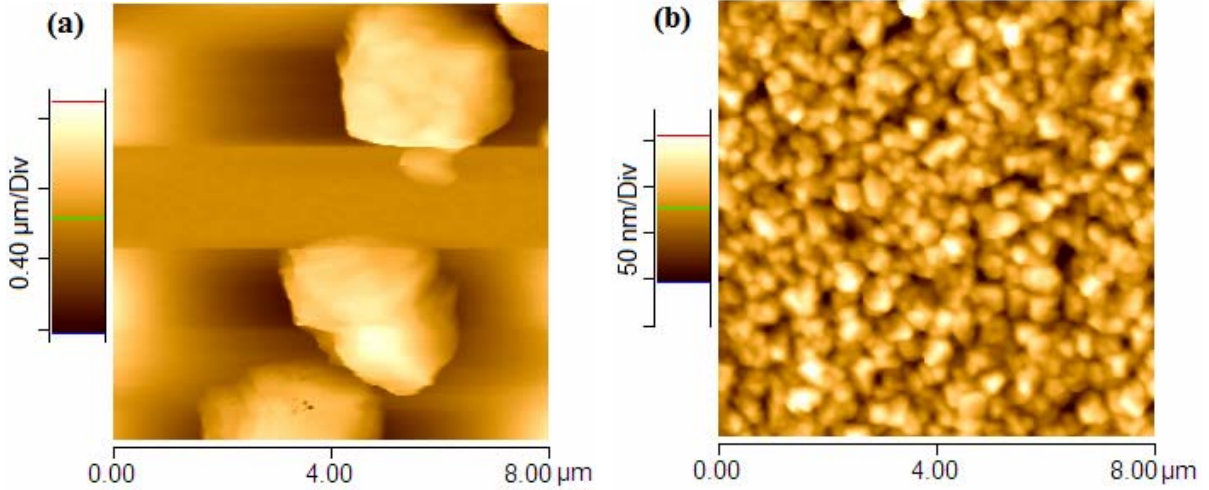


Fig 4.3.9 AFM micrographs of the (a) center and (b) edge regions of GaP / nrSi (1% NH₄F) run D.

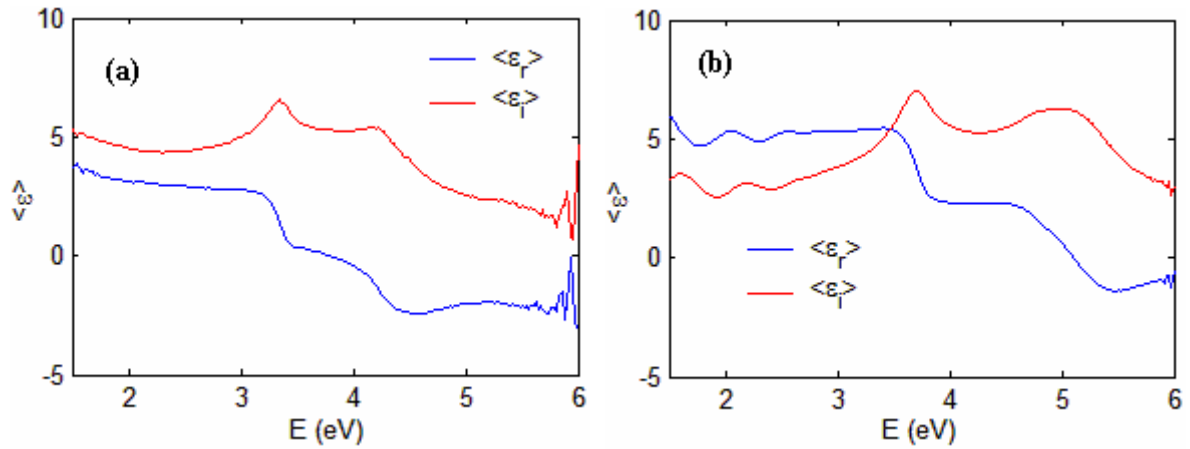


Fig 4.3.10 $\langle \epsilon \rangle$ spectrum from 1.5 to 6 eV for the (a) center and (b) edge regions of GaP / nrSi (1% NH₄F) run E, measured after deposition.

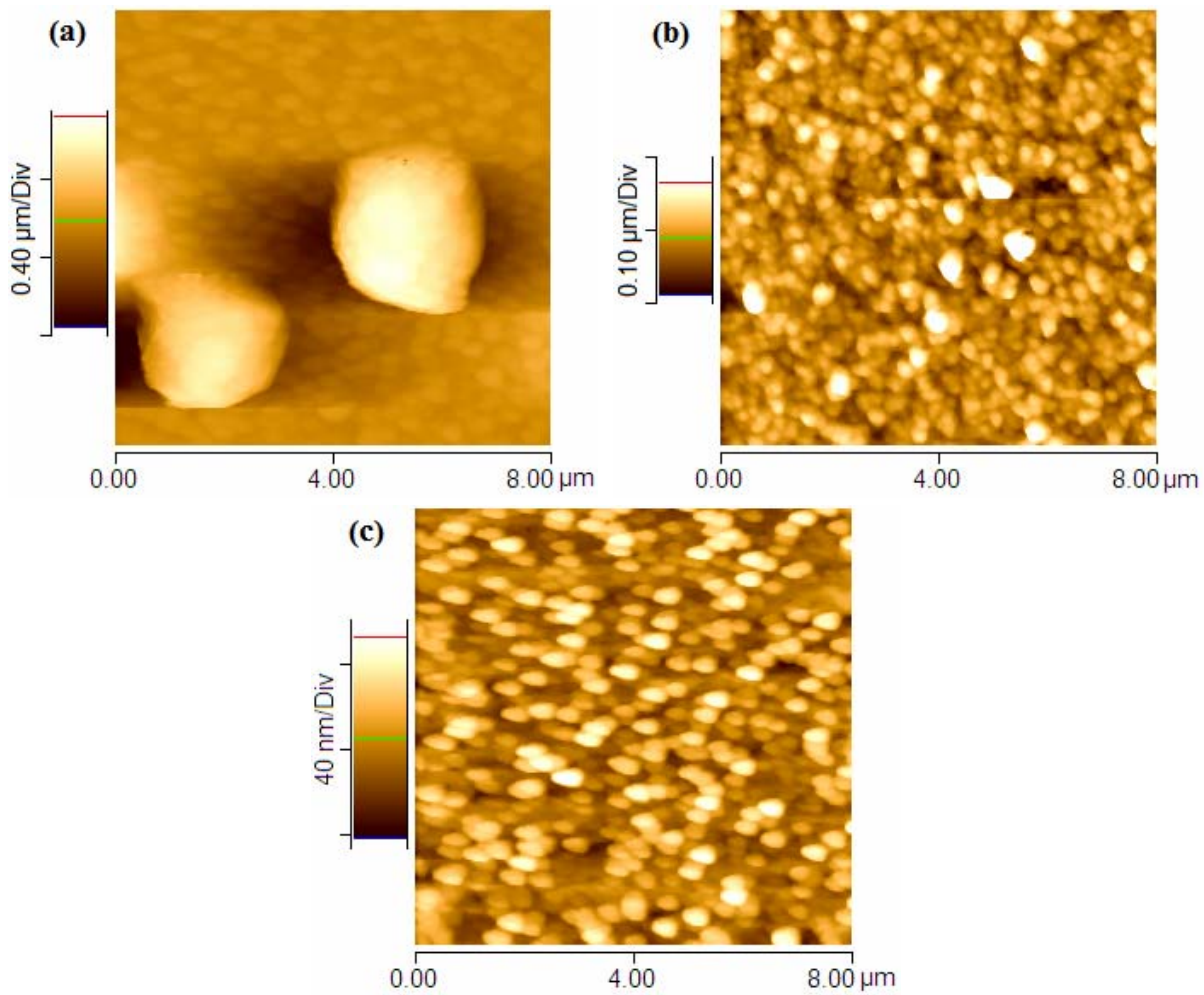


Fig 4.3.11 AFM micrographs of the (a) center, (b) edge, and (c) center between-islands regions of GaP/nrSi (1% NH₄F) run E.

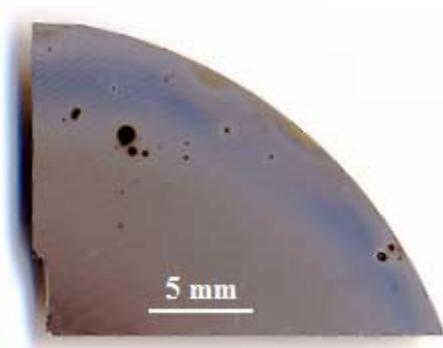


Fig 4.3.12 Photograph of a portion of GaP / nrSi (1% NH₄F) run D.

Figure 4.3.12 is an Epson Scanner image of run D, and shows the distinct contrast between edge and center regions. The blue band is the rough GaP deposited on the edge. The GaP islands deposited in the center appear only as hazy grains on top of the shiny dark green Si substrate. No bare Si regions exist in contrast to the GaP / Si case.

Thus the nrSi substrates generated by 1% NH₄F etching are not effective in suppressing GaP island growth in the center region under a normal V/III ratio of 2353, even though it exhibits a RMS roughness of 12 nm. However, we are able to growth continuous films of GaP on nrSi (1:1:1) substrates even though the RMS roughness is less, ~ 7 nm. The reason for this difference lies in the distinctive patterns of these two kinds of roughness on the atomic scale, as will be discussed in Section 4.5.2.

4.4 GaP heteroepitaxy on thermally oxidized Si

4.4.1 Growth and characterization of GaP / SiO₂

All experiments described in this section were done on Si wafers thermally oxidized *in situ* before GaP growth by first heating up the Si substrates to 800 °C under H₂ flow, then exposing the surface 6 times to 1 psi O₂ in bursts of 2 s each. After 6 exposures the E₂ peak of <ε_i> essentially stabilizes to a value lower than that of E₁, indicating a saturation thickness of 2.5 to 3 nm for SiO₂. The resulting film is very smooth, with typical RMS roughnesses of less than 0.5 nm. Experimental details are presented in Chapter 3.

Table 4.4.1 lists the growth conditions for 6 representative GaP/SiO₂ runs. As before, the growth modes can be distinguished according to different precursor values as normal, PH₃ deficient, TMG pulse, and TMG burst. One additional mode that we employ here is a TMG pulse, a process where TMG is first accumulated inside a valved-off reservoir line, and is then injected into the growth chamber through a pressure difference between the reservoir

line and the chamber. The TMG pulse delivered in this way is gentler and better controlled than TMG bursts achieved by changing the PC directly.

Figure 4.4.1 presents $\langle \epsilon \rangle$ spectra from 1.5 to 6 eV with GaP oxides removed with a solution of 10% NH_4OH . Figure 4.4.2 shows AFM micrographs taken near the center region. The crystalline quality was too poor to allow $\langle \epsilon \rangle$ to be analyzed using conventional four-phase models. We were able to achieve some success by inserting a compositionally graded GaP buffer layer between the substrate and the innermost GaP region. This reduces the sharp back-reflection that otherwise occur at a dielectrically abrupt interface. Instead of listing four phase model parameters obtained from least-squares fittings as before, we simply present the oscillator strength (OS) and E_2 peak height of $\langle \epsilon_i \rangle$ to allow a quick comparison among films. The OS is the largest peak-to-valley distance of the oscillations in the transparent region, and it provides an intuitive assessment of bulk GaP concentrations. The E_2 peak at 5.05 eV is a direct measure of the GaP surface quality. These two parameters along with the RMS roughness measured by AFM are summarized in Table 4.4.2.

As seen from Figure 4.4.1, for GaP layers grown on SiO_2 the heights of the characteristic peaks are much reduced relative to the ϵ spectrum of a GaP single crystal, and the bulk contains about 10 to 50% voids. The AFM results in Figure 4.4.2 also reveal that the epilayers are mainly polycrystalline, with grain sizes ranging from 200 to 700 nm in diameter. The polycrystalline quality as well as the grain size and morphology are established by growth conditions, mainly by TMG flow and the V/III ratio. Irregular deviations such as larger TMG flows and/or lower V/III ratios would deteriorate growth quality, which results in smaller OS, larger grain sizes and larger RMS roughnesses.

The effect of different growth conditions can also be seen from real-time analysis. Figures 4.4.3 – 4.4.6 present (a) RI and (b) $\langle \epsilon \rangle$ data at 2.64 eV together with least-squares model fitting for the initial stages of runs A, B, C, and E. The extracted fitting parameters are summarized in Table 4.4.2, which show among other results that the growth rates are

roughly proportional to TMG flow, and that the GaP density is roughly proportional to the V/III ratio.

Among the 6 representative runs, run A has the best film quality. It was grown under normal conditions with constant PH_3 and TMG flows of 1700 and 0.52 sccm, respectively. Thus the V/III was about 3300. The resulting OS of 8.8 is the largest, and the RMS roughness of 3.5 nm is also the smallest. Growth for the initial 42 s consists of 38% GaP being deposited at a rate of 0.28 nm/s. Afterward, GaP starts filling in the voids, with the bulk GaP concentration gradually increasing to an average of 90%, as shown by $\langle \varepsilon \rangle$ analysis. The completed film has a shiny dark green appearance and is mirror-smooth to the eye.

Growth conditions for runs B – F were chosen using run A as a reference. Run B is also normal growth, but with a higher initial TMG flow of 1.5 sccm and lower V/III ratio of 1130. For the first 10 s the growth rate is 0.39 nm/s, and the epilayer consists of 53% GaP. The OS shrinks to 1.9 and the RMS roughness increases to 19.3 nm.

Run C was done at a reduced TMG flow of 0.25 sccm and a higher V/III ratio of 6800. The growth rate is 0.25 nm/s for the initial 50 s, and the epilayer contains 72.8% GaP, which is better than run A. However, afterward the PH_3 flow changes from 1700 sccm to a residual level of 100 sccm, so the subsequent growth is relatively PH_3 deficient with a V/III of only 400. As a result the final OS is 2.4 and the RMS roughness is 11.7 nm.

Run D starts with 10 TMG pulses and then reverts to continuous growth. As described earlier the reservoir line is first filled with TMG. When the pressure inside reaches 20 Torr the valve is opened to deliver a TMG pulse into the chamber, which is at a pressure of 4 Torr. The resulting TMG flow is about 1.5 times the usual value of 0.52 sccm. The quality of run D is only slightly less than that of run A, with an OS of 5.7 and an RMS roughness of 6.2 nm. This indicates that growth under these particular TMG pulses at least, is fairly close to equilibrium.

Runs E and F both were done with 6 TMG bursts before changing to continuous growth,

with each burst generated by changing the PC from 600 to 200 Torr, thereby delivering a TMG flow during the burst that is 5 to 10 times higher than usual. The first burst of run E lasted 15 s, and the resulting film contained 45% GaP at 1.3 nm/s for the initial 8 s, and 57% GaP at 0.9 nm/s for the rest. The OS and RMS roughness are 3.1 and 3.2, and 28 nm vs. 26 nm, for runs E and F respectively.

Thus it is concluded that GaP films can be grown on thermally generated SiO₂, which is perhaps not surprising in that SiO₂ is similar to GaAs in the sense that both are polar materials. However, being amorphous SiO₂ cannot provide a reference frame where group III and V are incorporated selectively into two separate sublattices. Thus the resulting GaP layer is polycrystalline. To obtain the best quality material, it is necessary to use a low TMG flow with a high V/III ratio.

Table 4.4.1 Growth conditions for representative GaP/SiO₂ depositions.

Run	Type	T (°C)	PH ₃ (sccm)	TMG (sccm)	V/III	Carrier Gas	Rot.
A	Normal	570	1700	0.52	3269	H ₂	Y
B	Normal	570	1700	1.5 / 0.52	1133 / 3269	H ₂	Y
C	PH ₃ Deficient	570	1700 / 100	0.25	6800 / 400	H ₂	Y
D	TMG Pulse	610	1500	≥ 0.52	≤ 2885	H ₂	Y
E	TMG Burst	600	3200	>> / 0.52	<< / 6154	H ₂	Y
F	TMG Burst	600	3200	>> / 0.52	<< / 6154	N ₂	Y

Table 4.4.2 Characterization parameters for the final films and the initial stages determined by least-squares fitting for representative GaP/GaAs depositions.

Run	Final Film			Initial Stage		
	Oscillation Strength	E ₂ Peak Height	AFM RMS Roughness (nm)	Duration (s)	Growth Rate (nm/s)	GaP Comp. (%)
A	8.8	9.4	3.5	42 (22 – 64)	0.28 (0.01)	38 (4)
B	1.9	8.1	19	10 (185 – 195)	0.39 (0.03)	53 (7)
C	2.4	6.3	12	50 (251 – 301)	0.25 (0.002)	73 (0.4)
D	5.7	10.2	6.2	-	-	-
E	3.1	10.2	28	8 (407 – 415)	1.30 (0.07)	45 (5)
				7 (415 – 422)	0.86 (0.10)	57 (5)
F	3.2	5.9	26	-	-	-

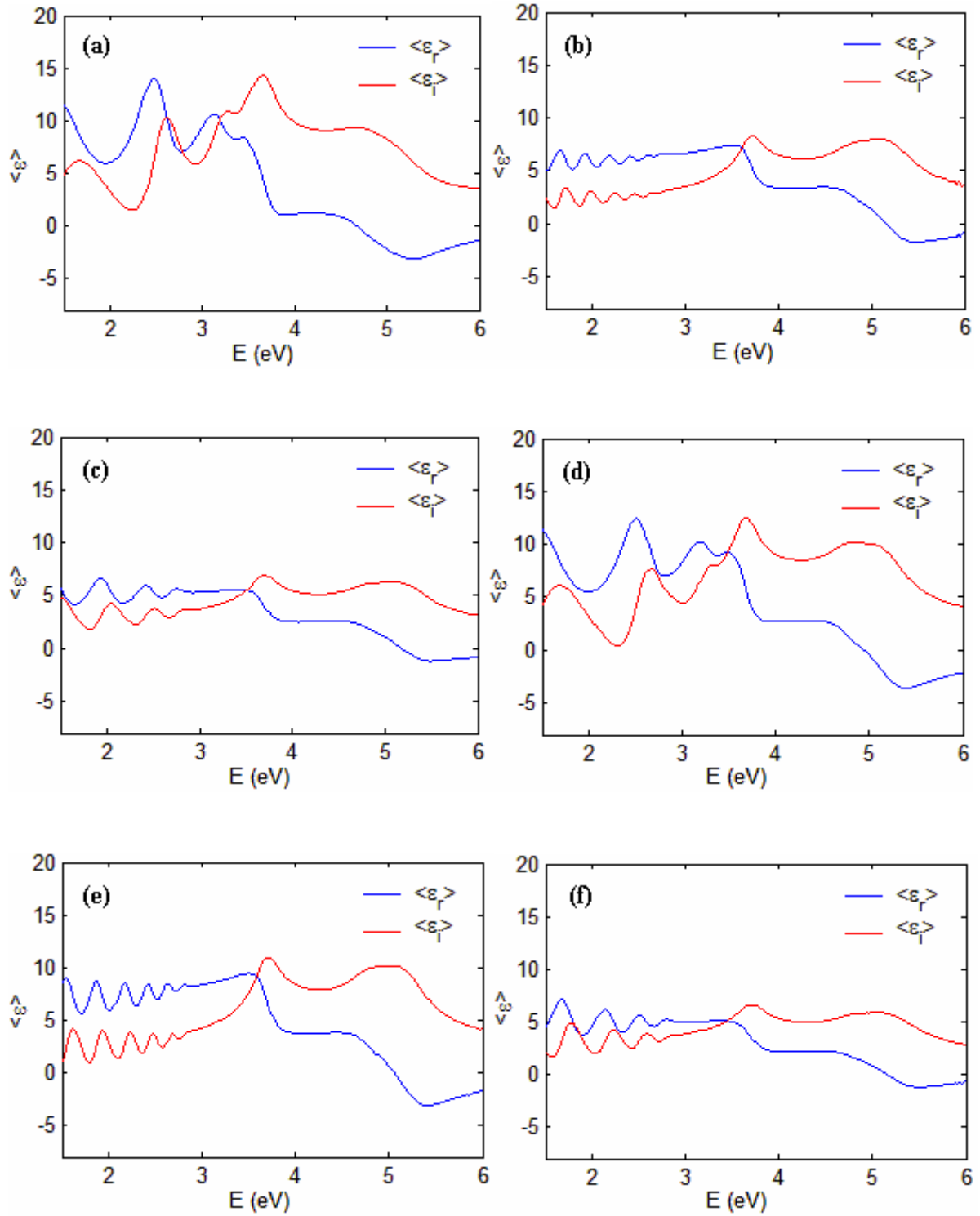


Fig 4.4.1 $\langle \epsilon \rangle$ spectra from 1.5 to 6 eV for GaP/SiO₂ runs A - F.

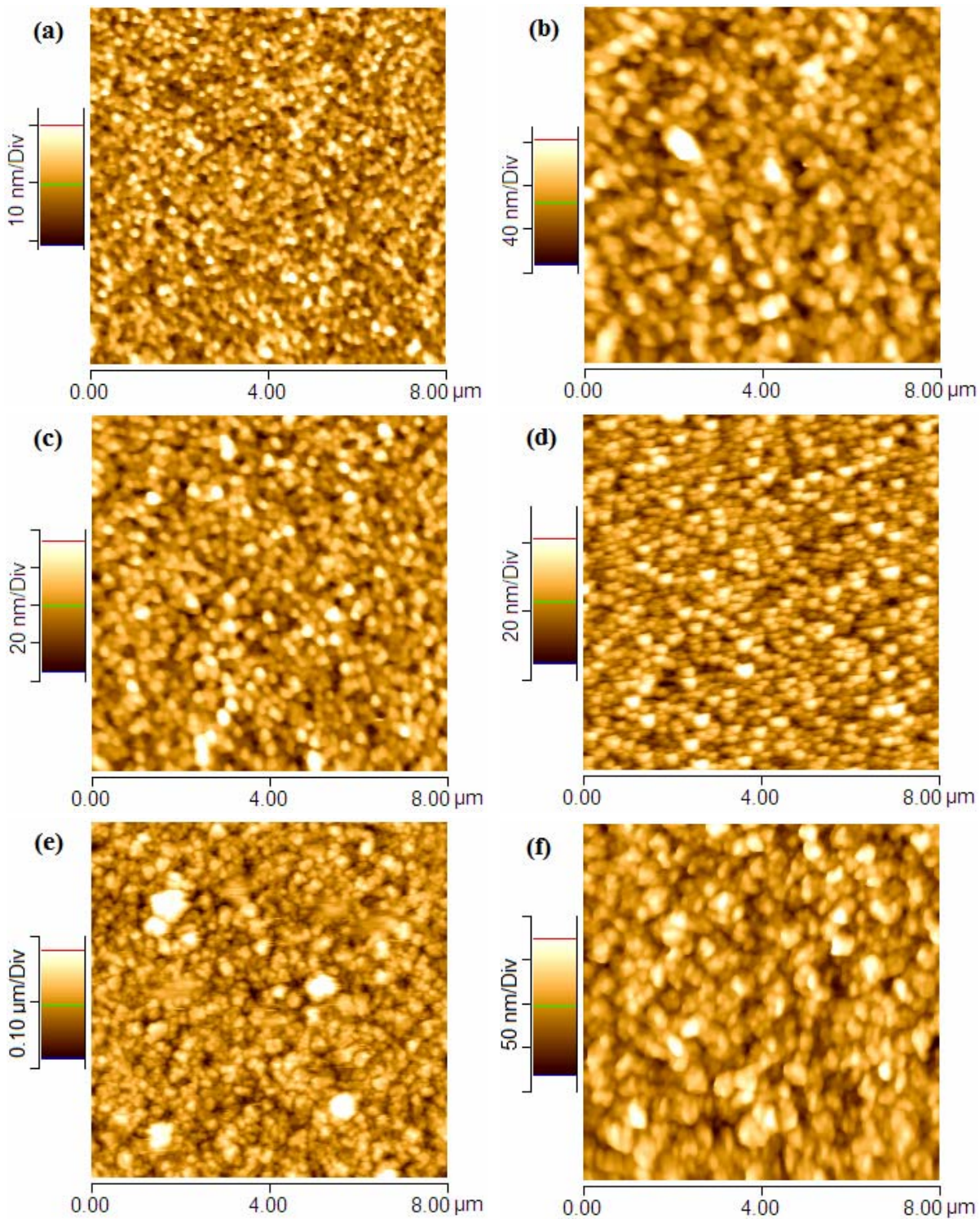


Fig 4.4.2 AFM micrographs of GaP/SiO₂ runs A - F.

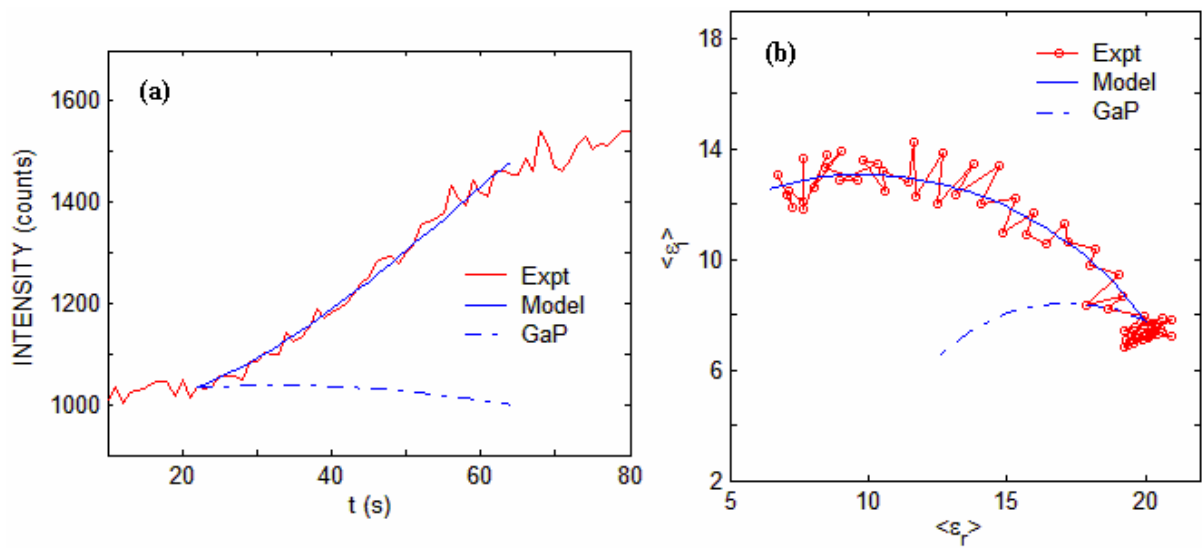


Fig 4.4.3 (a) RI and (b) $\langle \epsilon_r \rangle$ data at 2.64 eV for the initial stage of GaP/SiO₂ run A.

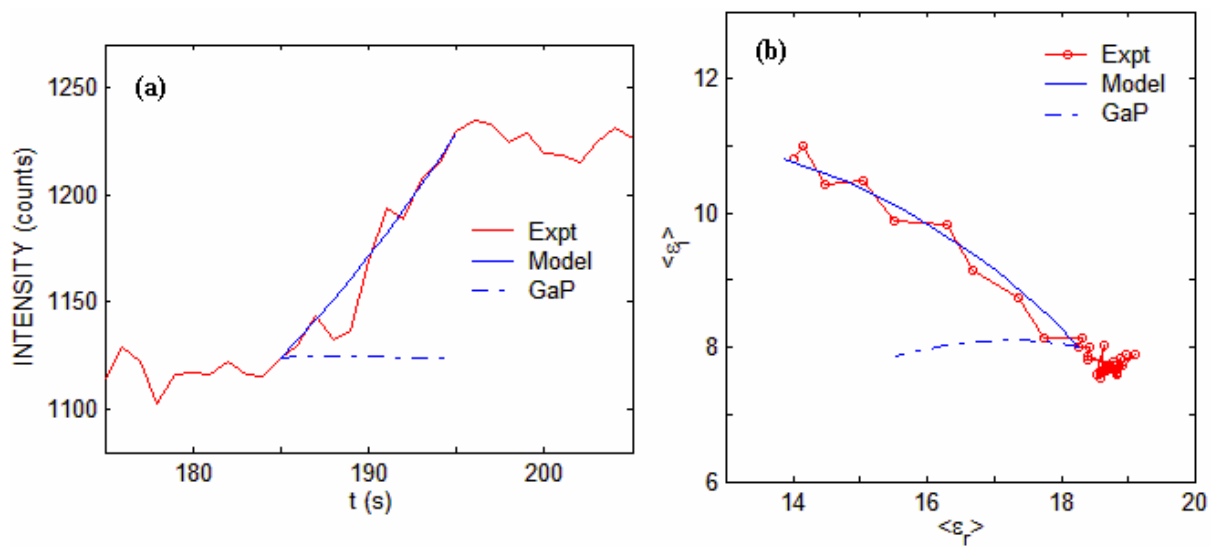


Fig 4.4.4 (a) RI and (b) $\langle \epsilon_r \rangle$ data at 2.64 eV for the initial stage of GaP/SiO₂ run B.

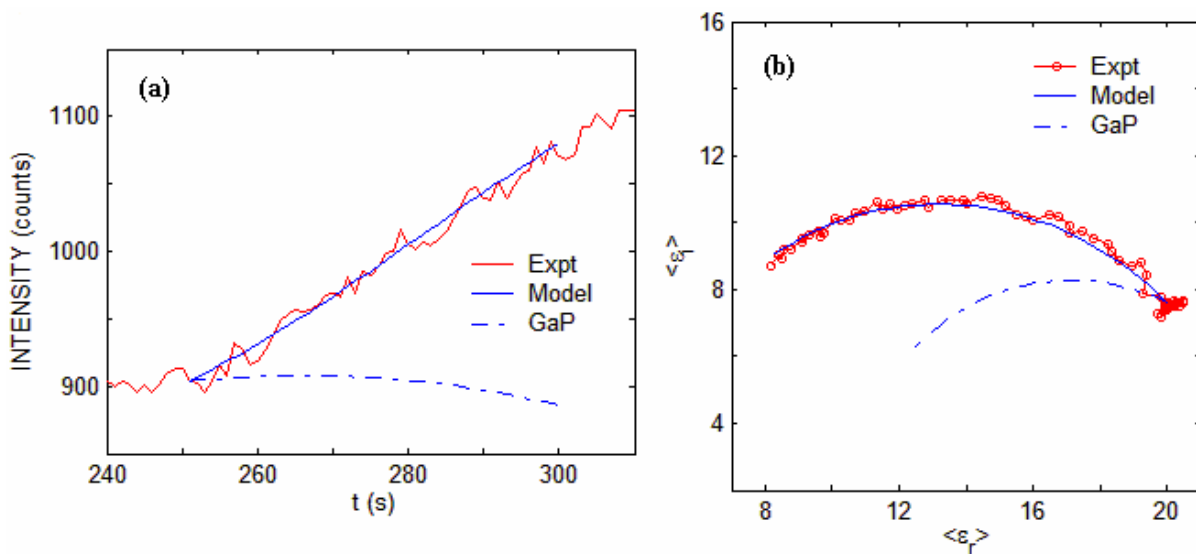


Fig 4.4.5 (a) RI and (b) $\langle \epsilon_r \rangle$ data at 2.64 eV for the initial stage of GaP/SiO₂ run C.

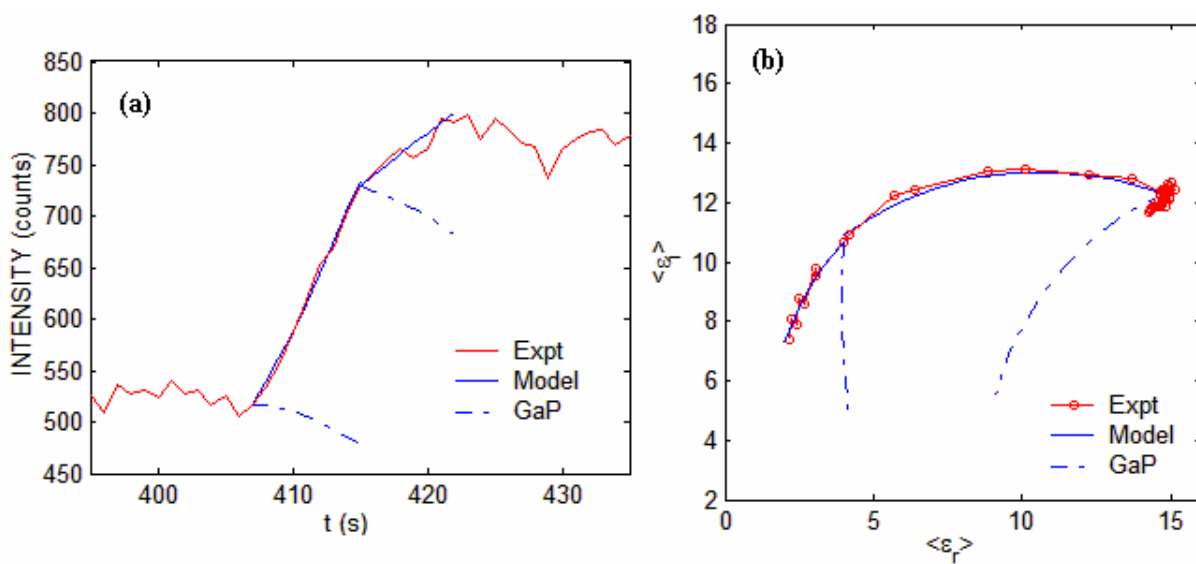


Fig 4.4.6 (a) RI and (b) $\langle \epsilon_r \rangle$ data at 2.64 eV for the initial stage of GaP/SiO₂ run E.

4.4.2 Lateral thickness profile of GaP / SiO₂

Figure 4.4.7 presents the lateral thickness profile of GaP / SiO₂ growth run C. The effective thickness is $T_E = 254.95 - 2.81 \times 10^{-9} e^{x/1.07}$ (x in mm, T_E in nm). The functional form is similar to the GaP / GaAs case, but both the pre-exponential factor and the characteristic length are much smaller. Figure 4.4.8 presents in (a) the calculated concentration change of the reactive gas-phase Ga species along the radius with the functional form $\Delta n = -2.81 \times 10^{-9} e^{x/1.07}$, and the resulting diffusion current shown in (b) is $J = e^{(x - 25.4)/1.07}$. Both are much smaller than GaP / GaAs and more confined to the edge (x = 25.4 mm). An image taken by an Epson Scanner for a corner of the sample run # C is shown in Fig. 4.4.9. The film exhibits an outer ring about 5 mm wide, whose color (blue) is different from that of the center (dark green). T_N drops quickly inside the blue region, but T_E does not show any change until 3 mm or closer to the edge. The reduced difference between T_N and T_E indicates that the edge quality is slightly better than that of the center. Further discussion is deferred to Section 4.5.3.

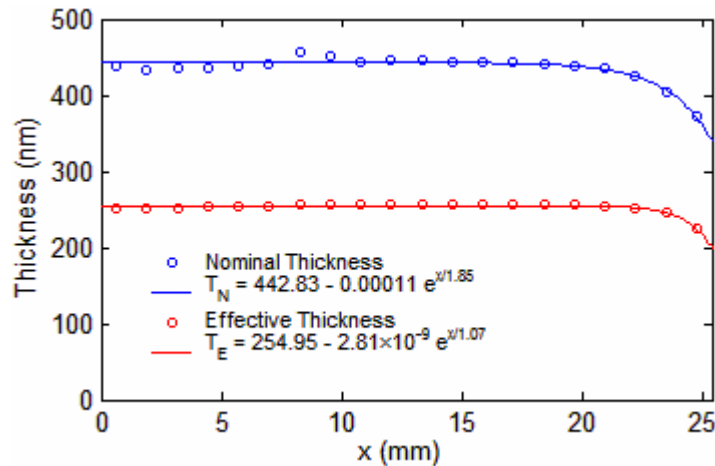


Fig 4.4.7 Thickness profile of GaP / SiO₂ run C.

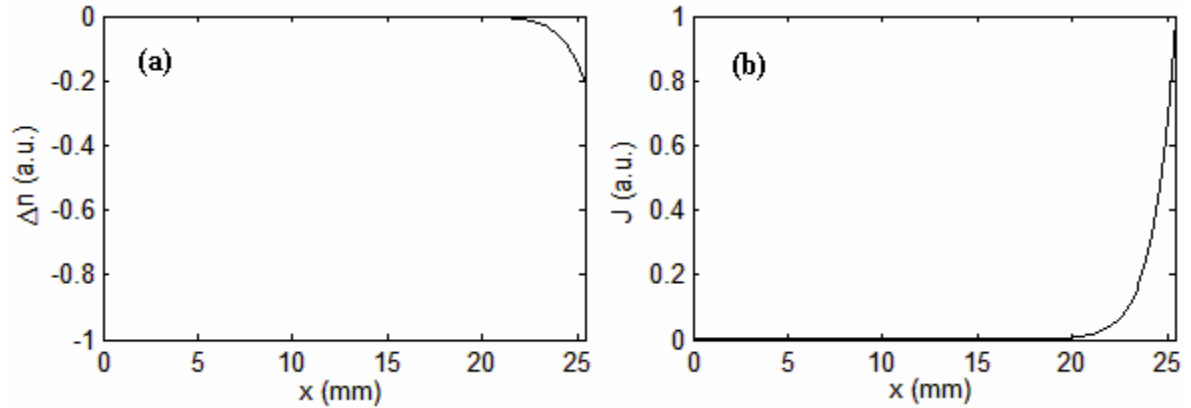


Fig 4.4.8 (a) Calculated concentration change of gas phase reactants along a radius for GaP / SiO₂ run C normalized to the center concentration. (b) Diffusion current resulting from (a) normalized to the edge flow.

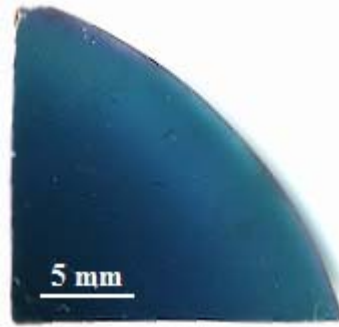


Fig 4.4.9 A segment of sample of GaP / SiO₂ run C.

Figure 4.4.10 presents the lateral thickness profile of GaP / SiO₂ TMG burst-growth run F. Here the effective thickness can be fitted linearly as $T_E = 301.5 - 0.07x$ (x in mm, T_E in nm). Thus the sample exhibits good thickness uniformity, with bulk crystalline qualities maintained throughout. An Epson Scanner image for a corner of sample run F is shown in Fig. 4.4.11. The sample has an overall dark green appearance, although the center is less shiny than the edge, indicating reduced surface quality in the center. Figure 4.4.12 presents the AFM micrographs of both regions. The average grain size is larger on the center than edge, and the RMS roughnesses are 26 nm and 13 nm respectively.

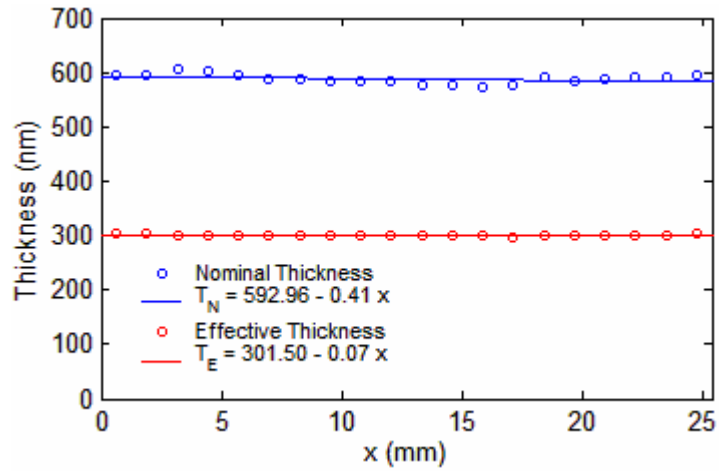


Fig 4.4.10 Thickness profile of GaP / SiO₂ run F.



Fig 4.4.11 A piece from the sample of GaP / SiO₂ run F.

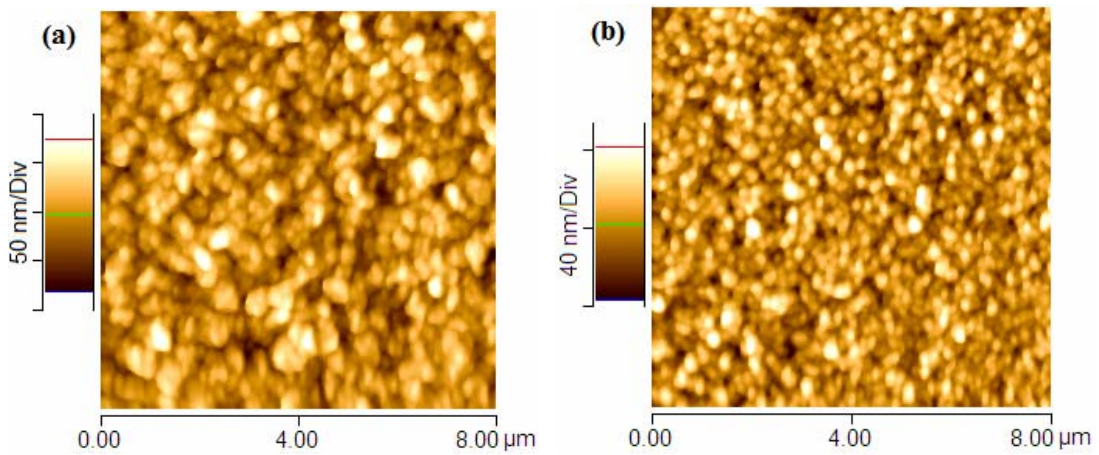


Fig 4.4.12 AFM micrograph for the (a) center and (b) edge of GaP / SiO₂ run F.

4.5 Discussion

4.5.1 Arrival-rate calculations: analysis of growth kinetics

It is seen that for GaP / GaAs and GaP / SiO₂, the growth rate is of the order of Å/s and roughly proportional to the TMG input flow, and can drop by a factor of 2 to 3 if the sample stage is not rotating (e.g., GaP / GaAs runs B and C). Also, in the extreme case of a TMG burst, the GaP homoepitaxial growth rate can increase by an order of magnitude. These data all suggest that growth under the current experimental conditions is mass-transport limited and Ga is the rate-limiting species. The above speculation can be justified by calculating the arrival rates and kinetic properties of various gas-phase species. These calculations will also yield useful insights concerning the growth process as well, such as an identification of reaction pathways.

The useful equations are summarized in Sec. 2.1.2.1. If growth is limited by surface kinetics, the density gradient of the reactant in the gas phase will be very small or negligible, and the concentration above the equilibrium growing surface will be close to or almost the same as that in the ambient. In this case the arrival rate at the surface is given by the homogenous impinging current, Eq. (2.1.2.6). It depends on the average velocity and the number density, and the final form is proportional to the partial pressure. If growth is limited by mass transport, the reactants are brought to the growth surface by diffusion through the stagnant layer, the surface concentration will be close to zero, and a large density gradient will exist. The arrival rate is then calculated from Eq. (2.1.2.12), which depends additionally on the mean free path. Given the arrival rate, the growth rate can be estimated together with the surface reaction probabilities. The various dimensionless numbers of our OMCVD system can also be calculated using the equations from Sec. 2.1.2.2 (see Table 4.5.3).

Tables 4.5.1 and 4.5.2 present the results of kinetic calculations for N_2 and H_2 carrier gases, respectively. Typical growth conditions are assumed, with temperature and total pressure fixed at 873 K and 4 Torr, and PH_3 and TMG flows of 1000 and 1 sccm. The mean free paths are assumed to be primarily determined by the carrier gas N_2 or H_2 with flow rates of 4000 or 9000 sccm, respectively, since these are the predominant constituents in the growth chamber. The thickness of the stagnant layer is assumed to be 1 cm, in accordance with Ref. [106]. For the growth-rate calculations, it is assumed that the surface reactions are rapid enough so that there is no delay for the incorporation of two adjacent atoms arriving at the same available site.

Based on the calculations above, Table 4.5.3 presents various dimensionless numbers under the same conditions. The growth chamber is 5" height and 6" in diameter, and the diameters of the Mo susceptor and sample are 3" and 2", respectively. Thus the system characteristic lengths are 5" for Kn and Re, and 1.5" for Pe.

The growth rates calculated from diffusion currents agree well with our experimental results, which are usually obtained with TMG flow of less than 1 sccm. Calculated homogeneous impinging currents are 1 or 2 order of magnitudes higher. Under typical conditions the arrival rates of P are thousands of times higher, so we can safely assume that the surface is essentially completely terminated with group-V species that can react with TMG. Hence it follows that growth is limited by mass transport of the Ga species with a concentration nearly zero at the surface, and a correspondingly large density gradient.

Table 4.5.1 Calculated gas-phase kinetic properties using N₂ as the carrier gas. The left 3 columns in the lower half assume that diffusion is not a factor and that growth is kinetically limited.

	Molecular mass (u)	Molecular Diameter (Å)	Partial pressure (Torr)	Number density (m ⁻³)	Average velocity (m s ⁻¹)	Mean free path (μm)
N ₂	24	2.9	3.2	3.54×10^{22}	878	60.5
P	31	2.0	0.8	8.85×10^{21}	772	60.5
PH ₃	34	2.84	0.8	8.85×10^{21}	737	60.5
Ga	70	2.6	8×10^{-4}	8.85×10^{18}	514	60.5
Ga(CH ₃) ₃	115	6.14	8×10^{-4}	8.85×10^{18}	401	60.5
H-P – Ga(CH ₃)	117	6.14	8×10^{-4}	8.85×10^{18}	398	60.5

Table 4.5.1 (continued)

	Impinging current (m ⁻² s ⁻¹)	Arrival rate (s ⁻¹)	Growth rate (nm s ⁻¹)	Diffusion coef. (m ² s ⁻¹)	Diffusion current (m ⁻² s ⁻¹)	Arrival rate (s ⁻¹)	Growth rate (nm s ⁻¹)
N ₂	7.77×10^{24}	1.15×10^6	-	-	-	-	-
P	1.71×10^{24}	2.54×10^5	3.46×10^4	0.020	1.72×10^{22}	2556	348
PH ₃	1.63×10^{24}	2.42×10^5	3.30×10^4	0.019	1.64×10^{22}	2441	333
Ga	1.14×10^{21}	169	23.0	0.013	1.15×10^{19}	1.70	0.23
Ga(CH ₃) ₃	8.87×10^{20}	132	18.0	0.010	8.94×10^{18}	1.33	0.18
H-P – Ga(CH ₃)	8.79×10^{20}	131	17.8	0.010	8.86×10^{18}	1.32	0.18

Table 4.5.2 As Table 4.5.1 but with H₂ as the carrier gas

	Molecular mass (u)	Molecular Diameter (Å)	Partial pressure (Torr)	Number density (m ⁻³)	Average velocity (m s ⁻¹)	Mean free path (μm)
H ₂	2	1.48	3.6	3.98×10^{22}	3040	232
P	31	2.0	0.4	4.42×10^{21}	772	232
PH ₃	34	2.84	0.4	4.42×10^{21}	737	232
Ga	70	2.6	4×10^{-4}	4.42×10^{18}	514	232
Ga(CH ₃) ₃	115	6.14	4×10^{-4}	4.42×10^{18}	401	232
H-P=Ga-CH ₃	117	6.14	4×10^{-4}	4.42×10^{18}	398	232

Table 4.5.2 (continued)

	Impinging current (m ⁻² s ⁻¹)	Arrival rate (s ⁻¹)	Growth rate (nm s ⁻¹)	Diffusion coef. (m ² s ⁻¹)	Diffusion current (m ⁻² s ⁻¹)	Arrival rate (s ⁻¹)	Growth rate (nm s ⁻¹)
H ₂	3.03×10^{25}	4.49×10^6	-	-	-	-	-
P	8.54×10^{23}	1.27×10^5	1.73×10^4	0.075	3.30×10^{22}	4908	669
PH ₃	8.16×10^{23}	1.21×10^5	1.65×10^4	0.071	3.16×10^{22}	4687	639
Ga	5.68×10^{20}	84.4	11.5	0.050	2.20×10^{19}	3.27	0.45
Ga(CH ₃) ₃	4.43×10^{20}	65.9	9.0	0.039	1.72×10^{19}	2.55	0.35
H-P=Ga-CH ₃	4.40×10^{20}	65.3	8.9	0.039	1.70×10^{19}	2.53	0.34

Table 4.5.3 Dimensionless numbers of our OMCVD system under N₂ and H₂ flows.

Carrier Gas	Flow rate (sccm)	Volume flow (m ³ s ⁻¹)	Vertical flow (m s ⁻¹)	Mass density (kg m ⁻³)	Viscosity (kg m ⁻¹ s ⁻¹)	Kundsen number (Kn)	Reynolds number (Re)	Péclet number (Pe)
N ₂	5000	0.051	2.8	1.76×10^{-3}	4.68×10^{-5}	4.8×10^{-4}	13.3	8.2
H ₂	10000	0.101	5.6	1.47×10^{-4}	5.05×10^{-5}	1.8×10^{-3}	2.1	4.3

In the above calculations, we have assumed that the steady-state n_s and equilibrium-state concentrations n_{eq} are both zero above the surface. The assumption that $n_{eq} = 0$ is quite accurate since at 600 °C the equilibrium partial pressure of Ga above a GaP surface is $\sim 10^{-12}$ Torr [107]. This corresponds to a number density $\sim 10^{10} \text{ m}^{-3}$. However the assumption that $n_s = 0$ needs to be examined more carefully. We do this by assuming that only $n_{eq} = 0$ and evaluating the mass transfer flux by means of the following steps, which is similar to that of Ref. [106]. We first calculate the surface reaction rate constant K_S using Eq. (2.1.2.8). The Damköhler number (Da) can then be obtained using Eq. (2.1.2.20). The steady-state concentration of nutrients above the growing surface can now be calculated from the ambient value together with Da and $n_{eq} = 0$ using Eq. (2.1.2.23). Finally, the mass-transfer flux J_{MT} is given by Eq. (2.1.2.22). The results for various Ga species are listed in Table 4.5.4. It is seen that the equilibrium concentration above the growing surface is on the order of 10^{16} to 10^{17} which is only about 1% to 4% of the ambient value. Therefore, the growth rates are almost the same or only slightly smaller compared to those calculated assuming that $n_s=0$.

Table 4.5.4 Growth rate of various Ga species calculated from surface reaction rates.

Carrier Gas	Ga Species	Surface reaction rate (m s^{-1})	Damkohler number (Da)	Surface number density (m^{-3})	Mass transfer flux ($\text{m}^{-2}\text{s}^{-1}$)	Arrival rate (s^{-1})	Growth rate (nm s^{-1})
N_2	Ga	128	99	8.83×10^{16}	1.13×10^{19}	1.68	0.23
	$\text{Ga}(\text{CH}_3)_3$	100	99	8.83×10^{16}	8.85×10^{18}	1.31	0.18
	H-P=Ga- CH ₃	99	99	8.83×10^{16}	8.77×10^{18}	1.30	0.18
H_2	Ga	128	26	1.65×10^{17}	2.12×10^{19}	3.14	0.43
	$\text{Ga}(\text{CH}_3)_3$	100	26	1.65×10^{17}	1.65×10^{19}	2.45	0.33
	H-P=Ga- CH ₃	99	26	1.65×10^{17}	1.64×10^{19}	2.43	0.33

Taking N₂ carrier gas as an example, the average residence time of available Ga atoms inside the chamber is:

$$t_r = \frac{V}{\text{Volume flow rate}} = \frac{0.0023}{0.0506} = 0.05s, \quad (4.5.1)$$

assuming that there is no reaction and atoms just get swept away by the advection flow. However, the average incorporation time for a single Ga atom is:

$$t_{c1} = \frac{1}{\text{Arrival rate}} = \frac{1}{1.33} = 0.75s. \quad (4.5.2)$$

Then the average total time to consume all available Ga atoms is:

$$\begin{aligned} t_c &= t_{c1} \frac{N}{\text{Available sites}} \\ &= 0.47 \times \frac{0.0023 \times 8.85 \times 10^{18}}{\pi \times (1 \times 0.0254)^2 \times 2 / (5.45 \times 10^{-10})^2} = 0.75 \times \frac{2.04 \times 10^{16}}{1.36 \times 10^{16}} = 1.13s. \end{aligned} \quad (4.5.3)$$

Since even if t_{c1} and t_c are larger than t_r growth is still mass-transport limited, a stagnant layer must exist above the growing surface, where the transport of the Ga species is less affected by bulk advection and appears to be “trapped”. The concentration of the Ga species on top and bottom of the stagnant layer has the ambient value $\sim 10^{18} \text{ m}^{-3}$ and the surface value $\sim 10^{16}$ to 10^{17} m^{-3} , respectively. The density gradient that results drives the vertical diffusion current that directs Ga to the growth surface. As noted above, the thickness of the stagnant layer is of the order of 1 cm. Under similar growth conditions it is larger for H₂ than for N₂ due to the enhanced diffusion capability of H₂. In principle the thickness of the overall stagnant layer can be reduced by sample rotation, which generates a downward pulling action on the bulk flow. However, as has been discussed in Sec. 4.2.2, the growth parameters other than the rate are observed to be relatively unaffected by rotation.

The Knudsen numbers are of the order of 10^{-4} to 10^{-3} . Thus the assumption of continuous gas flow is valid for our system. The Reynolds numbers are less than 25, so our flow conditions are well within the regime of laminar flow without rippling or turbulence.

The Péclet numbers are larger than 1 but smaller than 10, which mean that the primary mechanism of horizontal mass transport inside the stagnant layer is advection. However, diffusion can also play a minor role, which becomes more important when H₂ is used as the carrier gas.

From the above calculations it is not obvious which form of Ga is the precursor to growth. The growth rates calculated from the arrival rates of Ga, Ga(CH₃)₃, and H-P=Ga-CH₃ are very similar. Moreover, the exact behavior of lateral nutrient transport inside the stagnant layer is also not clear from the above. Thus additional analyses on growth mechanisms and lateral thickness variations are needed, which will be the topics of the subsequent sections. Unfortunately, the optical measurements are of no help here, because neither the stagnant layer nor its individual constituents have a unique spectral signature in our accessible spectral range.

4.5.2 Lateral thickness variations: implications for growth chemistry

As we have seen in the results section, the films grown in our vertical-flow low-pressure OMCVD reactor usually have nonuniform lateral thickness profiles, with the deposited GaP films either thinner or thicker at the edges than in the middle, but in either case showing an exponential dependence on radius. Meanwhile there are polycrystalline GaP material deposited on the Mo susceptor that surrounds the actual substrate. While nonuniformly thick epitaxial layers are a common problem in epitaxy, these are usually attributed to depletion of gas-phase reactants, which in vertical-flow reactors occurs from the center outward. Our thickness variations do not fall in this category, and as a result provide new information about OMCVD growth processes.

Table 4.5.5 summarizes some representative results, including the growth conditions and rates, the lateral effective thickness T_E along a 1'' sample radius, and the corresponding

calculated change of the nutrient concentration $\Delta n/n_0$ normalized to the center value. Here $\Delta n(x) = n(x) - n_0$ and $n_0 = n(x = 0)$. Only average values are shown for the TMG flow and the growth rate at the center of the film.

Table 4.5.5 Summary of the effective lateral thickness profiles for representative runs.

Growth	Carrier gas	Rot.	T (°C)	V/III ratio	Average TMG flow (sccm)	Average center growth rate (nm/s)
GaP / GaAs run A	H ₂	Y	570	3269	0.52	0.15
GaP / GaAs run C	H ₂	N	580	526	0.38	0.06
GaP / SiO ₂ run C	H ₂	Y	570	6800 / 400	0.25	0.09
GaP / SiO ₂ run F	N ₂	Y	600	<< / 6154	>> / 0.52	0.17
GaP / nrSi (1:1:1) run A	N ₂	N	600	2747	0.91	0.21

Table 4.5.5 (continued) (x in mm)

Growth	T _E (nm)	$\Delta n/\Delta n_0$
GaP / GaAs run A	$74.5 - 0.3 e^{x/5.52}$	$-3.5 \times 10^{-3} e^{x/5.52}$
GaP / GaAs run C	$134.3 - 0.5 e^{x/5.98}$	$-4.2 \times 10^{-3} e^{x/5.98}$
GaP / SiO ₂ run C	$255.0 - 2.8 \times 10^{-9} e^{x/1.07}$	$-2.8 \times 10^{-9} e^{x/1.07}$
GaP / SiO ₂ run F	$301.5 - 0.07 x$	$-2.0 \times 10^{-4} x$
GaP / nrSi (1:1:1) run A	$107.3 + 0.3 e^{x/5.02}$	$3.1 \times 10^{-3} e^{x/5.02}$

The lateral thickness profile is a direct indication of difference in the local growth rate. As growth is diffusion limited, the growth rate is proportional to the local concentration of the gas-phase reactants, $n(x)$. The analytic forms of $n(x)$ can be calculated from the 1D continuity equation

$$\nabla \cdot \bar{J} + \frac{\partial n}{\partial t} = G - R, \quad (4.5.4)$$

where \bar{J} is the lateral mass transport current, and G and R are the generation and removal of reactants, respectively. Under the steady state condition, $\frac{\partial n}{\partial t} = 0$. Assuming that the

lateral mass transport is by diffusion only, $\bar{J} = -D \frac{\partial n}{\partial x} \hat{x}$, and also assuming that the removal rate has the form of an exponential decay with time constant τ , $R = -\frac{n}{\tau}$. Here

$\frac{1}{\tau} = \frac{1}{\tau_1} + \frac{1}{\tau_2} + \frac{1}{\tau_3}$, with τ_1 , τ_2 , and τ_3 representing the time constants due to deposition,

decomposition, and removal by advection, respectively. Thus Eq. (4.5.4) becomes

$$-D \frac{\partial^2 n}{\partial x^2} = -\frac{n}{\tau} + G \quad (4.5.5)$$

which can be solved using the Green's function approach as follows.

The corresponding homogeneous form of Eq. (4.5.5) is

$$-D \frac{\partial^2 n}{\partial x^2} = -\frac{n}{\tau} \quad (4.5.6)$$

for which the solutions are:

$$n(x) = C e^{\pm x/L} \quad (4.5.7)$$

where $L = \sqrt{D\tau}$ is the characteristic length of diffusion. The Green's function n_G for Eq. (4.5.5) satisfies:

$$-D \frac{\partial^2 n_G}{\partial x^2} = -\frac{n_G}{\tau} + \delta(x - x_0) \quad (4.5.8)$$

The trial solution of n_G can be obtained from Eq. (4.5.7) by requiring the boundary conditions of $n_G(x = \pm\infty) = 0$, and it has the form

$$n_G(x, x_0) = C e^{-|x-x_0|/L} \quad (4.5.9)$$

where $C = \frac{L}{2D}$ is obtained by integrating Eq. (4.5.8) over an infinitesimal small region around x_0 .

With the Green's function n_G determined, the solution for the inhomogeneous case Eq. (4.5.5) can be readily obtained to be

$$n(x) = \int dx_0 n_G(x, x_0) G. \quad (4.5.10)$$

If $G = n_0$ exists over $x_0 \in (-\infty, +\infty)$, then

$$n(x) = \int_{-\infty}^{+\infty} n_G(x, x_0) n_0 dx_0 = \frac{n_0 L^2}{D}, \quad (4.5.11)$$

which is a constant. Physically it means that if the source is uniformly been generated over a large area, the reactant concentration above will be uniform. However if $G = n_0$ exists over $x_0 \in (-\infty, a)$, then

$$n(x) = \int_{-\infty}^a n_G(x, x_0) n_0 dx_0 + \int_a^x n_G(x, x_0) n_0 dx_0 = \frac{n_0 L^2}{D} - \frac{n_0 L^2}{2D} e^{(x-a)/L} \quad \text{for } x < a, \quad (4.5.11)$$

and

$$n(x) = \int_{-\infty}^a n_G(x, x_0) n_0 dx_0 = \frac{n_0 L^2}{2D} e^{-(x-a)/L} \quad \text{for } x > a, \quad (4.5.12)$$

which join smoothly at $x = a$. These two solutions correspond to the two different analytic forms of T_E in Table 4.5.5, and an example for the case of $a = 0$ and $L = 5$ is plotted in Fig. 4.5.1. Thus the reactant concentration varies as a negative exponential and an exponential decay for the regions above and beyond the source, respectively. Generalization to the case of two adjacent regions with different source generation rates is straightforward.

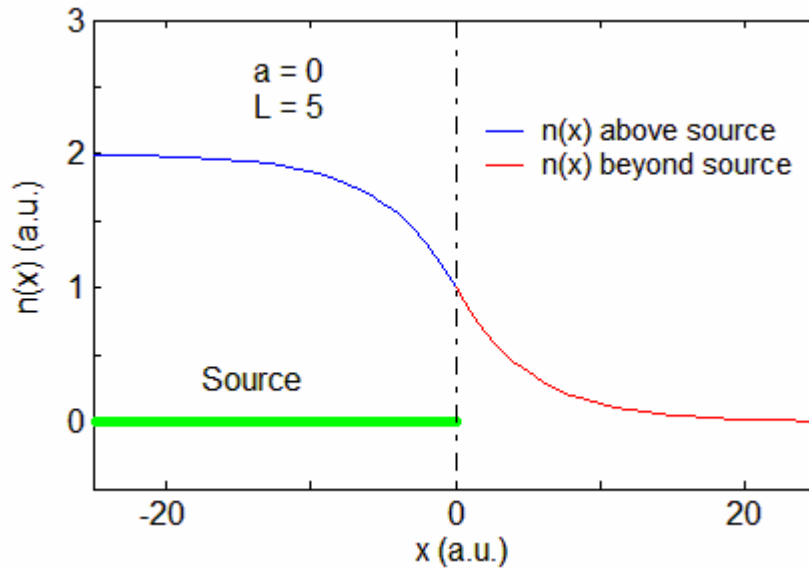


Fig 4.5.1 Plots of Eqs. (4.5.11) and (4.5.12) for $a = 0$ and $L = 5$.

GaP / nrSi (1:1:1)

From the above calculation, the case of GaP / nrSi (1:1:1), where the edge is thicker than the center, can be readily explained by an extra supply of reactants from the region outside the sample. Because the catalytic effect of a rough GaP film is not as strong as that of a single-crystal surface, we argue that the decomposition of PH_3 above the growing nrSi (1:1:1) surface is not as complete as in other cases, and that additional PH_3 cracking will occur on the Mo susceptor edge, where the temperature is about 100°C higher than that of the Si wafer. Also there may be catalysis effects coming from the Mo susceptor itself, or the polycrystalline GaP layer that is deposited on it. The decomposition products, which we assume are H-P=Ga-CH_3 adducts, back-diffuse against the advection flow and result in additional growth on the outer edge of the nrSi (1:1:1) wafer. Alternatively, it may be the reactive P species that are generated, which back-diffuse to compete with the upstream P species to generate more H-P=Ga-CH_3 adducts. Either model is consistent with the fact that the Péclet number of our system is not very large (< 10). Thus diffusion can certainly co-exist with advection, although its effect will be less. More importantly, this means that

the downstream reactants are able to diffuse upstream into the system.

The extent of backward diffusion of H-P=Ga-CH₃ or P can also be estimated from a 2D random walk model. A molecule travels on the average distance of $\sqrt{N}\lambda$ after N random collisions with the ambient. It stops when the front velocity between the (N – 1)th and the Nth collisions is equal to the ambient advection velocity U, or:

$$\frac{(\sqrt{N} - \sqrt{N-1})\lambda}{\lambda/V} = (\sqrt{N} - \sqrt{N-1})V = U \quad (4.5.4)$$

where λ is the mean free path and V the thermal velocity. Using the numbers from Tables 4.5.1 and 4.5.3, $\lambda = 60.5 \mu\text{m}$, $V = 878 \text{ m/s}$, and $U = 2.8 \text{ m/s}$, we get $N = 2.46 \times 10^4$, so the path length is

$$L = \sqrt{N}\lambda = \sqrt{2.46 \times 10^4} \times 60.5 \times 10^{-4} \cong 0.9 \text{ cm}. \quad (4.5.5)$$

which is comparable to the observed characteristic length in T_E (0.5 cm), the susceptor width (1.3 cm), and half the sample radius (1.3 cm). Thus it further supports the interpretation of backward-diffusion of the reactants.

GaP / Si and GaP / nrSi (1% NH₄F)

The unique surface morphology of GaP / Si, as shown in Fig. 4.2.4, is a clear indication of different growth kinetics happening over different sample regions, especially regarding the back-diffusion of reactants from the susceptor edge. This is consistent with the above interpretation as follows.

As will be discussed in Sec. 4.5.3, (001) Si is not effective in either catalyzing the decomposition of PH₃ or promoting the adsorption of reactants for surface reactions. Hence neither the partial pressure of H-P=Ga-CH₃ dimers over the center of the sample nor the surface density of the adsorbed reactants are high enough to allow for the growth of a continuous film, and islands with large sizes and spacings are formed. The concentration of

gas-phase reactants in the form of H-P=Ga-CH₃ dimers also gradually decreases towards the edge due to out-diffusion. Eventually it becomes too small to result any immediate nucleation, and thus a bare Si belt is formed as seen in Fig. 4.2.4. Precursors impinging on this region would diffuse in both directions. Those moving toward the center enter a region that already has enough nuclei to allow them incorporate without further diffusion. This accounts for the formation of transition regions consisting of two belts of different colors, which are due to different island sizes and spacings. Those moving outside will eventually desorb, since there are fewer surface reactants available.

However, as usual most of the PH₃ passing over the growing surface is not decomposed. Using the same argument as before, additional cracking will occur on the Mo susceptor, and more H-P=Ga-CH₃ adducts are generated. The adducts back-diffuse into the region above the edge area and result in edge growth that is separated from the center region. The inner part of the edge ring is affected by the diffusion of adatoms from the bare Si region, thus it is hazier. As seen from the AFM results of Fig. 4.2.3, the edge is smoother than the center, which suggests that the H-P=Ga-CH₃ concentration above the edge is higher than that in the center. Thus the decomposition efficiency of PH₃ above a Si substrate is consistently seen to be very low.

Growth on nrSi (1% NH₄F) substrates also suffer from the same problem of low PH₃ decomposition efficiency as in the cases of nrSi (1:1:1) and non-roughened Si. Thus the formation of the morphology in Fig. 4.3.12 can also be explained in consistent with the above. Additional PH₃ cracking happens on the susceptor followed by the back-diffusion of the adducts generated. The adducts density becomes smaller when moving from the edge to the center, thus a continuous rough GaP film is deposited around the outmost ring, and the nucleation density on the nrSi (1% NH₄F) surface gradually decreases towards the center, as seen from the less dense hazy patterns. As discussed in Sec. 4.5.2, since the nucleation of GaP and the generation of adducts are even less favored on nrSi (1% NH₄F) than on

non-roughened Si, growth here is primarily initiated from the effect of back-diffusion, thus no nrSi belt is observed.

GaP / GaAs

According to the calculation results, the first two cases for GaP / GaAs in Table 4.5.5, where the edge is thinner than the center is explained by the loss of growth nutrients at the edge. The analytic form $\Delta n = -Ce^{x/\lambda}$ is expected to change to $\Delta n = C'e^{-x/\lambda}$ above the Mo susceptor, although thickness measurement of the GaP deposited on the susceptor are not possible.

Consistent with the earlier discussions, the reason here for the existence of a reactant concentration gradient towards the edge is that, PH₃ decomposition is more efficient over the center region of GaAs and high-quality heteroepitaxial GaP than over the polycrystalline GaP that is deposited on the Mo susceptor. As a result, more adducts are generated above the wafer than the susceptor, and the diffusion current that is generated travels outward, as opposed to the GaP/nrSi (1:1:1) case. In addition, the laminar flow velocity is larger above the susceptor due to pumping and stage rotation, which also facilitates the removal of reactants and promotes diffusion.

GaP / SiO₂

The 3rd and 4th cases in Table 4.5.5 for GaP / SiO₂ are similar to that of GaP / GaAs. However, both the exponential factor and the characteristic length for the 3rd case are smaller comparing to that of GaP / GaAs. This is consistent with the fact that the heterogeneous catalysis effect of SiO₂ and the resulting low-quality GaP on PH₃ decomposition is between that of GaAs or high-quality GaP on the one hand, and Si or nrSi on the other. However, it is very similar to that of the polycrystalline GaP coated on the Mo susceptor. Here, the extent of reactant out-diffusion is significantly smaller than in the GaAs case, and the

resulting thickness difference is also smaller, consistent with observations.

The above effect is more obvious when growth conditions are changed, as in the 4th example of GaP / SiO₂ in Table 4.5.5. Here, the lateral thickness profile is almost uniform, with T_E being linear.

4.5.3 Growth mechanisms

From our data we have seen that under normal conditions, the growth modes and qualities of the heteroepitaxial GaP are primarily determined by the nature of the substrate, as summarized in Table 4.5.6. We will discuss each case below. The objectives are: (1) to relate our data to the theories of nucleation and epitaxy as described in Ch. 2, (2) to make comparisons with the prior works of others that are reviewed in Ch. 1, and (3) to provide consistent explanations of our data based on the above so as to build up a model for the growth mechanisms.

Table 4.5.6 The effect of different substrates and growth condition on GaP heteroepitaxy.

Substrate	Growth mode	Heteroepitaxial GaP
(001) GaAs	2D nucleation mediated layer-by-layer	Single crystal film
(001) GaAs, high supersaturation	Pseudo 2D nucleation mediated	Rough film
Singular and vicinal (001) Si	3D nucleation mediated	3D islands
nrSi (1:1:1)	Continuous	Rough film
nrSi (1:3:5), nrSi (1% NH ₄ F)	3D nucleation mediated	3D islands
Thermally generated SiO ₂	Pseudo 2D nucleation mediated	Polycrystal film

Many prior workers have attempted to address the homoepitaxial growth mechanisms of III-V materials and the decomposition behavior of various precursors, as reviewed in Ch. 1.

These are briefly summarized here. Larsen et al. [35] found that the PH_3 decomposition is enhanced heterogeneously on InP, and Buchan et al. [36, 37] found that it is further enhanced by the presence of TMI. Buchan et al. [37] proposed the growth mechanism of InP from TMI and PH_3 to be as follows. For temperatures below 400 °C, adducts of $(\text{CH}_3)_3\text{In} : \text{PH}_3$ are formed on the InP surface through either homogeneous reactions in the gas phase followed by adsorption, or heterogeneous reactions of individually adsorbed species through the LH mechanism. The adducts are then reduced heterogeneously through CH_4 eliminations. For temperatures above 400 °C, adduct formation is primarily homogeneous followed by the elimination of the first CH_4 molecule. Further CH_4 eliminations in $(\text{CH}_3)_2\text{In}-\text{PH}_2$ can happen either homogeneously or heterogeneously. Similar behaviors have been found for the homoepitaxial growth of GaAs through AsH_3 and TMG [38, 39], and the formation of an intermediated adduct was detected by infrared adsorption spectroscopy [47]. The activation energies of PH_3 decomposition on various substrates are measured to be: 2.40 eV (55.3 kcal/mol) [40] on Si, 1.92 eV (44.2 kcal/mol) [40] or 1.99 eV (46 kcal/mol) [35] on SiO_2 , and 1.56 eV (36 kcal/mol) [35] on InP. They are all smaller than the PH_2 -H bond strength of 3.92 eV (90.3 kcal/mol). The above information will be very illustrative in analyzing our data.

GaP / (001) GaAs

Under ordinary growth conditions, heteroepitaxial GaP films on (001) GaAs substrates are usually single-crystal with low void concentrations ($< 4\%$) and smooth terminating surfaces (RMS roughness < 1.5 nm). The real-time SE and SR data show oscillation patterns in the transparent region, which can be analyzed on a point-by-point basis (1 s per point) and indicate that high-quality GaP grows at a rate of approximately 0.1 nm/s. Thus the heteroepitaxy of GaP on (001) GaAs proceeds as 2D-nucleation-mediated layer-by-layer growth. The above follows because GaP and GaAs are chemically similar, hence the

interfacial energy $\gamma_{\text{GaP}/\text{GaAs}}$ is very small and 2D growth is thermodynamically favored.

The homogeneous decomposition of PH_3 in the gas phase is a low-probability event for our growth temperatures of the order of 600 °C. However, since both PH_3 and GaAs are polar materials, the strong dipole interaction with GaAs catalyzes the heterogeneous decomposition of PH_3 , resulting in products that chemisorb onto the Ga sites and essentially saturate the surface with P. Similarly for TMG, the decomposition is expected to go to completion with products of Ga and Ga-CH_3 chemisorbed onto the As or P sites. The strong chemisorptions facilitate the readily generation of GaP from the above adsorbates, either directly or through the removal of a methyl radical (for Ga species) or H atoms (for P species). Also, the nature of a (001) GaAs surface provides a perfect template for the growth of GaP, where the Ga and P sites are evenly distributed among two interpenetrating fcc lattices. Since the chemisorbed precursors are highly supersaturated with respect to the critical 2D nuclei, they can easily attach to the nuclei edge and contribute to the lateral overgrowth, as suggested by Eqs. (2.1.3.19) to (2.1.3.22) in Sec. 2.1.3.2. Subsequent GaP homoepitaxy will follow a similar route. Thus 2D nucleation-mediated layer-by-layer growth mode is achieved.

It is seen that reduced V/III ratios result in rougher surfaces. This can also be explained by nucleation. As an example, we consider the extreme case of a TMG burst where the surface becomes really rough. Under large TMG flow Ga supersaturation also becomes large, and the nucleation energy barrier and critical nucleus size for Ga species will become smaller, as suggest by Eqs. (2.1.3.26) and (2.1.3.27). At sufficiently high supersaturation, the Ga adatoms can effectively nucleate to form Ga droplets at any location, even on P sites. At the end of the burst the Ga droplets are converted to GaP islands, which results in a rough morphology, as observed in our data for the deposits of GaP/GaAs runs E and F in Sec. 4.1.1. To prevent this from happening, the P supersaturation should also be increased accordingly, so the stoichiometry can be maintained and the two sub-lattices of Ga

and P can grow at the same rate.

It should be noticed that in the TMG burst mode the morphology will still tend to be rough, even if the PH_3 flow is increased so the V/III ratio is maintained. This is because under large supersaturation or highly nonequilibrium conditions, the nucleation energy barrier and critical size are both smaller, so new 2D nuclei will have equal opportunity to form on existing nuclei instead of new material simply by incorporating at step edges. The nucleation rate will be very large. Thus for kinetic reasons growth will tend toward the pseudo 2D mode even if the 2D layer-by-layer mode is thermodynamically preferred. The result will be a rough morphology, again consistent with our data, specifically the GaP/GaAs run # F as in Sec. 4.1.1.

Despite the fact that a TMG burst could increase the nucleation density and growth rate, the associated rough morphology and large structure defects counteract its merits. It is thus concluded that the growth conditions of TMG burst or high Ga supersaturations are not desirable.

GaP / Si

Under normal growth conditions, our data clearly show that the heteroepitaxy of GaP on singular and vicinal (001) Si proceeds as widely spaced 3D islands that fail to coalesce even over long periods of time. The characterization length of the sizes and spacings of the islands are both of the order of microns. As a comparison, the average distance between adjacent atomic steps for (001) Si with a 4° miscut is only about 8 nm. From the nucleation-theory point of view, this observed 3D growth mode clearly indicates that atomic-height steps and smooth surfaces of Si are not effective in promoting nucleation. This is consistent with the finding of Soga et al. [16], who have also found that the spacings of GaP islands grown on vicinal (001) Si are from 1 to 3 μm . We suggest that the above is due to two reasons below.

The first is that the nucleation energy barrier is too high. Since GaP and Si are chemically incompatible, the interfacial energy between these two materials is very large, with $\gamma_{Si} < \gamma_{GaP} + \gamma_{GaP/Si}$. From Young's equation (2.1.3.24), this corresponds to the situation where $\theta > 0$. Thus the 3D growth mode is preferred thermodynamically. Also the nucleation energy barrier ΔG^c , which is given by Eq. (2.1.3.27), will be very large. As suggested in Ch. 2, to reduce ΔG^c we have the options of increasing the substrate surface energy γ_{sv} and/or decreasing the film-substrate interfacial energy γ_{fs} . These can be accomplished through the use of nrSi and SiO₂ substrates, respectively, as will be discussed later.

The second is that the surface density of adsorbed reactants, which is the pre-exponential factor of Eq. (2.1.3.30), is too low. Since Si is a nonpolar material, the interaction between the Si substrate and PH₃ is minimized. Thus (001) Si cannot promote the same level of heterogeneous catalysis for PH₃ decomposition as seen with (001) GaAs. This is also suggested by the larger PH₃ decomposition activation energy measured on Si than polar or III-V substrates. Given that the concentration of H-P=Ga-CH₃ adducts in the gas phase is very low, the formation of such GaP precursors must be done primarily on the Si surface via reactions between independently adsorbed P and Ga species. However, the nonpolar nature of Si means that the adjacent cation and anion sites required for the selective chemical adsorption of P and Ga species as precursors to H-P=Ga-CH₃ adducts are not present. In addition, the reactants are expected to be physisorbed not chemisorbed. Physisorbed molecules have smaller desorption energies than chemisorbed molecules and hence will spend less time on the substrate and travel shorter distances, as seen from Eq. (2.1.3.13). The net result is that the collision probability or equivalently, the reaction probability between the Ga and P species is very small. Thus nucleation is generally not possible, except perhaps at occasional defect sites.

There are several ways to change the situation. One way is to trying to increase the

formation probability and supersaturation of H-P – Ga-CH₃ dimers in the gas phase. The use of higher PH₃ flows would help, since it partially compensates for the inefficiency of PH₃ decomposition above a Si substrate, and the ratio of reactive P/Ga species can be increased. As seen from the GaP on Si growth run C which uses a higher PH₃ flows than runs A and B, the nucleation density becomes larger, and the resulting GaP islands have almost coalesced in the central region and a continuous polycrystalline GaP film is formed near the edge. However this approach is still not effective alone in producing good quality GaP films, and results in too much waste of the PH₃ precursor.

The reason for the above is that, the reaction probability, or equivalently, the collision probability to form H-P=Ga-CH₃ adducts, is also limited by the number densities of the reactive P and Ga species, as suggested by Eq. (2.1.2.10), which are in turn proportional to the partial pressures. In our experimental configuration the chamber pressure is established by a throttle valve placed before the pump. For hardware issues the experiments in this work were all done under a chamber pressure of 4 Torr. That is far less than the typical OMCVD growth pressure used by others, as seen in Table 1.1. In fact, the use of atmospheric pressure is not unusual. As seen earlier in Sec. 4.2.2, the best result that has been achieved in our OMCVD system prior to the present investigation was done with a chamber pressure of 60 Torr. In that case, the individual partial pressures for P and Ga species are 10 times higher and the collision probability is 100 times higher than the present work. Since then, the hardware problems have been solved, and we will investigate the influence of system pressure further in the future.

Another way to promote reaction is to terminate the Si with a polar compound, e.g., SiO₂. This converts physisorption into chemisorption, with its correspondingly much larger desorption energies and adjacent adsorption sites. With more adsorbed species available on the surface, in closer proximity, and with higher migration lengths, the reaction probability to form GaP is enhanced. This is seen in the data of GaP/SiO₂ deposits in Sec. 4.4.1, which

show that continuous films of GaP can be deposited although of a polycrystalline nature.

GaP / nrSi

We concluded previously that increasing the substrate surface energy γ_{sv} would reduce the nucleation energy barrier ΔG^c , and the use of nrSi substrates was suggested. Compared to singular or vicinal (001) Si, nrSi generated by chemical etching or other means will expose various high-index planes, resulting in an increased surface area and higher densities of irregularly oriented dangling bonds. The surface energy is therefore expected to be larger. Thus from a thermodynamics point of view, the nucleation energy barrier must be smaller for heteroepitaxy on nrSi.

From the kinetics point of view, nrSi may also contain a high density of kink sites. As discussed in Sec. 2.1.3.3, adatoms that impinge and adsorb on the kink sites can be incorporated directly without the necessity for nucleation, which also generates new kink sites. Thus ideally, starting from a certain kink site and depending on its nature, either both Ga and P are incorporated alternatively from the respective precursors, or only one species gets incorporated continuously. Growth on surfaces with high kink densities should exhibit only short range correlations and hence appear continuous. Thus heteroepitaxy on nrSi should follow the mode of continuous growth, in which the morphology of the rough kink surface is retained and with a growth rate given by Eq. (2.1.3.31). As with the 2D nucleation-mediated layer-by-layer growth of GaP on GaAs, continuous growth here can also be described by the arrival-rate calculations of Sec. 4.5.1. However, a factor of $(a/\delta)^2$ needs to be included to describe the geometric probability of finding a kink site. Here a and δ are the distances between ordinary and kink sites, respectively. For the case of GaP on nrSi (1:1:1), as in Sec. 4.3.1, the growth rate of 0.21 nm/s is fairly close to that predicted by the kinetics calculations. Therefore, we conclude that $(a/\delta)^2 \approx 1$ for a nrSi (1:1:1) surface

and that the kink site density is fairly large.

A distinct feature for the mode of continuous growth on a rough kink-covered surface is that the film roughness is conformal, following the substrate and barely changing with time. This is evident by following the evolution of E_2 peak of $\langle \epsilon_i \rangle$ in real time. If the starting E_2 peak is low, it may increase slightly but will soon saturate as the film gets thicker, regardless of how growth conditions are changed. A good example is given in Fig. 4.3.5 for GaP on nrSi (1:1:1). This is consistent with the post-growth AFM micrographs of Fig. 4.3.4, which show features similar to the original nrSi. Moreover, if the growth rate is small compared to the vertical roughness features, a recognizably sharp growth front will be hard to define. As a result the real-time RI and $\langle \epsilon \rangle$ data for continuous growth cannot be analyzed using a layer-by-layer model, since the data are averaged over the large area of the beam spot.

Despite the fact that the continuous growth mode is realized on nrSi (1:1:1), heteroepitaxy on other chemically etched substrates such as nrSi (1:3:5) and nrSi (1% NH_4F) still proceed in the 3D growth mode. The reason can be found by a careful examination of the etching mechanisms of various solutions and the post-etching AFM micrographs for the Si. Etching by mixtures of HF, HNO_3 , and H_2O usually has a high rate, and is diffusion-limited and isotropic. The RMS roughness of nrSi (1:1:1) (30 s) is about 7 nm, and this surface is terminated with randomly distributed fine structure consisting of mainly concave etch pits with dimensions smaller than 50 nm. The resolution of smaller features is limited by the radius of the AFM probe, which is 20 nm here. The above surface contains a high density of kink sites, and the structure favors GaP nucleation and continuous growth as shown in Sec. 4.3.1. As a contrary, the RMS roughness of nrSi (1:3:5) (1 min) is only ~ 1.5 nm, thus the kink-site density is likely to be much smaller than that of nrSi (1:1:1). Hence the nucleation density is also smaller.

Etching by weak solutions of NH_4F or NH_4OH at elevated temperatures usually occurs at a low rate, and is reaction-rate limited and anisotropic. We consider the situation for nrSi

(1% NH_4F) (7 min). Although its RMS roughness of ~ 12 nm is larger than that of nrSi (1:1:1), the composing grains have 40 to 100 nm diameters and convex morphologies. Thus nrSi (1% NH_4F) exposes mainly well-defined convex grains exposing $\{111\}$, $\{211\}$, or similar low energy facets, which makes nucleation even more difficult. Besides, since the anisotropic etching rates are higher for kinks and steps, the densities of such sites are expected to be very low, which makes the rough Si not suitable for our purpose of increasing the initial nucleation density. This is evident from the AFM micrographs of the surface after growth in Figs. 4.3.8 and 4.3.10, which show that the GaP islands exhibit even larger sizes and spacings than those seen with growth on flat Si under similar conditions.

Thus it appears that etching in 1:1:1 HF:HNO₃:H₂O for 30 s is the most efficient way so far of generating nrSi with large densities of kink sites. However, the quality of heteroepitaxial GaP grown on nrSi (1:1:1) is still not satisfactory, and more surface engineering techniques need to be explored.

GaP / SiO₂

From the earlier discussion, the use of SiO₂ as a substrate has two advantages. From the thermodynamics point of view, the bonding by O reduces both the film-substrate interfacial energy γ_{fs} and the nucleation-barrier energy ΔG^c . From the kinetics point of view, the electronegativity difference (in Pauling scale) between O (3.44) and Si (1.9) is 1.54, and that between As (2.18) and Ga (1.81) is 0.37. Thus SiO₂ can also be view as a polar material. The dipole interaction between PH₃ and SiO₂ can therefore catalyze the heterogeneous decomposition of PH₃ above the SiO₂ surface. The generation of more reactant species favors chemisorption, which further increases the surface density of adsorbed reactants. However, SiO₂ is amorphous, so the Si-O bonds are randomly oriented. This may reduce the catalytic effect compared to (001) GaAs or other III-V surfaces. In fact, the measured PH₃ decomposition activation energy on SiO₂ is between that on Si and InP

substrates. Nevertheless, due to the two reasons above, nucleation and growth of GaP on SiO₂ is easier than that on flat Si, as clearly shown by the data of Sec. 4.4.1.

The amorphous nature of SiO₂ means that it cannot provide a reference frame where Ga and P can be incorporated selectively into two separate sublattices. Thus GaP on SiO₂ is polycrystalline, as confirmed by the AFM micrographs after growth. The real-time SE and SR data for GaP films on SiO₂ can also be analyzed using a layer-by-layer model, and by so doing the resulting GaP concentration is found to be very low, of the order of 40 to 70%. Thus the growth of GaP on SiO₂ proceeds by the pseudo 2D-nucleation-mediated path.

Chapter 5 Summary and Conclusions

The objectives of this work are (1) to study OMCVD growth mechanisms, focusing on the lattice-matched but chemically mismatched heteroepitaxy of GaP on Si, and (2) to explore the possibility of improving the quality of the deposited GaP. We work within contemporary OMCVD technology, and examine particularly the possibility of improving the quality of the deposited GaP by using Si substrates that were deliberately roughened on the scale of nm prior to growth. With much higher densities of nucleation sites and lower mobilities of surface species, rough surfaces in principle eliminate the major problems associated with as-polished wafers that lead to widely spaced islands. To obtain additional information about the growth process, we made comparative measurements on the chemically compatible but lattice-mismatched system of GaP on GaAs, and the polar-on-polar system of GaP on thermally generated amorphous SiO₂. Inadvertent but nonetheless important data in establishing growth details were also obtained from a fifth surface, that of the Mo susceptor surrounding the sample. We use SP to follow growth chemistry in real time, and then analyze the deposited material with various techniques including AFM and SE.

Gas phase kinetics

To understand the growth process quantitatively, we investigated in detail the gas-phase kinetics inside our vertical-flow, low-pressure OMCVD reactor chamber. We calculated various kinetics parameters based on simple hard-sphere approximations, such as mean-free paths, diffusion coefficients, surface-arrival and reaction rates, etc. We also calculated the various characteristic dimensionless parameters. The Knudsen number is of the order of 10^{-4} to 10^{-3} , so gas flow can be viewed as continuous. The Reynolds number is smaller than

25, so the flow conditions are well within the regime of laminar flow without rippling or turbulence. The Péclet number is larger than 1 but smaller than 10, so mass transport is primarily by advection. However, diffusion also plays an important role as graphically demonstrated by the functional form of the variations in lateral thickness. The Damköhler number is much larger than 1, so the homoepitaxial growth of GaP is mass-transport limited. We also estimate the growth rate and compare it to experiment. These calculations show that a stagnant layer exists over the sample, and that its thickness is of the order of 0.5 to 1 cm.

From the results of these analyses, we now have a significantly better understanding of the processes as taking place inside the reactor chamber, and can now design growth conditions to optimize any specific task that we would like to achieve.

Lateral thickness variations

We have found that GaP films grown in our vertical-flow, low-pressure OMCVD reactor usually have nonuniform thicknesses. The deposited material may be thinner or thicker at the edges of our 2" substrate wafer than at the center, but in all cases shows an exponential dependence on radius. While nonuniformly thick epitaxial layers are a common problem in epitaxy, these are usually attributed to depletion of gas-phase reactants, which in vertical-flow reactors occurs from the center outward. Our thickness variations do not fall in this category, and as a result provide new information about OMCVD growth processes.

In analyzing these thickness variations we found that the causes all trace back to the differences in chemical properties of the various surfaces investigated here, more specifically, to the different catalytic effects that these surfaces exert on PH_3 decomposition and their tendencies to achieve good-quality GaP heteroepitaxy. A surface of particular interest here is that associated with the polycrystalline GaP deposited on the Mo susceptor that surrounds the actual substrate, which serves as a reference. These data in fact provide unambiguous

evidence that deposition occurs via a precursor that involves both Ga and P, and is formed by heterogeneous catalysis. In addition, this precursor is likely to be largely desorbed and to decompose in the gas phase. Starting with the diffusion equation, we derive analytic expressions that describe the variations in terms of the diffusion parameters and evaluate the diffusion length quantitatively. These results coincide with our observations, and show that different parts of the surface – including that of the susceptor – are in constant contact with each other during growth through gas-phase diffusion. We can use these results to make predictions concerning the formation of various lateral thickness profiles under different flow and substrate conditions, although some may not occur in real situations. These results strongly support the growth model that we propose. Details are provided in Sec. 4.5.2 and briefly summarized here.

We consider first the growth of GaP on nrSi (1:1:1), where the thickness at the edge is greater than the center. Since the decomposition of PH_3 is least efficient on nrSi, it is not surprising that cracking rate of PH_3 and therefore the production rate of the relevant growth precursor is greater on the Mo susceptor edge. PH_3 decomposition here is also aided by the fact that the susceptor temperature is about 100 °C higher than that of the wafer, and is also catalyzed by the enhanced dipole interactions exerted by the Mo surface itself or the polycrystalline GaP layer that coats it. The decomposition products, which we assume the H-P=Ga-CH₃ adducts, back-diffuse against the advection flow and result in additional growth on the outer edge of the nrSi (1:1:1) wafer. The model is consistent with the fact that the Péclet number of our system is not very large (< 10). Thus diffusion certainly coexists with advection, so downstream reactants are able to diffuse upstream into the system. The diffusion characteristic length is estimated to be 0.9 cm from a 2D random walk model, which is comparable to the observed λ of 0.5 cm.

Similar situations have been observed for GaP grown on Si and nrSi (1% NH_4F), where the decomposition of PH_3 are also inefficient. The effects of reactant back-diffusion are

more spectacular here, since 3D islands are grown in the center but the increased supply of precursors from the Mo susceptor results in a continuous GaP film deposited near the edge.

GaP grown on GaAs is different from the above in that the edge is thinner than the center. Here, PH_3 decomposition is more efficient on the epitaxial GaP deposited on GaAs than on the polycrystalline GaP deposited on the susceptor. Diffusion now reduces the concentration of the active species in the gas phase near the edge, and the result is an exponentially reduced thickness as the edge is approached.

GaP grown on SiO_2 also has a reduced thickness at the edge. However, both the exponential factor and the characteristic length are smaller than those associated with GaAs. This is consistent with the fact that the heterogeneous catalysis effect of SiO_2 and the resulting low-quality GaP on PH_3 decomposition is between that of GaAs or high-quality GaP on the one hand, and Si or nrSi on the other. However, it is very similar to that of the polycrystalline GaP coating the Mo susceptor. Therefore, diffusion again reduces the supply of the active species at the edge, consistent with observations.

Growth mechanisms

We have proposed a model for the growth of GaP in OMCVD using the precursors TMG and PH_3 . This model is based on information from the literature and our own observations, particularly those that demonstrate that different regions of the growth surface are in communication through the gas phase. Our model considers primarily the formation of reactants that are directly responsible for GaP growth, which we assume to exhibit the chemical form of $\text{H-P}=\text{Ga-CH}_3$ adducts, among many other possibilities. These adducts can form through extensive collisions between the reactive species of Ga and P, either homogeneously in the gas phase, or heterogeneously on the growth surface by reaction between adsorbates. The latter process appears to be predominant. The concentration of adducts formed depends on the collision probabilities between the precursors, which are

proportional to the number densities and relative velocities for the homogeneous case, and the surface densities and relative surface mobilities for the heterogeneous case.

The mechanism for the generation of $\text{H-P}=\text{Ga-CH}_3$ adducts is considered to be as follows. As a result of heterogeneous catalysis aided by high temperature, a TMG molecule impinging on the growth surface readily decomposes into one MMG molecule and two methyl radicals or one ethane molecule. The MMG molecule, in the form of $=\text{Ga-CH}_3$, has two unpaired bonds that are not stable. A MMG molecule that desorbs back into the gas phase can react with a PH_3 molecule, or its decomposition product of a H-P molecule. The former has two available bonds in the form of lone-pair electrons, and the latter has two open orbitals and behaves like S. If the reaction occurs the result is expected to be a $\text{H-P}=\text{Ga-CH}_3$ adduct with or without a H_2 molecule. The heterogeneous generation of adducts is probably more complicated, since it would involve multistage reactions and bond breakings on the surface. The exact scenario is not clear at this stage. Nevertheless, it is well known that GaP by itself deteriorates rapidly at temperatures of the order of 600°C , generating volatile P_2 and P_4 and leaving behind metallic Ga. To prevent this decomposition, a minimum PH_3 partial pressure needs to be maintained over the GaP surface. As a result, exchange currents involving various P species are expected to be fairly large. Thus there should be no shortage of reactive P species near the GaP surface. When TMG is introduced, the MMG decomposition product is expected to react with these species. This again favors the generation of $\text{H-P}=\text{Ga-CH}_3$. The above picture is only hypothetical, and needs further justifications from chemistry. Nevertheless it agrees well with our data.

We find that substrates also play a very important role in our model in three ways. First, substrates catalyze the heterogeneous decomposition of PH_3 , which is very inefficient in the gas phase at our growth temperatures. Thus substrates essentially control the generation of P-reactive species. Second, substrates determine the adsorption behavior of the precursors via adsorption energies and migration lengths, and thus control the

heterogeneous formation of the adducts. Finally and most important, substrates provide reference frames and nucleation sites for the heteroepitaxial growth of GaP.

Thus the two rate-determining steps for the growth of GaP in our model are (1) the generation of P-reactive species due to substrate catalyzation of PH_3 decomposition by the substrate; and (2) the subsequent formation and incorporation of $\text{H-P}=\text{Ga-CH}_3$ adducts, which can occur both homogeneously and heterogeneously. Our model, when used together with the thermodynamics and kinetic theories of nucleation and epitaxy, provides a consistent explanation of the various growth behaviors that we have observed. These are discussed in detail in Sec. 4.5.3 and the results are briefly summarized below.

In step (1), the generation and number density of the P-reactive species available depends largely on the catalytic effect of the substrate on PH_3 decomposition. For the substrates used in this work, PH_3 decomposition is seen to occur most efficiently on (001) GaAs and high-quality heteroepitaxial GaP grown on (001) GaAs. Decomposition is less efficient on SiO_2 and low-quality heteroepitaxial GaP grown on SiO_2 and the Mo susceptor, and relatively inefficient on Si and nrSi. This is in accordance with the measurements of various activation energies for PH_3 decomposition on different substrates by other groups.

From a thermodynamics point of view, the interfacial energies are in the order $\gamma_{\text{GaP}/\text{GaAs}} < \gamma_{\text{GaP}/\text{SiO}_2} < \gamma_{\text{GaP}/\text{Si}}$, and the substrate energies $\gamma_{\text{nrSi}} > \gamma_{\text{Si}}$. Thus the critical nucleus size and the nucleation energy barrier are expected to be highest for GaP heteroepitaxy on Si, which in fact follows the 3D-nucleation-mediated-growth mode and results in widely spaced 3D GaP islands. In contrast, the heteroepitaxy of GaP on (001) GaAs, nrSi (1:1:1), and thermally generated SiO_2 proceed as the growth modes of 2D-nucleation-mediated layer-by-layer, continuous, and pseudo 2D-nucleation-mediated layer-by-layer, respectively. The resulting GaP films are single-crystal, rough single-crystal, and polycrystal, respectively. The above can be further understood by analyzing the kinetic processes of step (2).

For GaAs, in addition to the facile generation of P-reactive species, the precursors are

also chemisorbed in large quantities and exhibit high surface mobilities. Thus reaction probabilities are very high. Also, the polar nature of GaAs allows two precursors to be chemisorbed selectively in adjacent Ga and As (or P) sites that are available, where they can readily react with each other to form GaP and hence bypass in part the adduct stage. Since the chemisorbed precursors are highly supersaturated with respect to the critical 2D nuclei, they can easily attach to edges, thereby contributing to lateral overgrowth and form single crystal GaP, as observed. Growth on SiO₂ is very similar, since SiO₂ can also be viewed as a polar material. However, the amorphous nature of SiO₂ cannot provide a reference frame where Ga and P can be incorporated selectively into two separate sublattices. Thus GaP grown on SiO₂ is polycrystalline.

By contrast, growth on Si is limited by the density of gas-phase P precursors, which is small. Also, the nonpolar nature of Si cannot provide selective chemisorption as can GaAs and SiO₂. Therefore, the reactants are physisorbed with low densities. Thus the reaction probability between precursors is very low, and nucleation is generally not possible, except perhaps at occasional defect sites.

Growth of GaP on nrSi is different. A nrSi (1:1:1) surface contains a high density of kink sites, which favors the direct incorporation of adatoms that impinge and adsorb on them. At the same time new kink sites are generated. Thus ideally starting from a specific kink site and depending on its nature, either both Ga and P are incorporated alternatively from the respective precursors, or only one species gets incorporated continuously. Growth on surfaces with high kink densities has only short-range correlations, is found to be conformal to the film roughness, and appears to be continuous. On the other hand, growth of GaP on Si substrates chemically etched as nrSi (1:3:5) and nrSi (1% NH₄F) proceeds in the 3D growth mode, since these nrSi surfaces either have smaller kink-site densities or exhibit mainly low-energy facets that do not favor GaP nucleation.

Future work

Our next goal is to continue to improve the quality of heteroepitaxial GaP on Si with the hope of achieving monolithic integration of these two materials. Based on the results of this work, we suggest two promising approaches. The first involves changing growth conditions, and the second engineering a nrSi substrate.

As described in Ch. 4, the reasons for the poor nucleation behavior of GaP on Si are partially ascribed to the inefficient decomposition of PH_3 , and the subsequent low reaction probability between Ga and P precursors for the formation of H-P=Ga-CH_3 adducts. We attempted to solve the second problem by increasing the flow rate of either TMG or PH_3 in order to increase the collision and reaction probabilities. By so doing we also expected to overcome the first problem, since the decomposition of PH_3 is enhanced due to the increased collisions with other molecules including Ga species.

Increasing the TMG flow rate through TMG bursts was found to increase both nucleation and growth rates, since the nucleation energy barrier and critical nucleus size for Ga species are both reduced. However, the enhanced nucleation also resulted in rough surface morphologies and structure defects, which counteract its merits. Thus we conclude that Ga-rich conditions should be avoided. On the other hand, increasing the PH_3 flow rate partially compensates for the inefficiency of PH_3 decomposition and also enhances the nucleation density. However, this is still not effective alone in producing good quality GaP films, and results in too much waste of the PH_3 precursor.

The collision probability is actually proportionally to the individual partial pressures, which are also limited by the growth pressure in addition to the flow rates. In our experimental configuration the chamber pressure is established by a throttle valve placed before the pump. As a result of hardware issues, all the experiments in this work were done under a chamber pressure of 4 Torr. That is considerably less than the typical OMCVD growth pressure used by others, as seen in Table 1.1. In fact, even the use of pressures as

high as atmospheric is not unusual. As seen earlier in Sec. 4.2.2, the best results that have been achieved in our OMCVD system prior to the present investigation were obtained with a chamber pressure of 60 Torr. In that case, the individual partial pressures of the active P and Ga species were 10 times higher and the collision probability 100 times higher than used in the present work. Since then the hardware problems have been solved, so we will investigate growth at elevated system pressures. This is consistent with the study of other groups, e.g., Soga et al. in Ref. [19].

By far the most effective way of generating nrSi with a high density of kink sites is by etching in HF, HNO₃, and H₂O solutions (1:1:1) on the time scale of 30 s. The use of nrSi (1:1:1) substrates improves the GaP nucleation and promotes the growth of continuous films. However, these results are still far from satisfactory from the perspective of achieving high-quality materials. The nrSi (1:1:1) substrate exhibits too much macroscopic height variation or vertical macroscopic roughness, thus making the growth of smooth layer virtually impossible. Also the etching rate is too high to allow for precise control. Thus other chemical etchants should be studied, including other combinations of HF, HNO₃, and H₂O. The development of modern photolithography techniques on the nm scale (nanolithography) might also provide a solution for generating appropriate nrSi.

The valuable experience that we have gained on the quantitative analysis of the OMCVD process, in particular the modeling of the growth mechanisms and information gained from the lateral thickness variation, is also directly applicable to the study of other material systems as well. For example, we are currently investigating the problem of heteroepitaxy of ZnO on Al₂O₃ and Si by OMCVD, where the precursor reactions are predominately homogeneous and require special control.

References

1. J. P. Andre, J. Hallais, and C. Schiller, *J. Cryst. Growth* 31, 147 (1975).
2. H. B. Pogge, B. M. Kendlage, and R. W. Broadie, *J. Cryst. Growth* 37, 13 (1977).
3. H. Beneking and H. Roehle, *J. Cryst. Growth* 55, 79 (1981).
4. Y. Su, *J. Phys. D* 15, 2325 (1982).
5. L. Samuelson, P. Omling and H. G. Grimmeiss, *J. Cryst. Growth* 68, 340 (1984).
6. J. M. Olson, M. M. Al-Jassim, A. Kibbler, and K. M. Jones, *J. Cryst. Growth* 77, 515 (1986).
7. M. Sugo, A. Yamamoto, and M. Yamaguchi, *J. Cryst. Growth* 88, 229 (1988).
8. K.A. Bell, M. Ebert, S.D. Yoo, K. Flock and D.E. Aspnes, *J. Vac. Sci. Technol. A* 18, 1184 (2000).
9. V. K. Dixit, T. Ganguli, T.K. Sharma, R. Kumar, S. Porwal, V. Shukla, A. Ingale, P. Tiwari and A.K. Nath, *J. Cryst. Growth* 293, 5 (2006).
10. Y. Kohama, K. Uchida, T. Soga, T. Jimbo, and M. Umeno, *Appl. Phys. Lett.* 53, 862 (1988).
11. Y. Kohama, Y. Kadota, and Y. Ohmachi, *Jpn. J. Appl. Phys.* 29, L229 (1990).
12. T. Soga, T. Jimbo, and M. Umeno, *Appl. Surf. Sci.* 82/83, 64 (1994).
13. M. Imaizumi, T. Saka, T. Jimbo, T. Soga, and M. Umeno, *Jpn. J. Appl. Phys.* 30, 451 (1991).
14. T. Soga, T. George, T. Suzuki, T. Jimbo, M. Umeno, and E.R. Weber, *Appl. Phys. Lett.* 58, 2108 (1991).
15. T. Soga, T. George, T. Jimbo, M. Umeno, *Jpn. J. Appl. Phys.* 30, 3471 (1991).
16. T. Soga, T. George, T. Jimbo, M. Umeno, *J. Cryst. Growth* 115, 418 (1991).
17. T. Suzuki, T. Soga, T. Jimbo, and M. Umeno, *J. Cryst. Growth* 115, 158 (1991).
18. T. Soga, T. Suzuki, M. Mori, T. Jimbo, and M. Umeno, *J. Cryst. Growth* 132, 134 (1993).

19. T. Soga, T. Jimbo, and M. Umeno, *J. Cryst. Growth* 163, 165 (1996).
20. J.R. Gong, S. Nakamura, M. Leonard, S.M. Bedair and N.A. El-Masry, *J. Electron. Mater.* 21, 965 (1992).
21. S.W. Choi, G. Lucovsky and K.J. Bachmann, *J. Vac. Sci. Technol. B* 10, 1070 (1992).
22. S.W. Choi, K.J. Bachmann and G. Lucovsky, *J. Vac. Sci. Technol. A* 11, 626 (1993).
23. S. Gonda, Y. Matsushima, S. Mukai, Y. Makita and O. Igarashi, *Jpn. J. Appl. Phys.* 17, 1043 (1978).
24. H. Kawanami, T. Sakamoto, T. Takahashi, E. Suzuki and K. Nagai, *Jpn. J. Appl. Phys.* 21, L68 (1982).
25. S.L. Wright, M. Inada and H. Kroemer, *J. Vac. Sci. Technol.* 21, 534 (1982).
26. S.L. Wright, H. Kroemer and M. Inada, *J. Appl. Phys.* 55, 2916 (1984).
27. W.G. Bi, X.B. Mei and C.W. Tu, *J. Cryst. Growth* 164, 256 (1996).
28. T. Tsuji, H. Yonezu, M. Yokozeke, Y. Takagi, Y. Fujimoto and N. Ohshima, *Jpn. J. Appl. Phys.* 36, 5431 (1997).
29. U. Takagi, H. Yonezu, K. Samonji, T. Tsuji and N. Ohshima, *J. Cryst. Growth* 187, 42 (1998).
30. M. Sadeghi and S. Wang, *J. Cryst. Growth* 227-228, 279 (2001).
31. X. Yu, P.S. Kuo, K. Ma, O. Levi, M.M. Fejer and J S Harris, *J. Vac. Sci. Technol. B* 22, 1450 (2004).
32. J.T. Kelliher, J. Thornton, N. Dietz, G. Lucovsky and K.J. Bachmann, *Mater. Sci. Eng. B* 22, 97 (1993).
33. K.J. Bachmann, N. Dietz, A.E. Miller, D. Venables, and J.T. Kelliher, *J. Vac. Sci. Technol. A* 13, 696 (1995).
34. K.J. Bachmann, U. Rossow, N. Sukidi, H. Castleberry, and N. Dietz, *J. Vac. Sci. Technol. B* 14, 3019 (1996).
35. C.A. Larsen, N.I. Buchan and G.B. Stringfellow, *J. Cryst. Growth* 85, 148 (1987).

36. N.I. Buchan, C.A. Larsen and G.B. Stringfellow, *Appl. Phys. Lett.* 51, 1024 (1987).
37. N.I. Buchan, C.A. Larsen and G.B. Stringfellow, *J. Cryst. Growth* 92, 605 (1988).
38. C.A. Larsen, N.I. Buchan and G.B. Stringfellow, *Appl. Phys. Lett.* 52, 480 (1988).
39. C.A. Larsen, S.H. Li, N.I. Buchan, G.B. Stringfellow and D.W. Brown, *J. Cryst. Growth* 102, 126 (1990).
40. G.G. Devyatikh, V.M. Kedyarkin and A.D. Zorin, *Russ. J. Inorg. Chem.* 14, 1055 (1969).
41. M. Yoshida, H. Watanabe and F. Uesugi, *J. Electrochem. Soc.* 132, 677 (1985).
42. M.G. Jacko and S.J.W. Price, *Can. J. Chem.* 41, 1560 (1963).
43. D.W. Squire, C.S. Dulcey and M.C. Lin, *Mater. Res. Soc. Symp. Proc.* 101, 301 (1988).
44. J.A. McCaulley, V.R. McCrary and V.M. Donnelly, *J. Phys. Chem* 93, 1148 (1989).
45. D.J. Schlyer and M.A. Ring, *J. Electrochem. Soc.* 124, 569 (1977).
46. M.R. Leys and H. Veenvliet, *J. Cryst. Growth* 55, 145 (1981).
47. J. Nishizawa and T. Kurabayashi, *J. Electrochem. Soc.* 130, 413 (1983).
48. D.H. Reep and S.K. Ghandhi, *J. Electrochem. Soc.* 130, 675 (1983).
49. J.E. Butler, N. Bottka, R.S. Sillmon and D.K. Gaskill, *J. Cryst. Growth* 77, 188 (1986).
50. T. George, E.R. Weber, S. Nozaki, A.T. Wu, N. Noto and M. Umeno, *J. Appl. Phys.* 67, 2441 (1990).
51. C. H. Choi, R. Ai, and S. A. Barnett, *Phys. Rev. Lett.* 67, 2826 (1991).
52. T.Y. Gorbach, R.Y. Holiney, L.A. Matveeva, P.S. Smertenko, S.V. Svechnikov, E.F. Venger, R. Ciach and M. Faryna, *Thin Solid Films* 336, 63 (1998).
53. T.Y. Gorbach, R.Y. Holiney, L.A. Matveeva, S.V. Svechnikov, E.F. Venger, M. Kuzma and G. Wisz, *Mater. Sci. Eng. B* 71, 288 (2000).
54. A. Bakin, D. Piester, I. Behrens, H. Wehmann, E. Peiner, A. Ivanov, D. Fehly and A. Schlachetzki, *Cryst. Growth Des.* 3, 89 (2003).
55. A. Hashimoto, T. Fukunaga and N. Watanabe, *Appl. Phys. Lett.* 54, 998 (1989).
56. K.R. Sprung, K. Wilke, G. Heymann, J. Varrio and M. Pessa, *Appl. Phys. Lett.* 62, 2711

- (1993).
57. A. Krost, R.F. Schnabel, F. Heinrichsdorff, U. Rossow, D. Bimberg and H. Cerva, J. Cryst. Growth 145, 314 (1994).
 58. R. Bhat, J. Cryst. Growth 120, 362 (1992).
 59. J.Z. Li, J. Bai, J.S. Park, B. Adekore, K. Fox, M. Carroll, A. Lochtefeld and Z. Shellenbarger, Appl. Phys. Lett. 91, 021114 (2007).
 60. S.F. Cheng, L. Gao, R.L. Woo, A. Pangan, G. Malouf, M.S. Goorsky, K.L. Wang and R.F. Hicks, J. Cryst. Growth 310, 562 (2008).
 61. H. Liu and D.S. Dandy, Diamond Relat. Mater. 4, 1173 (1995).
 62. P.A. Dennig and D.A. Stevenson, Appl. Phys. Lett. 59, 1562 (1991).
 63. R.R. Saxena, C.B. Cooper III, M.J. Ludowise, S. Hikido, V.M. Sardi and P.G. Borden, J. Cryst. Growth 55, 58 (1981).
 64. M. Sato and M. Suzuki, J. Electrochem. Soc. 134, 1540 (1987).
 65. G. Costrini and J.J. Coleman, J. Appl. Phys. 57, 2249 (1985).
 66. L.M. Miller and J.J. Coleman, CRC Crit. Rev. Solid State Mater. Sci. 15, 1 (1988).
 67. G. B. Stringfellow, Organometallic Vapor-Phase Epitaxy, 2nd Edition, Academic Press, 1999.
 68. M. Ohring, Material Science of Thin Films, 2nd Edition, Academic Press, 2002.
 69. D.L. Smith, Thin-film deposition: principles and practice, McGraw-Hill, 1995.
 70. W.R. Salzman, <http://www.chem.arizona.edu/~salzmanr/480a/480ants/kmtnts.html>.
 71. G. S. Bales, A. C. Redfield, and A. Zangwill, Phys. Rev. Lett. 62, 776 (1989).
 72. D.M. Dobkin and M.K. Zuraw, Principles of Chemical Vapor Deposition, Kluwer Academic Publishers, the Netherlands, 2003;
http://www.timedomaincvd.com/CVD_Fundamentals/Fundamentals_of_CVD.html;
http://www.enigmatic-consulting.com/semiconductor_processing/CVD_Fundamentals/Fundamentals_of_CVD.html.

73. R.B. Bird, W. E. Stewart and E.N. Lightfoot, *Transport Phenomena*, John Wiley & Sons, 1960.
74. <http://w3eos.whoi.edu/12.747/notes/lect15/l15s04.html>
75. R. J. Hamers, http://hamers.chem.wisc.edu/chem630_fall2006/nucleation_and_growth/nucleation_and_growth2.ppt
76. K. Reichelt, *Vacuum* 38, 1083 (1988).
77. D. Kashchiev, J.P. Van Der Eerden and C. Van Leeuwen, *J. Cryst. Growth* 40, 47 (1977).
78. S. Cooper, <http://www.dur.ac.uk/sharon.cooper/lectures/cryskinetics/handoutsall.html>
79. S.S. Iyer, T.A. Metzger and F.G. Allen, *J. Appl. Phys.* 52, 5608 (1981).
80. I.V. Markov, *Crystal Growth for Beginners*, 2nd Edition, World Scientific Publishing, 2003.
81. I.V. Markov, *Phys. Rev. B* 53, 4148 (1996).
82. D. E. Aspnes, *Thin Solid Films* 89, 249 (1982).
83. P. Lautenschlager, M. Garriga, L. Vina and M. Cardona, *Phys. Rev. B* 36, 4821 (1987).
84. D. E. Aspnes, *Surf. Sci.* 135, 284 (1983); D. E. Aspnes, *Sol. Energy Mater. Sol. Cells* 32, 413 (1994); S. D. Yoo and D. E. Aspnes, *J. Appl. Phys.* 89, 8183 (2001).
85. K. A. Bell, Ph.D. Thesis, North Carolina State University, Raleigh, 2000.
86. S. Kim, Ph.D. Thesis, North Carolina State University, Raleigh, 2004.
87. S. D. Hersee and J. M. Ballingall, *J. Vac. Sci. Technol. A* 8, 800 (1990).
88. K. Flock, Ph.D. Thesis, North Carolina State University, Raleigh, 2003.
89. M. Asar, Ph.D. Thesis, North Carolina State University, Raleigh, 2005.
90. D. R. Lide (Editor in Chief), *Handbook of Chemistry and Physics*, 82nd Edition, CRC Press, Boca Raton/New York, 2001 – 2002.
91. A. M. Gallois, T. M. Besmann, and M. W. Stott, *J. Am. Ceram. Soc.* 77, 2949 (1994).
92. H. Habuka, H. Tsunoda, M. Mayusumi, N. Tate, and M. Katayama, *J. Electrochem. Soc.* 142, 3092 (1995).

93. Y. Yanase, H. Horie, Y. Oka, M. Sano, S. Sumita, and T. Shigematsu, *J. Electrochem. Soc.* 141, 3259 (1994).
94. M. Futagami and M. Hamazaki, *Jpn. J. Appl. Phys.* 21, 1782 (1982).
95. F.W. Smith and G. Ghidini, *J. Electrochem. Soc.* 129, 1300 (1982).
96. J.J. Lander and J. Morrison, *J. Appl. Phys.* 33, 2089 (1962).
97. S. Shih, K.H. Jung, T.Y. Hsleh, J. Sarathy, J.C. Campbell and D.L. Kwong, *Appl. Phys. Lett.* 60, 1863 (1992).
98. A. Schwartz and H. Robbins, *J. Electrochem. Soc.* 123, 1903 (1976).
99. V.A. Kiselev, S.V. Polisadin and A.V. Postnikov, *Semiconductors* 31, 704 (1997).
100. W. Kern, *RCA Rev.* 39, 278 (1978).
101. G.S. Higashi, Y.J. Chabal, G.W. Trucks and K. Raghavachari, *Appl. Phys. Lett.* 56, 656 (1990).
102. M.A. Hines, *Int. Rev. Phys. Chem.* 20, 645 (2001).
103. S.P. Garcia, H. Bao, M.A. Hines, *Surf. Sci.* 541, 252 (2003).
104. E.D. Palik, V.M. Bermudez and O.J. Glembocki, *J. Electrochem. Soc.* 132, 871 (1985).
105. T. Hannappel, W.E. McMahon and J.M. Olson, *J. Cryst. Growth* 272, 24 (2004).
106. W.G. Breiland, M.E. Coltrin, J.R. Creighton, H.Q. Hou, H.K. Moffat and J.Y. Tsao, *Mater. Sci. Eng.* R24, 241 (1999).
107. C.D. Thurmond, *J. Phys. Chem. Solids* 26, 785 (1965).